Water Decontamination Using Magnetic Biochar Produced from Biomass and Mineral Processing Waste

by

Soumik Chakma

A thesis submitted to
The Faculty of Graduate Studies

of

Lakehead University

In partial fulfillment of the requirements

For the Degree of
Master of Science in Environmental Engineering

April 2025

Supervisor**:** Dr. Kang Kang

Co-supervisor: Dr. Sudip K. Rakshit

Dedication

I dedicate this thesis to my parents, Suprity Chakma and Swati Talukder

Abstract

Contamination from industrial wastewater is a serious environmental problem, often requiring innovative treatment methods beyond traditional technologies. This thesis explores the development of magnetic biochar (MBC), a carbon-rich, magnetically separable material produced by pyrolyzing biomass with iron sources as an efficient and sustainable solution for water decontamination. The research first reviews recent advances in biochar design, modification, and application for heavy metal removal, highlighting key factors like feedstock choice, pyrolysis conditions, and activation methods. In the experimental work, MBC was synthesized using different iron compounds and production methods. Among them, one-step co-pyrolysis of maple wood and FeO at 700 °C produced the most effective MBC for removing a model dye, Remazol Brilliant Blue R (RBBR), achieving nearly 100% removal under acidic conditions. Adsorption studies revealed that the process followed pseudo-second-order kinetics and fit the *Langmuir* isotherm model. Taking this a step further, a new approach was developed by co-pyrolyzing red mud, an industrial waste, rich in iron, with chemically activated biomass (treated with KOH and HNO_3) to produce cost-effective MBC. The KOH-activated MBC demonstrated outstanding performance, achieving almost 100% removal of copper (Cu^{2+}) and lead (Pb^{2+}) ions from water, while also offering lower production costs compared to HNO_3-activated MBC. Overall, this work demonstrates that properly engineered MBC materials, including those made from waste resources like red mud, offer a highly promising, low-cost, and eco-friendly solution for treating dye- and heavy metal-contaminated waters.

Acknowledgement

First and foremost, I would like to express my deepest gratitude to my esteemed supervisors, Dr. Kang Kang and Dr. Sudip K. Rakshit. Their unwavering support, insightful guidance, and valuable feedback have been instrumental throughout every stage of my research journey. I am truly grateful for the opportunity to work under their mentorship and for the encouragement and dedication they have consistently shown.

I am also sincerely thankful to my thesis committee members, Dr. Baoqiang Liao and Dr. Francisco Ramos-Pallares, for their constructive feedback, encouragement, and thoughtful suggestions, which have helped strengthen my work and broaden my perspective. I would like to thank Dr. Leila Pakzad for her guidance and support in her role as graduate coordinator throughout my studies.

My sincere appreciation goes to Dr. Gousheng Wu, Mr. Michael Sorokopud, and Mr. Greg Kepka from the LUIL department at Lakehead University for their kind support and assistance with the analytical instrumentation. Their expertise and generosity, along with their time, were crucial in facilitating experimental work for this research.

I am grateful to all the members of our research group for creating a friendly, supportive, and collaborative lab environment. I would especially like to acknowledge Dr. Shrikanta Sutradhar, Aakash Chakraborti, and Mehedi Hasan for their continued support, guidance, and companionship in the lab, which have been greatly appreciated.

Finally, I would like to extend my heartfelt thanks to my beloved parents, Suprity Chakma and Swati Talukder, for their unconditional love, endless sacrifices, and unwavering belief in me. Their constant encouragement and emotional support have been the foundation of my strength throughout this academic journey. This achievement is as much theirs as it is mine.

Table of Contents

List of Figures

List of Tables

Abbreviations

AI	Artificial Intelligence
ANFIS	Adaptive Neuro-Fuzzy Inference Systems
ANN	Artificial Neural Networks
BET	Brunauer Emmett Teller
BPNN	Backpropagation Neural Networks
BC	Biochar
CAD	Canadian Dollar
CIP	Ciprofloxacin
CP	Cold Plasma
CT	Computed Tomography
DT	Decision Trees
EDS	Energy Dispersive X-Ray Spectroscopy
EDTA	Ethylenediaminetetraacetic Acid
FC	Fixed Carbon
FTIR	Fourier Transform Infrared Spectroscopy
GBR	Gradient Boosting Regression
GO	Graphene Oxide
GOA	Grasshopper Optimization Algorithm
GP	Gaussian Process
HHV	Higher Heating Value
IBU	Ibuprofen
KNN	K-Nearest Neighbors
LCA	Life Cycle Assessment
MB	Methylene Blue
MBC	Magnetic Biochar
ML	Machine Learning
MLP	Multi-Layer Perceptron
MLP-NN	Multilayer Perceptron Neural Networks
MW	Maple Wood
nZVI	Nano Zero-Valent Iron
PFAS	Polyfluoroalkyl Substances
pH_{PZC}	Point Of Zero Charge
RBBR	Remazol Brilliant Blue R
RBFN	Radial Basis Function Network
Redox	Oxidation-Reduction
RF	Random Forests
RM	Red Mud
RSM	Response Surface Methodology

RSML	Rough Set Machine Learning
SEM	Scanning Electron Microscopy
SSA	Specific Surface Area
SVM	Support Vector Machine
TC	Tetracycline
TEA	Techno-Economic Assessment
VM	Volatile Matter
XGB	Extreme Gradient Boosting
XPS	X-Ray Photoelectron Spectroscopy
XRD	X-Ray Diffraction
ZP	Zeta Potential
ZVI	Zero-Valent Iron

Chapter 1 Introduction

1.1. Background

Water is a fundamental resource supporting all life forms on Earth, playing a critical role in ecological balance, human health, agricultural productivity, and industrial development. Although approximately 3% of the Earth's water is freshwater, only a small fraction is accessible for human use, making the preservation of water resources essential for human survival [1]. Additionally, protecting aquatic ecosystems is essential, as pollutants can bioaccumulate in the food chain, ultimately impacting human health [2]. However, as industrialization progresses, the demand for water increases, leading to its extensive use in manufacturing processes. Due to efficient access to resources, industries are often built near water bodies. These industries can cause water contamination through the discharge of untreated or inadequately treated waste into rivers or lakes, including dyes, heavy metals, and chemicals. For example, Bangladesh, a major textile exporter, generates vast amounts of dye-laden wastewater, often discharged untreated into rivers, contaminating water sources with toxic azo dyes like Reactive Blue, Orange-II, and Acid Black [3-5]. In Canada, while the textile sector is smaller, dye pollution from paper mills and wastewater treatment plants has been detected in major freshwater bodies, including the Great Lakes [6]. Heavy metal pollution is another critical issue, primarily arising from industrial emissions, mining, and improper waste disposal. Canada faces heavy metal contamination, particularly in mining-intensive regions such as Ontario, Quebec, and British Columbia. In Canada, mining regions like Sudbury, Ontario, have reported high Cu and Ni contamination [7]. It has been reported that industrial waste and aging infrastructure contribute to localized Pb pollution, disproportionately impacting Indigenous communities [8]. The presence of Pb in Canadian water bodies has been linked to historical leaded gasoline usage, mining waste runoff, and lead pipe infrastructure in older cities [9]. Water contamination by synthetic dyes and heavy metals is a significant global concern due to their persistence, toxicity, and environmental impact. Chronic exposure to these pollutants can cause neurological disorders, kidney failure, and developmental issues in children [10, 11].

The persistence of dyes and heavy metals in aquatic environments highlights the urgent need for an effective solution. Adsorption is widely regarded as an effective and sustainable method for wastewater treatment due to its simplicity, cost-effectiveness, and high efficiency in removing a wide range of contaminants. Unlike conventional methods such as chemical precipitation or membrane filtration, adsorption does not generate harmful by-products or require extensive energy input. Additionally, adsorbents can often be regenerated and reused, making adsorption a more environmentally friendly solution for wastewater remediation [12, 13].

Biochar (BC), a carbon-rich material produced through the pyrolysis of biomass, has attracted significant interest as an adsorbent due to its high surface area, porosity, and tunable surface chemistry [14]. Canada's extensive forest resources, covering approximately 347 million hectares and representing about 9% of the world's total forest area, make it one of the leading producers of biomass, including agricultural and forestry residues [15]. The choice of maple wood as a biomass source for BC production is driven by its abundance across Canada, particularly in the eastern provinces of Ontario, Quebec, and the Atlantic provinces [16]. Maple wood, rich in lignocellulosic components, cellulose (42~47%), hemicellulose (~30.4%), and lignin (21~23.3%), contains inherent functional groups that can enhance BC's adsorption properties [17, 18]. One limitation of conventional BC is the difficulty in separating it from treated water, which can lead to secondary contamination. This issue can be overcome by impregnating BC with magnetic materials such as FeO, Fe_3O_4, or $FeCl_3$, creating magnetic biochar (MBC), enabling rapid and easy recovery using an external magnetic field. Recently, there has been research on promising alternatives for this iron precursor to produce MBC.

Red mud (RM) is a highly alkaline and iron oxide-rich material, making it a potential replacement for synthetic iron precursors in MBC synthesis. RM, a by-product of alumina production from bauxite ore, is a major industrial waste problem worldwide. On average, 1.25 tonnes of RM is produced for every tonne of alumina, with global refineries generating an estimated 177.25 million tonnes in 2023 [19]. Canada, a major player in the aluminum industry with 3.3 million tonnes of production in 2023, also contributes significantly to RM production, especially in regions like Quebec, home to key alumina refineries [20]. However, due to its high alkalinity and metal content, improper disposal of RM leads to severe environmental issues, including soil and water contamination. Given its abundance and unique composition, utilizing RM as a BC modifier not only enhances its adsorption capacity but also promotes mineral processing waste valorization, contributing to a circular economy and reducing landfill burdens. By engineering BC with RM and other chemical modifiers, this study aims to enhance the functionality of MBC for wastewater treatment while addressing the environmental challenges associated with RM disposal. This approach aligns with the broader goal of developing cost-effective, sustainable adsorbents for water remediation.

1.2. Specific objectives for this study and thesis organization

I. Synthesize MBC with different iron anchoring methods and evaluate their application in wastewater treatment, particularly for the removal of organic pollutants such as dyes.
II. Synthesize acid and alkali-modified MBC with RM and investigate their application in the adsorption and removal of heavy metals from aqueous solutions.

The following chapters are presented in this thesis to address the targeted objectives and novelty of this work:

Chapter 1: The background, objectives, and significance of the research are introduced, along with an overview of the thesis organizational structure.

Chapter 2: A literature review is provided on the design, synthesis, modification, and application of BC for heavy metal removal from water. Key modification methods, adsorption mechanisms, and recent advancements are discussed. (Published in *Canadian Journal of Chemical Engineering*)

Chapter 3: Presents experimental findings on MBC synthesized from maple wood using various iron-anchoring methods and their performance in dye removal from water. (Manuscript is under review in a peer-reviewed journal)

Chapter 4: Reports on the synthesis of industrial waste-based MBC through pre-pyrolysis activation, focusing on its enhanced adsorption of Cu and Pb, and includes a comparative economic analysis. (Manuscript is under review in a peer-reviewed journal)

Chapter 5: Summarizes the key findings of the research, highlighting its implications, limitations, and suggesting future research directions

References

[1] W. Musie and G. Gonfa, "Fresh water resource, scarcity, water salinity challenges and possible remedies: A review," *Heliyon,* vol. 9, no. 8, 2023, doi: 10.1016/j.heliyon.2023.e18685.

[2] S. Ray and R. Vashishth, "From water to plate: Reviewing the bioaccumulation of heavy metals in fish and unraveling human health risks in the food chain," *Emerging Contaminants,* vol. 10, no. 4, p. 100358, 2024/12/01/ 2024, doi: https://doi.org/10.1016/j.emcon.2024.100358.

[3] S. N. Sakib. "Garment industry in Bangladesh struggles to contain pollution." Dialogue Earth. https://dialogue.earth/en/pollution/garment-industry-bangladesh-struggles-to-contain-pollution/ (accessed March 15, 2025).

[4] F. Akter and Y. Dong, "Investigation of removing orange II azo dye from wastewater through an oxidation process," *Applied Water Science,* vol. 14, no. 11, p. 243, 2024/10/30 2024, doi: 10.1007/s13201-024-02311-2.

[5] H. Regan, "Asian rivers are turning black. And our colorful closets are to blame," CNN, September 28, 2020. [Online]. Available: https://www.cnn.com/style/article/dyeing-pollution-fashion-intl-hnk-dst-sept

[6] A. A. Adesida *et al.*, "Simultaneous degradation of persistent organic pollutants and heavy metal removal via an electrochemical filtration system: A case study on a pulp mill wastewater effluent," *Case Studies in Chemical and Environmental Engineering,* vol. 6, p. 100258, 2022/12/01/ 2022, doi: https://doi.org/10.1016/j.cscee.2022.100258.

[7] T. A. Jackson, N. Nguyen, and W.-C. Li, "Effects of Copper, Nickel, and Sulfate from the Smelters at Sudbury, Ontario (Canada) on Microbial Communities in Lakes," *Geomicrobiology Journal,* vol. 34, no. 5, pp. 400-420, 2017/05/28 2017, doi: 10.1080/01490451.2016.1204375.

[8] S. Law, "Mercury poisoning near Grassy Narrows First Nation worsened by industrial pollution, study suggests," CBC News, May 23, 2024. [Online]. Available: https://www.cbc.ca/news/canada/thunder-bay/grassy-narrows-first-nation-methylmercury-study-1.7211750

[9] H. Canada, "Lead in Canadians," Ottawa, ON, December 14, 2021. [Online]. Available: https://www.canada.ca/en/health-canada/services/environmental-workplace-

health/reports-publications/environmental-contaminants/human-biomonitoring-resources/lead-canadians.html

[10] W. Waqas *et al.*, "Toxic effects of heavy metals on crustaceans and associated health risks in humans: a review," *Environmental Chemistry Letters,* vol. 22, no. 3, pp. 1391-1411, 2024/06/01 2024, doi: 10.1007/s10311-024-01717-3.

[11] H. Kolya and C.-W. Kang, "Toxicity of Metal Oxides, Dyes, and Dissolved Organic Matter in Water: Implications for the Environment and Human Health," *Toxics,* vol. 12, no. 2, p. 111, 2024. [Online]. Available: https://www.mdpi.com/2305-6304/12/2/111.

[12] J. Bayuo, M. J. Rwiza, J. W. Choi, K. M. Mtei, A. Hosseini-Bandegharaei, and M. Sillanpää, "Adsorption and desorption processes of toxic heavy metals, regeneration and reusability of spent adsorbents: Economic and environmental sustainability approach," *Advances in Colloid and Interface Science,* vol. 329, p. 103196, 2024/07/01/ 2024, doi: https://doi.org/10.1016/j.cis.2024.103196.

[13] N. El Messaoudi *et al.*, "Regeneration and reusability of non-conventional low-cost adsorbents to remove dyes from wastewaters in multiple consecutive adsorption–desorption cycles: a review," *Biomass Conversion and Biorefinery,* vol. 14, no. 11, pp. 11739-11756, 2024/06/01 2024, doi: 10.1007/s13399-022-03604-9.

[14] L. Leng *et al.*, "An overview on engineering the surface area and porosity of biochar," *Science of The Total Environment,* vol. 763, p. 144204, 2021/04/01/ 2021, doi: https://doi.org/10.1016/j.scitotenv.2020.144204.

[15] N. R. Canada, "The State of Canada's Forests: Annual Report 2023," 2023. Accessed: March 14, 2025. [Online]. Available: https://natural-resources.canada.ca/sites/nrcan/files/forest/sof2023/NRCAN_SofForest_Annual_2023_EN_accessible-vf(1).pdf

[16] Tim. "10 Native Types of Maple Trees in Canada." Arborist Halifax. https://arboristhalifax.ca/maple-trees-in-canada/ (accessed March 18, 2025).

[17] X. He *et al.*, "Pivotal factors of wood-derived electrode for supercapacitor: Component striping, specific surface area and functional group at surface," *Carbon,* vol. 210, p. 118090, 2023/06/15/ 2023, doi: https://doi.org/10.1016/j.carbon.2023.118090.

[18] B. Koohestani, A. Koubaa, T. Belem, B. Bussière, and H. Bouzahzah, "Experimental investigation of mechanical and microstructural properties of cemented paste backfill

containing maple-wood filler," *Construction and Building Materials,* vol. 121, pp. 222-228, 2016/09/15/ 2016, doi: https://doi.org/10.1016/j.conbuildmat.2016.05.118.

[19] R. Majumder. "Red mud generation trend across major countries, 2018 to 2023." AL Circle. https://www.alcircle.com/news/red-mud-generation-trend-across-major-countries-2018-to-2023-112752 (accessed March 13, 2025).

[20] N. R. Canada. "Aluminum facts." Natural Resources Canada. https://natural-resources.canada.ca/minerals-mining/mining-data-statistics-analysis/minerals-metals-facts/aluminum-facts#a4 (accessed March 15, 2025).

Chapter 2 Review of recent advances in the design, synthesis, and modification of biochar for remediation of heavy metal pollution in water

Abstract

Heavy metal contamination of water has long been a serious environmental issue. Biochar (BC) and BC-based composites are emerging as effective and sustainable solutions for heavy metal removal due to their strong adsorption abilities and environmentally friendly nature. This review focuses on the latest developments in designing, producing, and modifying BC for heavy metal remediation. It discusses key factors like biomass selection, pyrolysis conditions, and activation processes that influence BC properties. Methods for preparing magnetic biochar (MBC), including pre-pyrolysis treatment, co-pyrolysis, and post-pyrolysis modification, are explained. The review highlights the importance of BC properties that impact their functionality in heavy metal adsorption. The latest progress in different modification methods, physical, chemical, and biological, are also discussed. Additionally, it discusses the primary characterization techniques used for BC characterization and performance evaluations. The review also examines in-depth how BC is functioning in removing specific heavy metals like cadmium, chromium, lead, and nickel. It explains adsorption kinetics, mechanisms, and modeling, and explores ways to regenerate and reuse BC. The potential of machine learning to optimize BC applications in wastewater treatment is discussed. Finally, the review considers Life Cycle Assessment (LCA) and Techno-Economic Assessment (TEA) to evaluate the sustainability and cost-effectiveness of BC use. The paper concludes by identifying knowledge gaps and suggesting future research directions to further improve BC technologies for wastewater treatment.

*Chapter 2 has been accepted for publication as a review paper in the *Canadian Journal of Chemical Engineering*.

2.1. Introduction

The environmental impact of heavy metal pollution, resulting from industrial activities, agriculture, and improper waste management, poses a severe threat to ecosystems and human health. Thus, developing cost-effective, sustainable, and efficient treatment technologies is imperative. Biochar (BC), a carbon-rich material derived from the thermochemical conversion of biomass, has gained significant attention in recent years in environmental remediation. Among its various uses, BC's effectiveness in wastewater treatment has been extensively explored due to its high surface area, porous structure, and abundance of functional groups that enable the adsorption of contaminants, including heavy metals.

This review comprehensively examines the recent advances in the design, synthesis, and modification of BC and BC-based composites for wastewater treatment. While previous reviews have highlighted the basic principles of BC's adsorption capabilities, this work is unique in providing a detailed analysis of the impact of various modification techniques on enhancing BC’s adsorption performance, particularly for heavy metals. Furthermore, the review addresses the latest innovative strategies for BC modification, such as magnetic functionalization, chemical and biological treatments, and their implications on adsorption mechanisms.

The originality of this review lies in its comprehensive assessment of BC's evolving role in wastewater treatment, with a particular focus on the impact of tailored modification strategies in enhancing its performance. This work critically examines recent advancements in BC functionalization for improved selectivity, the influence of feedstock selection and pyrolysis conditions on adsorption efficiency, and the challenges associated with large-scale applications. Additionally, the review identifies key research gaps, including the long-term stability of BC in dynamic wastewater environments and the potential risks of secondary environmental impacts. By addressing both the current limitations and future directions in BC-based heavy metal remediation, this review provides novel insights into optimizing BC design and application for sustainable and efficient wastewater treatment.

Furthermore, this review explores emerging interdisciplinary frontiers, including the integration of machine learning (ML) and artificial intelligence (AI) in BC research. ML and AI-based approaches have shown potential in optimizing BC synthesis conditions, predicting adsorption efficiencies, and modeling complex interactions between BC and contaminants. The application of AI-driven computational modeling and predictive analytics is expected to accelerate the design of next-generation BC materials, reducing reliance on costly and time-consuming experimental trials.

Additionally, this review looks into the feasibility of BC-based treatment technologies by assessing existing Life Cycle Assessment (LCA) and Techno-Economic Assessment (TEA) studies. These methodologies provide a comprehensive assessment of BC's environmental footprint, energy efficiency, and cost-effectiveness across different production and application scenarios. While BC is often considered a sustainable adsorbent, factors such as feedstock selection, pyrolysis conditions, and post-treatment modifications significantly influence its overall environmental impact. This review presents an up-to-date analysis of LCA and TEA studies to identify sustainable pathways for large-scale implementation.

In summary, this review aims to provide a comprehensive and forward-looking perspective on BC development for wastewater treatment. By integrating recent breakthroughs in BC modification, AI-driven optimization, and sustainability assessments, this work serves as a valuable resource for researchers and practitioners seeking to develop next-generation BC materials with enhanced performance and environmental sustainability.

2.2. Biochar synthesis and functionalization for heavy metal remediation

2.2.1. Impacts of biomass resources and biochar production methods

The production methods of BC significantly influence its ability to adsorb heavy metals; hence, choosing production parameters is crucial for optimizing BC as an effective adsorbent. The type of reactor, pyrolysis conditions, temperature, and pressure all play pivotal roles in determining the BC's physicochemical properties, affecting its adsorption capacity. **Figure 2.1** summarizes and illustrates the biomass resource selection criteria, activation/modification processes, and optimal pyrolysis parameters for producing high-quality BC for heavy metal removal.

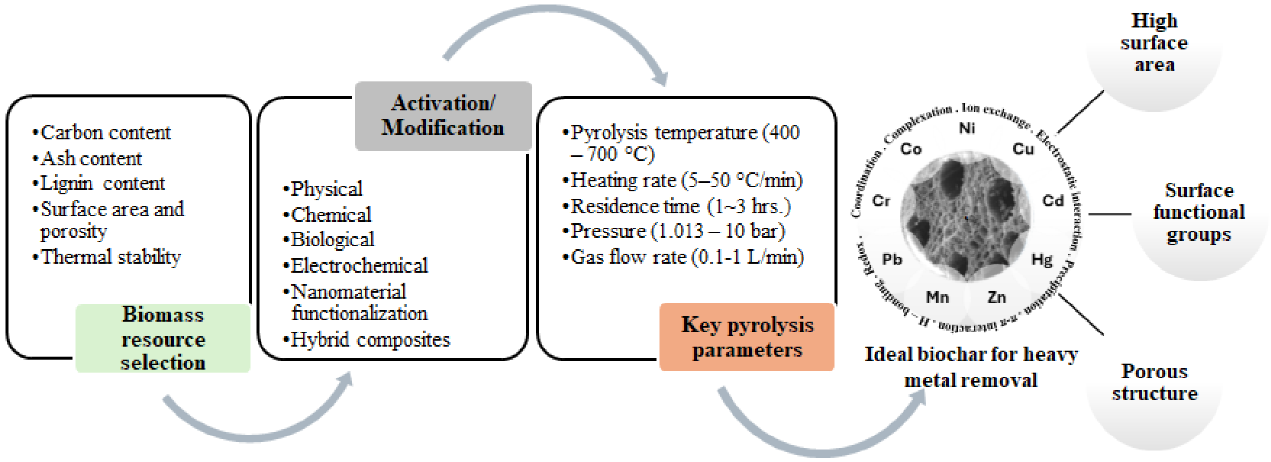

Figure 2.1 Key parameters for producing optimal BC for heavy metal removal

Biomass resource selection

Biomass refers to organic matter obtained from living or recently deceased organisms, predominantly plants and plant-based substances, along with animal waste. The properties of biomass significantly influence BC's heavy metal adsorption capacity. These include factors such as the type of biomass, its chemical composition, and inherent mineral content, which play critical roles. Feedstocks rich in lignin, like wood, tend to produce BC with higher carbon content, lower ash content, and a fine aromatic structure due to lignin breakdown. In contrast, cellulose-rich feedstocks, such as agricultural residues, generally yield BC with lower carbon content, higher ash content, and an improved porous structure from the breakdown of cellulose. [1, 2]. For example, corn cob residue-based BC, due to its high lignin content, exhibits a highly porous structure, leading to improved adsorption of heavy metals like Pb(II), Cu(II), and Cd(II) from wastewater [3]. In addition to organic content, the mineral composition of the biomass also affects the adsorption efficiency [4]. BC produced from biomass containing calcium, magnesium, and potassium tends to form metal precipitates such as hydroxides and carbonates, facilitating the adsorption of metals [5]. For instance, the study by Vaičiukynienė et al. [6] demonstrated that BC derived from alkali-activated slag, which is rich in minerals, showed enhanced Pb(II) adsorption due to the precipitation of $Pb_3(CO_3)_2(OH)_2$ on the BC surface. Moreover, specific functional groups in the biomass, such as carboxyl, hydroxyl, and phenolic groups, contribute to the BC's ability to adsorb heavy metals through mechanisms like ion exchange, complexation, and precipitation. For example, BC produced from Douglas fir wood, which is rich in carboxyl and hydroxyl groups, was found to exhibit high adsorption capacities for Cr(VI), Pb(II), and Cd(II) due to the formation of stable metal-organic complexes [7].

Pyrolysis temperature

The pyrolysis reaction temperature is a critical factor that significantly affects the properties of BC, thereby influencing its capacity for heavy metal adsorption. Raising the pyrolysis temperature generally improves BC's adsorption performance by increasing porosity, enhancing the conversion of organic compounds, and enriching its surface functional groups [8]. At lower pyrolysis temperatures (e.g., 300–400 °C), BC tends to retain more functional groups [9]. These functional groups are known to enhance the adsorption of heavy metals through mechanisms like surface complexation and ion exchange. Ma et al. [10] found that BCs produced at lower temperatures (300–400 °C) effectively adsorb Cr(VI) due to the abundance of functional groups (-OH, -COOH), facilitating adsorption through electrostatic interactions, complexation, and reduction. As the pyrolysis temperature increases to a moderate level (e.g., 500–700 °C), the BC undergoes a greater degree of carbonization, leading to a more aromatic structure and a significant reduction in volatile matter. Higher temperatures also contribute to the development of a larger surface area and increased porosity, which are crucial for physical adsorption mechanisms. A study by Wang et al. [11] demonstrated that BC produced at 600 °C had a much higher surface area than that produced at lower temperatures (300, 400 °C), resulting in a greater adsorption capacity of 124.7 mg/g for Pb(II). However, high pyrolysis temperatures (above 700 °C) may reduce the functional groups on the BC surface, potentially decreasing their chemical adsorption capabilities [9, 12]. Despite this, the highly porous structure formed with high aromaticity at these temperatures can still support high adsorption capacities through physical adsorption [11, 13, 14]. Soares et al. [14] reported that BC produced at 750 °C exhibited an increased surface area and enhanced adsorption capacity for As(II) and Pb(II) compared to that produced at 350 °C.

BC retains more functional groups at lower temperatures (<400 °C), enhancing chemical adsorption via surface complexation and ion exchange. As temperature increases to 500–700 °C, BC undergoes more complete carbonization, resulting in higher surface area and porosity, which improves physical adsorption. However, very high temperatures (>700 °C) may reduce functional groups, but still can promote adsorption through a highly porous structure. Thus, an optimal pyrolysis range of 500–700 °C is ideal for balancing functional group retention and enhanced porosity, maximizing BC's adsorption efficiency.

Pyrolysis heating rate, pressure, and residence time

The heating rate during pyrolysis plays a critical role in determining the physicochemical properties of BC, which directly influence its effectiveness as an adsorbent. For instance, Li et al. [15] explored how varying heating rates impact BC's functional groups and structural properties derived from lignin pyrolysis. At lower heating rates, such as 10 °C/min, the pyrolysis process favors the preservation of organic structures like phenolic compounds with conjugated π-bonds, while higher rates, like 20 °C/min, promote further decomposition of these organic structures, leading to significant changes in the BC's surface chemistry and functionality [15]. Higher heating rates facilitate the cracking of aliphatic compounds and promote deoxygenation and dehydrogenation of organic components, leading to increased production of gaseous by-products. This rapid heating results in BC with a lower carbon content and higher oxygen retention, which correlates with a reduced higher heating value (HHV) of the BC. Another study by Shagali et al. [16] examined the effects of varying heating rates (10-40 °C/min) at a moderate pyrolysis temperature of 700 °C on walnut shell BC. They observed that increasing the heating rate influenced the yield and porosity of the BC, with KOH-activated BC yielding the highest (40% dry basis) due to dehydrogenation reactions, while steam-activated BC developed more micropores. Additionally, a slower heating rate (10 °C/min) resulted in a broader -OH stretching peak, indicative of more pronounced alcohol groups, whereas higher rates (40 °C/min) led to the deformation of carboxylic acid derivatives [16].

Pressure is another critical parameter controlling pyrolysis, significantly influencing BC yield and quality. Typically, pyrolysis is conducted at atmospheric pressure, but variations in reactor pressure can lead to notable differences in the characteristics of the resulting BC. A study by Rasaq et al. [17] demonstrated that pressures between 0 and 5 bars significantly affected the quality and characteristics of the products, improving dehydrogenation and deoxygenation reactions in bio-oil and increasing gas yields of CH_4, H_2, and CO_2. Higher pressures also enhance BC's compactness and structural integrity despite minimal changes to its combustible features [17].

The choice of an inert atmosphere, such as nitrogen or argon, also affects the surface chemistry of BC. Recent studies show that the presence of CO_2 during pyrolysis can positively influence the

HHV of bio-oil, while N_2 tends to decompose high calorific value components, reducing HHV [18]. They also reported that the N_2/CO_2 ratio favors the production of alcohols and phenols in bio-oil, with N_2 enhancing benzene formation and CO_2 contributing to carboxylic acids.

As a summary, generally, lower heating rates (e.g., 10 °C/min) favor preserving functional groups, such as phenolics and alcohols, which enhance chemical adsorption, while higher rates (e.g., 20-40 °C/min) promote porosity but reduce functional groups. Moderate pressures (0-5 bars) improve BC's structural integrity without compromising adsorption efficiency. Regarding the atmosphere, inert gases like N_2 are generally favorable, though CO_2 can enhance certain functional properties.

2.2.2. Synthesis of MBC for heavy metal removal

Magnetic modification of BC involves embedding magnetic nanoparticles, such as iron oxides, into the BC matrix, enhancing its pollutant adsorption and recovery capabilities. This can be achieved through biomass pre-treatment with iron salts, post-pyrolysis impregnation, or co-pyrolysis with iron precursors, as shown in **Figure 2.2**.

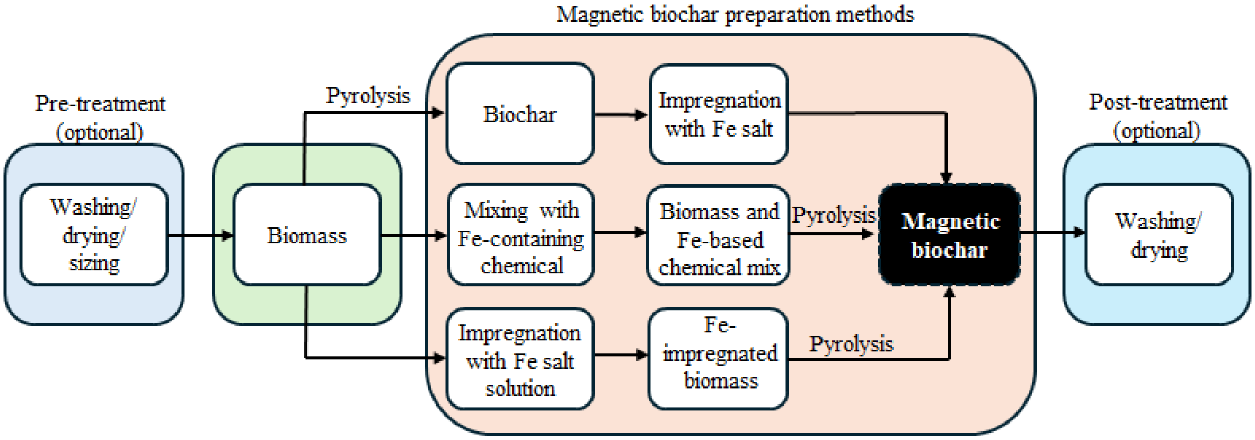

Figure 2.2 Different methods used for producing MBC

Pre-pyrolysis treatment

Recent research studies have investigated the production of MBC by impregnating biomass with iron (Fe) salts [19-21]. The process typically involves the immersion of selected biomass feedstock in a solution containing specific iron salts (such as $FeCl_3$ and $FeSO_4$), facilitating the absorption of iron by the biomass. The absorption of iron salts by the biomass leads to the formation of iron-containing compounds within the BC structure during subsequent thermal decomposition and pyrolysis. The incorporation of iron into the BC matrix is believed to occur through mechanisms such as chemical reactions, thermal decomposition, and redox processes, leading to the formation of magnetic phases or nanoparticles within the BC. One of the critical factors for this process is maintaining a suitable impregnation ratio. Choosing the proper impregnation ratio is recommended to get the targeted result. The pore formation can be hindered by the high impregnation ratio of metal salts to biomass (higher than 0.5), resulting in lower adsorption [22]. A study showed that MBC prepared by a lower impregnation ratio (0.3) showed good adsorption quality on Tetracycline. In comparison, the higher ratio (0.6) gave better results in removing heavy metals, Pb(II) and Cd(II) [23].

Co-pyrolysis

Co-pyrolysis is a one-step thermochemical conversion process incorporating magnetic nanoparticles into BC. **Figure 2.2** shows the simplified flow chart of how MBC can be produced through co-pyrolysis of biomass with Fe-containing chemicals, such as FeO, red mud, etc. When a physical mixture of biomass and Fe-based chemicals is subjected to pyrolysis, the resulting BC exhibits magnetic properties due to the presence of magnetic nanoparticles. The iron particles present in the initial physical mixture get dispersed within the BC matrix during the pyrolysis. Magnetic properties arise from retaining Fe particles within the carbonaceous structure of the BC. This inclusion allows BC to acquire magnetic behavior due to the inherent magnetic properties of iron oxide. Recently, there have been many advances in producing MBC by co-pyrolysis of the biomass with magnetic nanoparticles, which can be materials like hematite (Fe_2O_3), magnetite (Fe_3O_4), or nano zero-valent iron (nZVI) [24, 25]. In a particular research investigation, MBC was generated through co-pyrolysis by introducing steel dust particles into the process [26]. The resulting BC exhibited enhancements in terms of its heterogeneity, crystalline structure, and the presence of surface functional groups.

Post-pyrolysis treatment

Post-pyrolysis modification with iron precursors is also used to enhance BC's properties for environmental applications, particularly in contaminant removal. Incorporating iron species such as iron salts (e.g., $FeCl_3$, $FeSO_4$), iron oxides (e.g., Fe_2O_3, Fe_3O_4), or zero-valent iron (ZVI) into BC through methods like impregnation, co-precipitation, and thermal treatment. This is a two-step synthesis process involving biomass's thermochemical conversion into BC in the first step, followed by doping the BC into Fe-containing salt solutions. For instance, Wang et al. [27]

prepared MBC through a post-pyrolysis treatment process, where BC was first produced from rice straw at 500 °C, followed by impregnation in a mixture of $FeSO_4$ and $FeCl_3$. Similarly, Li et al. [28] produced MBC from corncob by first pyrolyzing it at 500°C. The resulting BC was then suspended in 100 mL of ultrapure water, followed by the addition of 290 mL of a mixed solution containing ferric nitrate (18.7 g/L) and ferrous sulfate (133.3 g/L) at pH 10.6, and stirred for 2 hours to obtain MBC. However, this method can be more time-consuming and expensive due to the additional processing steps required after pyrolysis.

In summary, selecting an appropriate synthesis method and optimizing process parameters is crucial to producing high-quality MBC. Among the available techniques, co-pyrolysis of biomass with iron precursors offers a straightforward and economically viable approach, as it integrates magnetic nanoparticle formation during BC production without requiring additional post-treatment steps. Optimizing the impregnation ratio, which is the amount of chemical agent or metal impregnated onto an adsorbent relative to the adsorbent's weight, is vital as lower ratios improve the adsorption of organic pollutants, while higher ratios enhance heavy metal removal. By carefully balancing these factors, it is possible to produce MBC that is both cost-effective and efficient for environmental remediation applications.

2.2.3. Desirable properties of biochar for heavy metal removal

Surface area

BC typically possesses a high surface area due to its porous structure, which allows for a greater contact area between the BC particles and the heavy metal ions in the wastewater. As a result, more heavy metal ions can attach to the surface of the BC, increasing the adsorption capacity. Several studies have demonstrated that an increased surface area enhances the adsorption capacity of BC for contaminants. Wani et al. [29] showed that several factors, including pyrolysis temperature and volatile matter (VM) content, influenced the surface area of BC. Higher pyrolysis temperatures promote carbonization, leading to increased surface area, while elevated volatile matter content tends to reduce surface area by clogging micropores [29]. Optimizing pyrolysis conditions, such as increasing temperature and minimizing ash content, is essential for maximizing the surface area, particularly for wood-based BC, demonstrating a more pronounced response than other biomass types like rice husks or straw. Li et al. [30] found that BC made from fish scales had an enhanced surface area of 3370 m^2/g, effectively removing ciprofloxacin from aqueous solutions. Herath et al. [7] demonstrated that enhancing the BC's surface area from 535 to 1050 m^2/g through KOH activation significantly boosted its adsorption capacity for Cr(VI), Pb(II), and Cd(II) to 127.2, 140, and 29 mg/g, respectively, from aqueous solutions. Furthermore, the presence of meso and micropores in BC enhances surface area accessibility and promotes diffusion of contaminants into the interior of the adsorbent, ensuring efficient removal from aqueous solutions [31]. Meso- and micropores facilitate mass transfer by providing a network of transport pathways (mesopores) and abundant active sites (micropores) for adsorption.

An optimal BC adsorbent should have a high surface area, ideally above 400 m^2/g, to maximize active sites for contaminant interaction. However, surface area alone is insufficient; a balance with abundant functional groups like hydroxyl and carboxyl enhances adsorption mechanisms. A well-developed pore structure also aids in achieving efficient contaminant removal.

Surface functional groups

BC can have various functional groups, such as hydroxyl, carboxylic, carbonyl, ether, phenolic, and ketone groups, contributing to its applications in heavy metal removal. They can be categorized as Oxygen (O), Nitrogen (N), and Sulfur (S), containing functional groups according to their bonding on carbon surfaces, commonly oxygen, nitrogen, sulfur, phosphorus, and halogens [32, 33]. Their abundance is preparation temperature dependent, as the number of functional groups (hydroxyl, carboxylic, and amino groups) decreases with increasing temperature, mainly due to their advanced carbonization level [34, 35].

O-functional groups

Oxygen (O) functional groups contribute to its hydrophilic properties and ability to interact with water molecules and other polar compounds. Hydroxyl and carboxylic groups, the two main O-functional groups, create active sites on the surface of BC that can chemically bind to heavy metal ions through surface complexation, hydrogen bonding, and pH-dependent charge interactions [36]. These interactions increase the adsorption capacity of BC for heavy metals, making it an effective material for environmental remediation. Previous studies show that the binding capacity of O-functional groups leads to effective Cu(II) adsorption in an aqueous solution [33]. The O-functional groups also greatly affect the adsorption of Pb(II) and Cd(II) by involving in complexation with the heavy metals [35].

N-functional groups

N-functional groups on BC have a wide variety of applications, like the adsorption of heavy metals (Pb, Cd, Cu) and organics, as well as catalytic performance [37, 38]. Pyrrolic, pyridinic, and amine groups are the major N-functional groups that can enhance the adsorption capacity of BC due to their ability to form coordination bonds with heavy metal ions. N-functional groups show the formation of electrostatic attraction, hydrogen bonding, and chelation that can create active sites on BC surfaces and help bind with metal ions [39]. The electron-rich nature of nitrogen facilitates the binding of metal ions through complexation reactions, leading to the formation of stable surface complexes. These functional groups can also modify the surface charge of BC, thereby influencing the electrostatic interactions between the BC surface and metal ions in the solution.

S-Functional groups

S-functional groups found in BC primarily include thiol (-SH), sulfide (-S-), and sulfate ($-SO_3H$) groups, which contribute to the chemical reactivity of BC, influencing its capacity to adsorb heavy metals and organic pollutants. These functional groups rarely appear on BC due to the low Sulfur content of biomass and can degrade with temperature variability [40, 41]. Rather, they have to be introduced through special methods. Over the years, many methods have been developed to synthesize BC with S-functional groups, such as sulfurization and molten salt process [42, 43]. These functional groups interact with pollutants and heavy metals in water through chemical coordination. They can create more binding sites and show ion exchange property that facilitates the removal of Pb(II) and Cu(II) [43].

Other functional groups

Other than the dominant functional groups mentioned above, some phenolic groups, carbonyl groups, alkyl groups, and some aromatic rings can also be present in BC. Phenolic groups contain oxygen atoms, allowing them to form complexation bonds with metal ions through ligand exchange or coordination interactions. Earlier research suggests that the primary catalysts for the reduction of Cr(VI) are the phenolic groups found in BC [44, 45]. Another study shows that activated carbons rich in phosphorus-containing functional groups are much more efficient in adsorbing Cd(II) and Co(II) from aqueous solution [46]. Carbonyl groups, formed during pyrolysis, can affect the BC's reactivity and ability to participate in chemical reactions. Carbonyl groups on BC surfaces can undergo redox reactions, providing reactive sites for heavy metal binding. The oxygen in carbonyl groups can form coordination bonds with heavy metal ions, facilitating adsorption. Alkyl groups, derived from the original biomass, can be present in BC. Alkyl groups contribute to the hydrophobic nature of BC, promoting interactions with hydrophobic heavy metal species. Alkyl groups may participate in complexation reactions, influencing the adsorption of certain metal ions. Aromatic structures may contribute to the BC's stability and adsorption characteristics. Aromatic structures can engage in π-π interactions with heavy metal ions, contributing to adsorption. Aromatic rings can also act as electron donor sites, forming coordination bonds with heavy metals.

In summary, for developing an effective adsorbent, the desired surface functional groups would include a mix of O-functional and N-functional groups due to their strong ability to form stable complexes with heavy metals. Functional groups such as hydroxyl, carboxyl, carbonyl, phenolic, pyrrolic, and thiol contribute to BC's reactivity and adsorption capacity. O-functional groups, especially hydroxyl and carboxyl, are crucial for forming surface complexes and hydrogen bonds with metal ions. N-functional groups, like pyrrolic and amine, improve adsorption through electrostatic attraction, hydrogen bonding, and chelation. S-functional groups, such as thiol and sulfate, though less common, can be synthetically introduced to increase the removal efficiency of metals like Pb and Cu.

Porous structure

The rich porous structure of BC provides numerous benefits that contribute to its adsorption capacity and overall efficacy in heavy metal removal. BC is composed of numerous pores and cavities of varying sizes. These pores provide sites for heavy metal ions to adsorb physically onto the BC surface. Smaller pores can lead to chemical adsorption, while larger pores may facilitate physical adsorption and ion exchange processes. The pores are distributed into three categories according to their varying pore sizes: micropores (<2 nm), mesopores (2–50 nm), and macropores (>50 nm) [47]. Macropores typically facilitate the ease of substance diffusion, mesopores function as effective pathways for mass transfer, and micropores offer spaces to capture and retain substances [48]. BC's porosity is dependent on temperature, as higher temperatures lead to increased porosity within the BC structure [49, 50]. The interconnected pore network allows for rapid diffusion of contaminants into the internal surfaces of BC particles, increasing the contact area between the adsorbent and the aqueous solution. This enhanced accessibility to active adsorption sites facilitates the removal of contaminants through surface complexation, ion exchange, and electrostatic interactions.

The porous structure of BC is crucial for its effectiveness in heavy metal removal, with micropores, mesopores, and macropores providing sites for both physical and chemical adsorption. Macropores enhance diffusion, mesopores aid mass transfer, and micropores retain metal ions. This structure, shaped by pyrolysis temperature, increases the contact area between BC and contaminants, enabling efficient adsorption through surface complexation, ion exchange, and electrostatic interactions. For optimal performance, BC should have a well-developed porous structure and a variety of functional groups, especially oxygen, nitrogen, and sulfur, to form stable complexes with heavy metals.

2.2.4. Modification methods

BC is usually modified to enhance its adsorption capacity, and the appropriate modification method relies on the intended use of BC. For example, activated BC, characterized by increased surface area and porosity, is frequently favored for adsorption applications. There are two main approaches to BC modification: physical and chemical. However, there are also other less-used methods to modify BC, which are illustrated in **Figure 2.3**. Recent studies on BC modification are summarized in **Table 2.1**, presenting the methods used and the properties enhanced in each study. This table provides insight into the progress and application areas of BC modification in recent years.

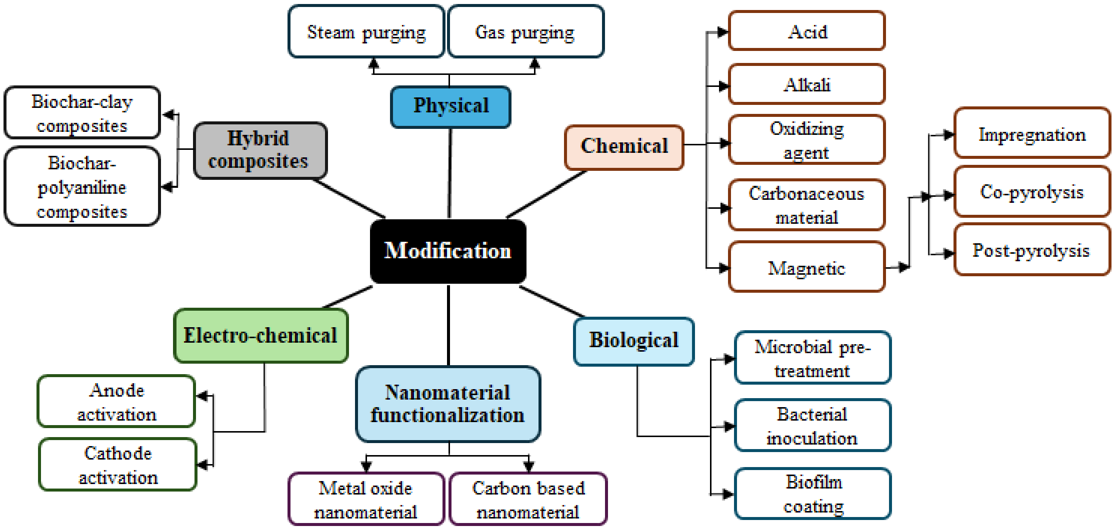

Figure 2.3 Different methods used for BC modification

Table 2.1 Recent adsorption studies on the modified BC

Raw materials	Modifier	Pollutant(s)	Adsorption capacity (mg/g)		Surface Area (m^2/g)	Ref
			Before modification	After modification		
Raspberry stalks	Urea	As(V), Cr(VI)		As = 15.50 Cr = 14.70	117.00	[51]
Pinewood sawdust	Mg/Zn	Micro-plastics	94.81%	Mg-MBC = 98.75% Zn-MBC = 99.46%	221.75	[52]
Peanut shells	Chitosan-EDTA	Pb(II)	10.90	156.68	3.09	[53]
Corn straw	MoS_2	Cd(II)	17.80	139.00	88.30	[54]
Corncob	Ni, Al layered double oxides	Acridine Orange	-	30.74	552.62	[55]
Rape straw	CTAB	Polystyrene; Carboxylate-modified Polystyrene	-	PS = 163.40 CPS = 159.60	683.60	[56]

Raw materials	**Modifier**	**Pollutant(s)**	**Adsorption capacity (mg/g)**		**Surface Area (m^2/g)**	**Ref**
			Before modification	**After modification**		
Cow litter	Phosphate rock	Pb(II); Cd(II)	-	Pb = 451.24 Cd = 120.87	13.66	[57]
Rice straw	Mg/La	PO_4^{3-}	1.21	62.50	-	[58]
Tea waste	Chitosan	Tetracycline; Cu(II)	Cu(II) = 17.30 TC = 471.77	Cu(II) = 65.87 TC = 241.33	646.00	[59]
Wheat straw	Soil indigenous microbes	Cd(II)	6.28	14.42	3.77	[60]

Physical modification

During steam activation, BC undergoes exposure to elevated temperatures, usually ranging from 300 °C to 900 °C, while in the presence of steam [61-63]. This procedure is carefully conducted within a controlled environment to avoid combustion. Steam interacts with the carbon in the BC, initiating gasification and forming oxides and hydrogen [63, 64]. These finally result in the liberation of volatile organic compounds. The elimination of these compounds results in the formation of pores and voids within the structure of the BC, markedly increasing its surface area. For instance, Su et al. [65] produced BC from palm kernel shells using microwave pyrolysis at 700 W and then activated it with steam for 30 minutes. This modification resulted in a BC with a BET surface area of 419 m^2/g, compared to 404 m^2/g for the unmodified BC. Wang et al. [66] activated bamboo-derived BC with steam, which not only increased its surface area and carbon content but also enhanced its ability to remove TC and Cu(II). Steam activation increased the graphitic carbon ratio, benefiting TC removal by facilitating π-acceptor interactions with the TC molecule's aniline ring, while the higher ratio of O-C=O improved hydrogen bonding with TC. Gas purging involves exposing BC to activating gases, such as ozone, CO_2, or air, at elevated temperatures [67]. This process is conducted in the absence of steam. The interaction of gas with carbon in BC involves gasification and the elimination of carbonaceous material, fostering the development of pores and a rise in surface area [68]. Much like steam purging, the utilization of gas purging yields activated

BC characterized by enhanced porosity and surface area, thereby boosting its efficacy in adsorption and catalytic activities.

Chemical modification

Acid modification of BC can introduce new functional groups such as carboxyl (-COOH), hydroxyl (-OH), and ketone (C=O) on the BC surface. Introducing functional groups increases the number of active sites available for chemical interactions, creates pores, and increases surface area, improving the BC's ability to adsorb contaminants, such as heavy metals and organic pollutants, from water and soil. A study showed that BC derived from rice straw, when modified with an equal mixture of H_2O_2 and HNO_3, exhibited a twofold increase in surface carboxyl and phenol groups, resulting in an enhanced Cd(II) adsorption capacity of 93.2 mg/g, compared to 69.3 mg/g for unmodified BC [69]. In comparison to the unmodified BC, this process also raised the surface area, carboxyl groups, and phenol groups by 22%, 124.1%, and 111.3%, respectively [69]. Another study showed that BC modified with H_2SO_4 showed a significant increase in surface area and O-containing functional groups, resulting in 1.57 times higher NH^{4+} adsorption capacity than the unmodified BC [70].

The alkali modification of BC includes subjecting BC to alkaline substances or solutions with the intention of changing its chemical composition and surface characteristics. Frequently employed alkaline agents for this process encompass hydroxides such as potassium hydroxide (KOH) or sodium hydroxide (NaOH). Alkali modification leads to an increase in both surface area and the presence of basic functional groups compared to acid modification [71, 72]. The increase in basic functional groups on BC facilitates adsorption by enhancing ion exchange, electrostatic attraction, chemisorption, surface reactivity, pH adjustment, etc., which improves BC's ability to interact with and adsorb various contaminants. Also, alkali treatment results in BC with an elevated surface aromaticity ratio (H/C) and a higher N/C ratio, indicating an increased presence of nitrogen-containing groups on the modified BC surface that enhances its ability to sorb negatively charged ions and organic pollutants from wastewater [73]. Moreover, alkali modification was excellent in adsorbing pollutants such as Pb, Cd, Cu, and Mn(II) [74, 75].

Biological modification

Biological modification involves using microorganisms, enzymes, or biologically derived substances to alter the surface properties and functionality of BC. This method uses certain microorganisms to produce enzymes and metabolites that can interact with BC, introducing new functional groups or modifying existing ones to improve their adsorption capacity and other properties. A notable study by Tao et al. [76] explored the biological modification of BC using rumen microorganisms for the biological modification process. The corn stalks were first prepared through ensilage and then subjected to anaerobic fermentation using rumen inoculum obtained from cows fed on a mixed ration diet. The rumen fluid, rich in microorganisms, was used as a starter culture for anaerobic fermentation at 39 °C, simulating the residence time of corn stalk silage in the rumen. This biological treatment introduced specific functional groups that enhanced the BC's characteristics, resulting in a greater Cd(II) adsorption capacity, with more than 96% of Cd(II) being fixed within 4 hours. Biological processes often operate under mild conditions, reducing the need for harsh chemicals or extreme temperatures. However, there are also drawbacks to this method. The modification process can be time-consuming, as it often requires extended periods for microbial growth and biofilm formation. Additionally, the reproducibility of biologically modified BC can be challenging due to the variability in microbial activity and environmental conditions. Therefore, it is observed that this method is not reported much in heavy metal adsorption studies.

Among the various BC modification techniques, chemical activation stands out as the most effective method for enhancing BC's adsorption capacity. This approach offers superior control over surface chemistry and functionality by introducing a range of active functional groups that significantly improve BC's ability to adsorb contaminants. Although physical methods like steam or gas activation and advanced methods such as magnetic or biological modifications also provide valuable enhancements, chemical activation generally achieves the most pronounced improvements in adsorption efficiency. This makes it the preferred choice for producing high-performance BC adsorbents, particularly for applications requiring robust and reliable contaminant removal. However, there are many things that need to be studied for better chemical activation processes regarding following green chemistry principles by adopting less harsh chemicals and reducing the quantity of chemicals used.

Nanomaterial functionalization

Nanomaterials, such as metal oxide nanoparticles (Fe_3O_4, TiO_2, ZnO) and carbon-based nanomaterials, such as carbon nanotubes and graphene oxide (GO), have been incorporated into BC to improve their surface area, adsorption capacity, and magnetic recovery properties. ZnO impregnation enhances the adsorption properties of BCs by improving their microstructure, increasing the number of active sites, and facilitating the adsorption of both As(V) and Pb(II) through surface functional groups and ion exchange mechanisms [77]. The presence of ZnO contributed to microporosity, allowing better pollutant affinity, while Pb(II) adsorption occurred via binding to hydroxyl groups on ZnO, releasing protons into the solution, and As(V) adsorption was facilitated through ligand exchange, forming Zn-O-As complexes. GO-modified MBC also exhibits a well-defined graphitic structure that enhances π-π conjugation, while its advanced porosity, surpassing that of unmodified BC, promotes macromolecule transport, with oxygen-rich functional groups (-COOH, -CH(O)CH) from GO increasing surface binding capacity [78]. Another study showed that GO-enriched BC has improved metal adsorption capacity of 70.3 mol/g and 56.5 mol/g, with Cu and Zn, respectively, exhibiting low water solubility (<0.5%) and a slow-release profile [79]. This was likely facilitated by abundant O-functional groups that enabled Cu binding in a favorable spatial arrangement and Zn coordination via shared oxygen atoms, while its porous structure contributed to improved metal retention and slow release.

Electrochemical modifications

Electrochemical activation has emerged as an effective strategy to enhance BC's surface charge, pore structure, and functional groups. Studies have shown that electrochemically oxidized BC exhibits improved heavy metal adsorption due to the introduction of O-functional groups and increased redox reactivity. For example, electrochemical activation enhanced Pb adsorption by increasing O-functional groups, particularly hydroxyl groups, which facilitated Pb complexation through chemisorption [80]. Cathode activation promoted hydroxyl ion generation, leading to $Pb(OH)_2$ as the primary Pb species on BC, while anode activation enriched -OH and -COOH groups, boosting Pb removal from 27% (pristine BC) to 100% [80].

Hybridization into composites

Hybrid BC composites combining inorganic and organic modifiers have gained attention for their multifunctionality. For instance, BC-polyaniline composites have demonstrated enhanced adsorption for Cr(VI) due to the synergistic effect of BC's porosity and polyaniline's redox activity [81]. Similarly, BC-clay composites have been shown to improve stability and selectivity in wastewater treatment applications. For example, due to a well-developed mesoporous structure, hematite-modified BC-clay granular composites demonstrated a significantly higher specific surface area and improved adsorption capacity for Cr(VI) (61.72 m^2/g and 19.51 mg/g), compared to the unmodified BC, which had values of 18.43 m^2/g and 3.36 mg/g [82].

2.3. Updated review on the application of BC in specific heavy metal removal

Cadmium (Cd)

The chemical properties of Cd(II) ions, including their relatively small size and positive charge, make them prone to adsorption onto the surface of BC. The chemical functional groups found in BC, including carboxyl, amino, and hydroxyl groups, play a beneficial role in adsorbing Pb(II) and Cd(II) ions [83]. Also, Cd and Pb are divalent metal cations. These divalent metal cations tend to form strong hydration complexes in aqueous solutions, a process influenced by pH. So, pH influences the adsorption rate of Cd from the aqueous solution. At a pH level below 8, Cd shows little hydrolysis tendency, while at a pH level above 11, Cd(II) forms hydroxo-complexes. A study also showed a similar trend, where the adsorption of Pb and Cd gradually increased with the increase in pH [83]. Surface complexation is crucial as Cd ions form bonds with functional groups like carboxyl and hydroxyl on the BC surface. For example, Chen et al. [84] observed minimal shifts in the Fourier transform infrared (FTIR) spectra of carboxyl groups when comparing BC before and after Cd sorption, suggesting that Cd sorption primarily involved complexation with carboxyl groups. Fu et al. [85] observed that after Cd(II) adsorption onto wheat straw-derived MBC, numerous fine particles were detected on its surface and within its pore structure. The weight percentage of Cd was found to be 6.17%, as determined by Scanning electron microscopy with Energy Dispersive X-ray Spectroscopy (SEM-EDS) analysis, while no Cd species were detected before the adsorption process. This indicates that Cd(II) was removed by forming complexes with -COOH and -OH functional groups or by precipitation with OH^- and CO_3^{2-} on the surface of the adsorbent [85].

Chromium (Cr)

Chromium exists in various oxidation states, with the most common being trivalent chromium (Cr(III)) and hexavalent chromium (Cr(VI)). Both forms are encountered in environmental pollutants, with Cr(VI) being more toxic. Cr(III) is recognized as an essential micronutrient for humans, significantly less toxic than Cr(VI), yet its presence as a soluble species in natural waters can pose health risks due to potential oxidation to Cr(VI) in the environment [86]. Cr(VI) exhibits high solubility and mobility in water, posing significant environmental concerns due to its carcinogenic, mutagenic, and teratogenic effects on biological systems [86]. Two mechanisms have been suggested for the sorption of Cr(VI): (1) electrostatic attraction involving the negatively charged Cr(VI) species and positively charged BC and (2) the reduction of Cr(VI) to Cr(III) facilitated primarily by O-functional groups like carboxyl and hydroxyl groups, followed by the complexation of Cr(III) with functional groups on the BC [34, 87, 88]. The negatively charged chromate (CrO_4^{2-}) and dichromate ($Cr_2O_7^{2-}$) ions are attracted to positively charged sites on the BC surface. This attraction is due to the opposite charges of the ions and the BC surface, facilitating their binding. The reduction to Cr(III) is facilitated by O-functional groups. In this process, the O-functional groups on the BC surface donate electrons to the Cr(VI) ions, leading to their reduction to Cr(III) ions. The presence of electron-donating groups facilitates this reduction reaction. After being reduced to Cr(III), the ions bind with the functional groups on the BC surface through coordination bonds [89]. The complexation of Cr(III) with functional groups on the BC helps to immobilize the chromium ions and enhances their adsorption onto the BC surface. A study showed that amino-functionalized BCs were effective in Cr(VI) removal, which was mainly through Cr(VI) reduction to Cr(III) and then complexation by hydroxyl and carboxyl groups on BC, with a maximum of 76% removal [87]. Overall, the reduction and complexation processes are key in effectively removing Cr(VI) from aqueous solutions using BC-based adsorbents. The removal of Cr(VI) is pH-dependent, with better performance observed at lower pH [87, 90]. At lower pH, the predominant species of chromium (Cr(VI)) exists in the form of chromate ions (CrO_4^{2-}) and dichromate ions ($Cr_2O_7^{2-}$). Due to electrostatic interactions, these anionic species have a higher affinity for positively charged sites of the BC surface. BC typically carries a net positive charge at lower pH due to the protonation of surface functional groups such as –OH, –COOH, –CHO, –COC, etc. [91]. This positive charge facilitates the attraction and adsorption of negatively charged Cr(VI) ions onto the BC surface [91]. Furthermore, at lower pH, the protonation of functional groups on the BC surface may enhance the formation of surface complexes with Cr(VI) ions, promoting their adsorption.

Lead (Pb)

Lead ions (Pb^{2+}) possess a positive charge, allowing them to undergo electrostatic interactions with negatively charged functional BC groups, such as carboxyl, hydroxyl, and phenolic groups. These electrostatic attractions facilitate the adsorption of lead ions onto the BC surface. In a recent study on Pb removal from aqueous solutions, the adsorption process was predominantly governed by electrostatic interactions, wherein the transition of functional groups (-OH and -COOH) on the BC surface from positive to negative charge with increasing pH facilitated the attraction between Pb(II) ions and the BC surface [92]. Ion exchange is also responsible for the sorption of lead. In the ion exchange process, lead ions in the aqueous solution replace other ions bound to the surface functional groups of BC. The exchange occurs based on the relative affinity of lead ions for the BC surface compared to other ions present in the solution. This process allows lead ions to be immobilized on the BC surface, effectively removing them from the aqueous phase. Cation exchange with K^+ and Ca^{2+} for Pb sorption showed 69.9–85% of the total ion exchange adsorption capacity [93]. In another case study, the enhanced ion exchange capacity of $MgCl_2$-modified BC suggests successful impregnation of MgO onto the BC surface, where MgO undergoes hydration in water to form $Mg(OH)_2$ [94]. Lead ions can also form coordination complexes with functional groups on the BC surface through chemical bonding. Functional groups containing oxygen and nitrogen atoms, such as carboxyl and amino groups, can act as ligands and coordinate with the lead ions, enhancing their adsorption onto the BC surface.

Nickel (Ni)

In aqueous environments, nickel exists predominantly in two oxidation states: Ni(II) and Ni(III). In particular, soluble nickel compounds like nickel sulfate and nickel chloride are known to be carcinogenic and can cause respiratory issues, skin irritation, and adverse impacts on aquatic ecosystems. The chemical nature of nickel makes it amenable to adsorption by BC due to several factors. First, nickel ions (Ni^{2+}) possess a positive charge, allowing them to undergo electrostatic interactions with negatively charged functional BC groups, such as carboxyl, hydroxyl, and phenolic groups. These electrostatic attractions facilitate the adsorption of nickel ions onto the BC surface. Secondly, nickel ions can form coordination complexes with functional groups on the BC surface through chemical bonding [95]. Functional groups containing oxygen and nitrogen atoms, such as carboxyl and amino groups, can act as ligands and coordinate with the nickel ions, enhancing their adsorption onto the BC surface [95, 96].

The sorption of Ni also depends on pH, as the sorption increases with increasing pH (>5) [95, 97]. At lower pH, nickel ions are predominantly hydrated Ni^{2+} ions. As pH increases, the formation of hydroxide complexes such as $Ni(OH)^+$ and $Ni(OH)_2$ becomes more favorable. These hydrolyzed forms of nickel ions are more likely to adsorb onto the BC surface due to their larger size and increased reactivity than the hydrated Ni^{2+} ions. At lower pH, the surface of BC tends to be positively charged due to acidic functional groups like carboxyl and phenolic groups. However, as pH increases, the surface becomes negatively charged. This change in surface charge affects the electrostatic interactions between the positively charged nickel ions Ni^{2+} and the negatively charged BC surface, facilitating adsorption. Additionally, as pH increases, functional groups on the BC surface, such as carboxyl and hydroxyl groups, become more deprotonated and thus more negatively charged. This enhances the ability of these functional groups to complex with nickel ions through surface complexation reactions, leading to increased adsorption of nickel onto the BC surface. To further illustrate the effectiveness of BC in heavy metal removal, recent studies have been compiled in **Tables 2.2** and **2.3**.

Table 2.2 Recent studies of non-magnetic BC utilization for removing heavy metals

Biomass	**Process**	**Temp.**	**Surface area (m^2/g)**	**Pore volume (cm^3/g)**	**Heavy metals**	**Key results**	**Ref**
Wheat straw	Microwave pyrolysis	600 W	156.09	0.079	Pb(II), Cd(II), Cu(II)	Heavy metal adsorption capacity (31.25 and 139.44 mg/g)	[98]
Wheat Straw	Pyrolysis	550 °C	256.00	-	Co(II)	Co(II) immobilized in soil via -COOH and -OH, enhanced by Fe/Mn oxides.	[99]
Walnut shell	Pyrolysis	520 °C	280.00	0.950	Ni(II)	Optimal conditions: Ni(II) conc.: ≤ 150	[100]

						mg/L, pH: 6.5, Contact time: 120 min, Dose: 3000 mg/L, Temp: 288–303 K	
Lignin	Pyrolysis	450 °C	-	-	Cu(II), Mn(II), Zn(II)	Effectively adsorbs Cu(II) with a multilayer, heteroporous structure (Harkins-Jura model). Cu(II) removal is ~1.7x faster than Zn(II) and ~2.3x faster than Mn(II), with higher intraparticle adsorption.	[101]
Eichhornia crassipes plants	Pyrolysis	800 °C	296.42	0.103	Pb(II), Cu(II), Cd(II) and Zn(II)	High O-content (60.11%) and gave good removal Capacities for Pb(II), Cu(II), Cd(II), and Zn(II)were 0.57, 0.41, 0.44, and 0.48 mmol/g	[102]
Municipal sludge	Pyrolysis	400-1000 °C	30.96	-	Cd(II)	Maximum Cd(II) adsorption capacity at 700 °C: 120.24 mg/g.	[103]
Rice straw	Pyrolysis	300 °C			As(V)	Al modification increases As(V) adsorption	[104]
Potamogeton crispus	Pyrolysis	300-700 °C	7.15	0.022	Cr(VI)	BC produced at 300 °C showed the highest Cr(VI) adsorption	[105]

						(34.37 mg/g) at pH 2.0.	
Alkali lignin	Microwave pyrolysis	400 °C	1.15	0.009	Cu(II)	Cu(II) adsorption capacity: 405.55–492.75 mg/g, best fit by pseudo-second-order and Langmuir models. Co-precipitation and surface complexation (86.6%) are the main mechanisms.	[106]
Cornstalk	Pyrolysis and carbonization	600 °C	-	-	Hg(II)	Raw Carbon adsorbs Hg(II) (75.56 mg/g), with Inorganic Carbon (22.4%) and Organic Carbon (77.6%). IC has the highest capacity (92.63 mg/g) due to multiple mechanisms, while RC and OC rely on complexation.	[107]
Water hyacinth	Pyrolysis	500 °C	-	-	Cr	Removal efficiency at optimized conditions (time: 10 min, dose: 3g/70ml, pH 7.7) was 99%	[108]

Table 2.3 Recent studies of MBC utilization for removing heavy metals

Biomass	Magnetization	Process	Temp (°C)	Surface area (m^2/g)	Pore volume (cm^3/g)	Heavy metal	Key results	Ref
Peanut husk	Pre-pyrolysis treatment	Pyrolysis	600 °C	183.62	0.263	Cr(VI)	The removal rate by MBC was nine times better than regular BC	[19]
Brown algae	Post-pyrolysis treatment	Pyrolysis followed by hydrothermal treatment	700 °C	66.54	0.358	Cu(II)	High Cu(II) adsorption capacity (105.3 mg/g)	[109]
Hijikia	Pre-pyrolysis treatment	Pyrolysis	500 °C	63.33	-	Cd(II), Cu(II), Zn(II)	High Cu(II) adsorption as Cu(II) shows high affinity with the O-functional groups.	[20]
Corn waste straw	Post-pyrolysis treatment	Pyrolysis	600 °C	225.90	0.110	Cd(II)	More O-functional groups, fine-pore structure, and large surface area	[54]
			800 °C	313.90	0.220			
Palm kernel	Post-pyrolysis treatment	Pyrolysis	350 °C	90.19	-	Cd(II), Cr(III), Pb(II), Hg(II)	Rapid monolayer-physisorption	[110]
	Modified with MnO_2			89.39	-			
Waste pine needles	Post-pyrolysis treatment	Pyrolysis	500 °C	-	-	Pb(II), Cd(II)	Achieved up to 97% removal of Pb(II) and Cd(II) at basic pH, with maximum adsorption	[111]

Biomass	Magnetization	Process	Temp (°C)	Surface area (m^2/g)	Pore volume (cm^3/g)	Heavy metal	Key results	Ref
							capacities of 125 mg/g for Cd(II) and 142 mg/g for Pb(II)	
Tea waste	Post-pyrolysis treatment, microwaved with $(NH_4)_2 Fe(SO_4)_2$	Pyrolysis followed by microwave heating	800 °C	44.26	0.077	Ni(II), Co(II)	Adsorbed up to 147.84 mg/g of Ni(II) and 160.00 mg/g of Co(II)	[112]
Wheat straw	Co-pyrolysis	Pyrolysis	800 °C	44.31	0.065	Pb(II)	The high adsorption capacity of 190.42 mg/g	[25]
Water hyacinth	Pre-pyrolysis treatment	Pyrolysis	350 °C	163.60	-	Cu(II), Zn(II)	Feasible, spontaneous, and exothermic biosorption.	[113]
			450 °C	1038.48	-			
			600 °C	983.75	-			
Juglans regia nuts	Pre-pyrolysis treatment	Pyrolysis	450 °C	110.54	0.110	Cu(II), Ni(II)	The highest adsorption of Cu(II) (98.30%) and Ni(II) (98.10%) occurred at pH 6 and 50 mg/L, following Langmuir isotherm and pseudo-second-order kinetics, with endothermic behavior and activation	[114]

Biomass	Magnetization	Process	Temp (°C)	Surface area (m^2/g)	Pore volume (cm^3/g)	Heavy metal	Key results	Ref
							energies of 117.27 kJ/mol (Cu) and 100.24 kJ/mol (Ni)	

2.4. Adsorption mechanisms, reusability, modeling, and LCA studies

2.4.1. Adsorption mechanisms

Key mechanisms involved in metal adsorption by BC include ion exchange, surface complexation, precipitation, electrostatic attraction, physical adsorption, redox reactions, and chelation. **Figure 2.4** provides an overview of the adsorption mechanisms in BC used for contaminant removal.

Physical adsorption

Physisorption involves non-covalent interactions such as dispersion forces, dipole-dipole interactions, and hydrogen bonding [115]. These interactions are relatively weak, making physisorption generally reversible and favored under lower temperature conditions [116]. The process is largely driven by the surface area and pore structure of the adsorbent. A study showed that the increase in surface area (from 273.26 to 2372.51 m^2/g) and pore volume (from 0.24 to 1.20 cm^3/g) significantly increased the Hg adsorption capacity (209.65 mg/g) [117]. In another study, physisorption primarily governed the adsorption of ibuprofen onto waste coffee residue-based BC, with enhanced pore-filling effects playing a significant role in the adsorption of IBU onto the adsorbent [118]. In a study by Lee et al. [119], physisorption was identified as a primary mechanism for the sorption of Cd(II) and As(V) onto Miscanthus-derived BC, attributed to the adsorbent's porous structure, which includes micropores (191.6 m^2/g) and nanopores (57.2 m^2/g).

Chemical adsorption

Ion Exchange

Ion exchange is a mechanism where metal ions in the solution displace ions that are initially present on the surface of BC. This process is driven by the availability of exchangeable cations such as

H^+, Na^+, K^+, Ca^{2+}, and Mg^{2+} on the BC. Wu et al. [94] observed a substantial increase in the release of Mg^{2+} ions into the solution when using Mg-modified BC compared to unmodified BC. The adsorption capacities (Q_e) for Pb(II) and Cd(II) on the Mg-modified BC significantly increased from 3.93 and 1.78 mg/g to 192.36 and 105.46 mg/g, respectively. This impregnation of MgO onto the BC enhanced the ion exchange capacity. X-ray photoelectron spectroscopy (XPS) analysis revealed that the Mg1s peak area decreased by 88.5% for Pb(II) and 97% for Cd(II) following adsorption, indicating that the reduction in Mg1s peak intensity was primarily due to the release of Mg^{2+} ions during ion exchange. The leaching of Mg^{2+} from the modified BC further contributed to the observed decrease in Mg 1s intensity.

Electrostatic interaction

Electrostatic interaction occurs when metal ions are drawn to oppositely charged sites on the BC surface. This mechanism is especially effective for capturing cationic metals and is influenced by the BC's surface charge, which is determined by its pH and functional groups. For instance, in a study on Cr(T) adsorption, which involved dissolving $K_2Cr_2O_7$, it was found that Cr(T) is present as $HCrO^{4-}$, Cr_2O7^{2-}, CrO_4^{2-}, and H_2CrO_4, which are attracted by the positively charged BC surface [120]. Another study identified that the primary mechanism for removing Pb(II) and Cu(II) from aqueous solutions using modified BC as adsorbents is likely electrostatic interaction between the modified BC and the target ions [121]. Zeta potential (ZP) values, representing the surface charge of biomaterials dispersed in various pH solutions, describe the electrostatic potential of particles. ZP is a key indicator of colloidal stability; strongly positive or negative values suggest the potential for electrostatic attraction of oppositely charged ions [122]. For instance, Chen et al. [123] observed a significant decrease in zeta potential values from pH 2 to 4, stabilizing between pH 4 and 10. This indicates that the surface of pomelo peel derived from both magnetic and non-magnetic BC was negatively charged, suggesting that Pb(II) or Cu(II) ions were likely adsorbed onto the BC via electrostatic attraction. Similarly, Li et al. [121] observed that when the solution pH exceeded the point of zero charge, the adsorbent carried a negative charge. This negative charge facilitated the electrostatic binding of the adsorbent to Pb(II), Cu(II), and As(III).

Surface complexation

Complexation, which forms stable covalent bonds between metal ions (e.g., Cu(II), Fe(III)) and functional groups like carboxyl, hydroxyl, amino ($-NH_2$), and thiol (-SH) on the BC surface, significantly enhances the stability and retention of these metal ions [124]. Almanassra et al. [120], observed that after Cr(T) and Pb(II) adsorption, the FTIR analysis showed a shift in the C=O bond peak from 1632 cm^{-1} to 1645 cm^{-1}, with reduced intensity, indicating the involvement of C=O groups in adsorption. XPS analysis further revealed an increase in the binding energy of C–O groups, suggesting their interaction with Cr(T) through surface complexation. Chen et al. [123] observed that the reduction in intensity and shifting of peak positions in the FTIR analysis before and after adsorption indicated that the functional groups (-OH and -COOH groups) on the pomelo peel-derived BC formed metal chelate complexes with Pb(II) and Cu(II) ions. Another study found that iron ions in the MBC serve as a bridge, linking the BC to As(III) and leading to the formation of new complex compounds [125].

Precipitation

Precipitation is crucial in BC's heavy metal adsorption, involving converting dissolved metal ions into insoluble solid phases on the BC surface. This mechanism is affected by the chemical composition of the BC, including its mineral content and functional groups. High mineral content in BC, particularly from feedstocks rich in inorganic materials, creates a conducive environment for precipitation reactions. These minerals can interact with metal ions to form insoluble hydroxides, carbonates, or phosphates, which are then deposited on the BC surface. A study showed that coconut shell BC released CO_3^{2-}, PO_4^{3-}, and OH^- anions which precipitated Pb(II) and Cd(II) into $PbCO_3$, $Pb_3(CO_3)_2(OH)_2$, $2PbCO_3 \cdot Pb(OH)_2$, $Pb(H_2PO_4)_2$, and $CdCO_3$, $Cd_3(PO_4)_2$, $Cd(OH)_2$, and Cd_3SiO_5 respectively [94]. Surface functional groups on BC, like carboxyl (-COOH) and hydroxyl (-OH), play a key role in precipitation by binding metal ions to form stable metal-organic complexes that facilitate further precipitation. Li et al. [121] found that the precipitation of Pb(II) and Cu(II) with –OH groups on the adsorbent enhanced the adsorption of metal ions. Post-adsorption X-ray diffraction (XRD) patterns revealed peaks at 24.63° and 27.13°, likely corresponding to $Pb_3(CO_3)_2(OH)_2$ for Pb, and a distinct structural change at 28.98°, associated with the reflection peak of $Cu(OH)_2$ for Cu. In a similar study, As(V) was found to precipitate on BC-loaded Ce^{3+} enriched ultra-fine cerium oxide nanoparticles, forming $CeAsO_4$ [126]. This was confirmed by XRD analysis, which revealed the after-adsorption peaks at 26.4°, 28.2°, 30.1°, and 40.3°.

Other removal mechanisms

Redox reactions, aided by BC's surface functional groups and redox-active components, play a significant role in reducing metal ions. For instance, the interaction between the O-functional groups on BC and Cr(VI) is crucial, where these groups donate electrons to convert Cr(VI) to Cr(III). Subsequently, Cr(III) can be exchanged with K^+ ions in the BC and released into the solution [127]. π-π interactions involve the coordination of metal ions with the aromatic rings of BC. Liu et al. [128] found that BC made from banana stems and leaves efficiently adsorbs Pb and Cd. FTIR analysis revealed a decrease in -CH, C=C, and C=O groups after adsorption, indicating that these metal ions interacted with the π-electrons during adsorption. Hydrogen bonding occurs when metal ions bond with hydroxyl and carboxyl groups on BC, which improves adsorption. Research has demonstrated that As(V) is adsorbed onto BC through hydrogen bonding with the -COOH groups on the BC surface [129].

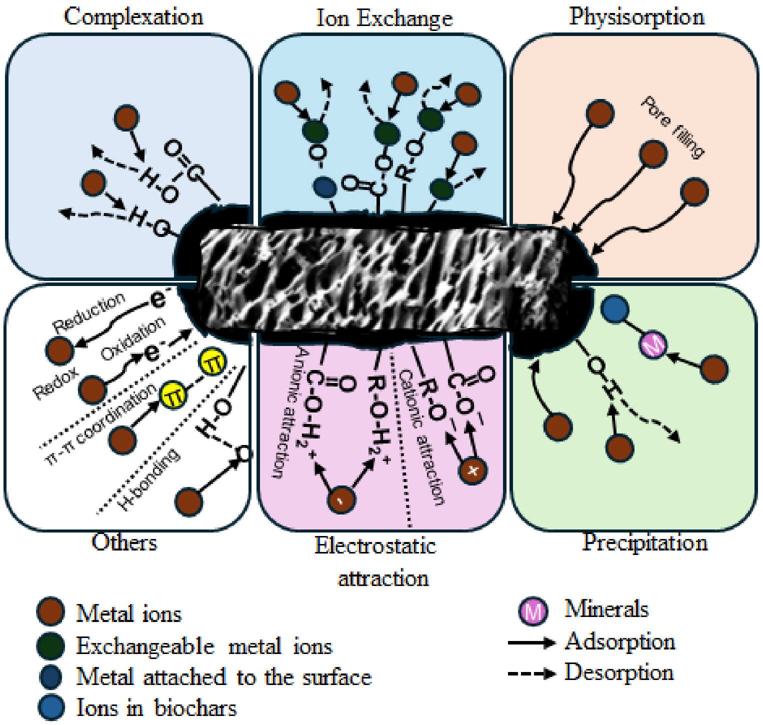

Figure 2.4 Adsorption mechanisms in BC for heavy metal removal [130]

2.4.2. Regeneration and reusability

Regeneration and reuse of BC and BC-based adsorbents are designed to restore the adsorption capacity of BC after it becomes saturated with contaminants, thereby extending its lifespan and minimizing the need for replacement. Moreover, effective regeneration prevents the re-release of adsorbed pollutants into the environment, ensuring that the treatment process remains both efficient and sustainable. Several regeneration techniques have been explored to restore BC’s adsorption properties, each with varying degrees of effectiveness, as shown in **Table 2.4**.

Thermal regeneration involves heating BC to high temperatures in the absence of oxygen to desorb the adsorbed contaminants. This process effectively restores the BC's adsorption capacity by removing organic pollutants and volatile compounds, allowing the BC to be reused in subsequent adsorption cycles. Shan et al. [131] demonstrated that the thermal regeneration of BC at 80 °C, used as a catalyst for methyl orange degradation, maintained good stability, with the degradation efficiency slightly decreasing from 97.48% to 96.10% after five cycles. Similarly, Guo et al. [132] achieved 79.54% methylene blue (MB) removal after 3 cycles by regenerating BC by heating the MB-loaded BC at 449.85 °C in an oxygen-limited environment using a muffle furnace. However, repeated thermal regeneration can sometimes lead to structural changes and loss of mass in the BC due to continuous heating and washing [133].

Chemical regeneration is another commonly used method for restoring adsorbents, relying on the concentration of the adsorbate and its interaction with the adsorbent. It uses solvents and reagents to desorb contaminants, making it ideal for organic adsorbents with low thermal stability and boiling points [134]. Common chemicals include acids, bases, and oxidizing agents. For instance, some studies show that acid treatment using different concentrations of HNO3, H2SO4, and HCl was used to regenerate BC used for inorganic (heavy metal) and organic pollutant (dye, antibiotic) removal, achieving a significant restoration of adsorption capacity [135-137]. Bases are also successfully used for regeneration purposes. For instance, Ahmed et al. [138] regenerated BC after Pd(II) adsorption using NaOH, achieving 91% efficiency and successfully reusing it for five cycles. In addition to conventional regeneration methods, Kandel et al. [139] explored cold plasma (CP) treatment for BC regeneration. After drying, the used adsorbent was treated in DI water with radical species generated by CP (10 mA, 2.2 W) for 1 hour, achieving 70% efficiency after five cycles. Notably, this technique consumes 6.4 times less power than carbonizing new adsorbent, highlighting its energy efficiency. While BC regeneration is critical for sustainable application, repeated adsorption-desorption cycles often lead to structural degradation and loss of active adsorption sites of the adsorbents. Thermochemical and chemical regeneration methods have been explored, but these processes can alter surface chemistry and reduce adsorption efficiency.

Moreover, chemical regeneration using acids or alkalis may introduce additional environmental concerns. Optimizing regeneration conditions, such as mild acid/base washing or electrochemical desorption, can help maintain BC integrity while minimizing waste generation.

Table 2.4 Summary of different proposed methods for the regeneration of BC

Material	Pollutant	Regeneration method	Regeneration process	Reusability	Ref
Carbonized rice husk (CRH)	Methylene blue (MB)	Cold plasma (CP) treatment	CRH added to 100 mL DI water and exposed to air with radicals generated by CP at 10 mA and 2.2 W for 1 h.	70%, 5 cycles	[139]
Macroalgae-based BC	MB	Chemical	HNO_3	67%, 3 cycles	[135]
La-modified Platanus ball fiber BC	Phosphate	Thermal	washed with 0.5 mol/L NaOH solution at 50 °C	3 cycles	[140]
Orange peel BC	Cu(II), Ni(II)	Chemical	0.8 M H_2SO_4	68% for Cu; 65% for Ni, 5 cycles	[136]
Ag/TiO_2/BC composite catalyst	Methyl orange	Thermal	filtered, rinsed by DI water, and dried at 80 °C	97.48%, 5 cycles	[131]
Sludge-based MBC	MB	Chemical	0.05 mol/L HCl for 9 h	61.73%, 5 cycles	[137]
Rice-straw BC	Pb(II)	Chemical	50 mL of 0.5 mol/L NaOH	91%, 5 cycles	[138]
Chitosan magnetite nanosorbents	Glyphosate herbicide	Chemical	washed three times with ethanol (20 mL) and twice	83.3%, 4 cycles	[141]

Material	Pollutant	Regeneration method	Regeneration process	Reusability	Ref
			with distilled water (20 mL), and dried		
Activated carbon	PFAS	Thermal	Drying at 105 °C; Pyrolysis at up to 800 °C; Oxidizing gas treatment	99%	[133]
Waste coffee residue BC	Ibuprofen	Thermal	EtOH, 0.1 M EDTA, or 0.1 M NaOH (1:5, w/v) for 24 h, washed with DI water and oven-dried at 80 °C for 12 h.	15–24% NaOH, 41–47% EtOH, 10–18% EDTA, 5 cycles.	[118]

2.4.3. Machine learning and artificial intelligence applications in biochar for wastewater treatment

Recently, Machine Learning (ML) and Artificial Intelligence (AI) have shown significant potential in designing BC-derived materials and optimizing their environmental applications. ML's capacity to analyze complex variable interactions makes it particularly effective in developing novel adsorption processes. The optimization and analysis capabilities of ML models streamline the development of adsorption models, which initially required an extensive amount of experimental work due to the numerous parameters involved, such as temperature, heating rate, adsorbent surface area, dosage, initial concentration, particle size, contact time, and pH [142-144]. Specifically, ML has been used to connect BC utilization with computational techniques such as Decision Trees (DT), Artificial Neural Networks (ANN), and Random Forests (RF) [145]. For instance, DT models in ML are employed to optimize BC-based wastewater treatment processes by modeling the complex interactions between BC properties and adsorption efficiency [146]. ANN algorithms, which simulate the human brain's learning and memorization processes using programming languages, are also being applied in this field [142]. **Figure 2.5** illustrates the machine-learning workflow for BC synthesis and heavy metal adsorption.

Recent ML developments in BC synthesis include predicting BC yield and properties, optimizing synthesis conditions, and evaluating economic costs [147]. Pyrolysis conditions, particularly temperature and biomass feedstock properties (e.g., ash content), were identified by ML as one of the dominant factors influencing BC yield. Zhu et al. [148] utilized RF models to forecast BC yield and carbon content, determining that pyrolysis conditions contributed more significantly to yield prediction (65%) than feedstock properties (53%). Leng et al. [149] applied RF and gradient boosting regression (GBR) to predict BC yield, nitrogen content, and specific surface area, confirming reaction temperature and residence time as the most influential factors. Hai et al. [150] compared multiple supervised learning models, including multiple linear regression (MLR), DT, RF, Support Vector Machine (SVM), and K-nearest neighbors (KNN), for predicting BC yield and surface area. RF exhibited superior predictive performance, with pyrolysis temperature identified as the most critical factor. Potnuri et al. [151] employed polynomial regression-based ML models to predict sawdust-derived BC production from microwave-assisted catalytic pyrolysis, achieving R-values higher than 0.93. Additionally, Narde and Remya [152] used linear, interactive, and quadratic regression models to predict microwave-assisted pyrolysis BC yield, with the quadratic regression model demonstrating the best performance ($R^2 = 0.894$), where key influencing factors included volatile matter content, biomass ash content, and reaction temperature. Li et al. [153] studied multilayer perceptron neural networks (MLP-NN) and adaptive neuro-fuzzy inference systems (ANFIS) to predict BC yield and composition. MLP-NN achieved high accuracy ($R^2 = 0.964$), with pyrolysis temperature, ash content, and nitrogen content being the most significant determinants. Kingsley and Tien-Chien [142] reported that methods like Extreme Gradient Boosting (XGB) and RF have demonstrated high precision in predicting BC yield and carbon content, with XGB achieving an R^2 of 0.84, and have provided insights into the complex interactions among parameters such as ash content and pyrolysis conditions.

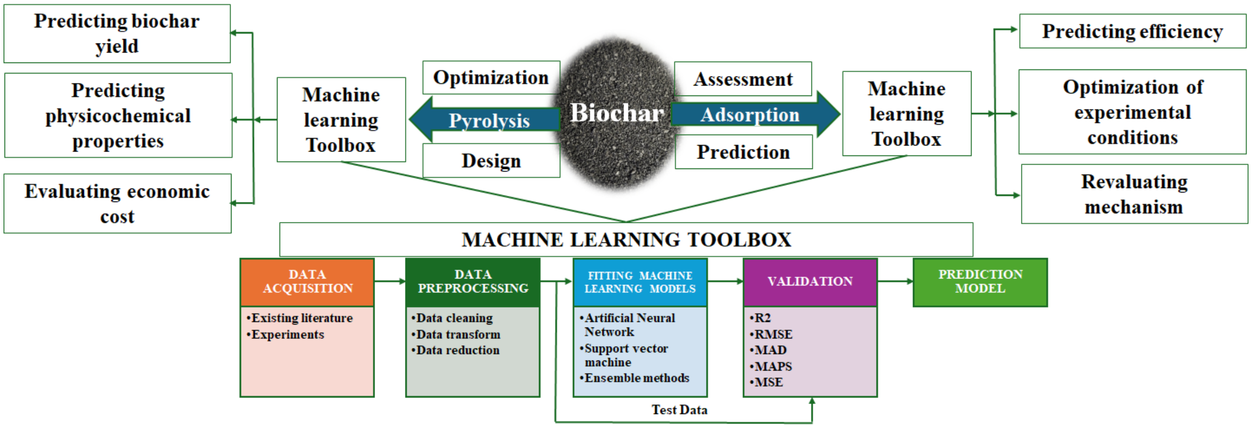

Figure 2.5 Machine learning research frontiers involved in BC synthesis and heavy metal adsorption studies [147, 154]

ML techniques have demonstrated high accuracy in predicting BC properties, including elemental composition (C, H, N, O), fixed carbon (FC), volatile matter (VM), ash content, specific surface area (SSA), and pore volume. Leng et al. [149] utilized RF and GBR models to optimize BC yield, nitrogen content, and SSA based on biomass characteristics and pyrolysis conditions, achieving an R^2 of > 0.97. Similarly, Li et al. [153] employed MLP-NN and ANFIS models to predict BC composition with R^2 values ranging from 0.785 to 0.940. Shahbeik et al. [155] successfully applied RF to predict the H/C, H/N, and O/C ratios of sludge-derived BC with an R^2 exceeding 0.9, further confirming ML's predictive potential. Ang et al. [156] used rough set machine learning (RSML) to model these properties, identifying pyrolysis temperature, time, and biomass composition (FC, VM, Ash) as dominant influencing factors. Li et al. [157] demonstrated that RF and GBR could effectively predict SSA and total pore volume with R^2 in the range of 0.89 – 0.94, further validating the capability of ML in BC surface property prediction.

ML techniques can also effectively model complex heavy metal adsorption on BC, surpassing traditional isotherms by capturing nonlinear interactions and enhancing predictive accuracy. Several studies validate their effectiveness in adsorption modeling. Wong et al. [158] investigated using rambutan peel BC for Cu(II) removal from water, evaluating operational parameters using AI models, including ANN, Adaptive ANFIS, and MLR. The ANFIS model achieved the highest accuracy at 90.24%, followed by ANN at 88.27% and MLR at 59.14%. Similarly, Li et al. [159] employed an SVM model for Pb(II) adsorption on EDTA-modified BC, while Nath et al. [160] used iron oxide permeated mesoporous rice-husk nano-BC for arsenic removal, achieving 96% efficiency through ANN and Response Surface Methodology (RSM). El Hanandeh et al. [143]

developed six AI models with various ANN architectures to analyze the adsorption of Pb, Cu, and Ni ions from single and multi-component aqueous solutions using date seed-derived BC. All models demonstrated high efficiency, with correlation coefficients exceeding 0.99. Chakraborty and Das [161] utilized ANN to predict Cr(VI) adsorption on nanocomposite sawdust BC, establishing an effective adsorption mechanism and equation. Zhao et al. [146] introduced a new approach using a Kernel Extreme Learning Machine (a subset of SVM) and Kriging models to predict adsorption efficiencies for six heavy metal ions. Their models accurately identified temperature, pH, and carbon content as key influencing parameters, achieving R^2 values above 0.9.

In addition to adsorption conditions, the surface properties of BC also play a crucial role. Yan et al. [162] demonstrated that surface O-functional groups significantly enhance As(V) and As(III) removal, whereas high non-polar carbon content negatively affects adsorption performance. Zhu et al. [163] further highlighted that polyaromatic and non-polar carbon functionalities improve Cr(VI) adsorption on Fe-modified BC. Da et al. [164] predicted uranium adsorption behavior using logistic regression (LR), SVM, RF, and MLP-NN models, concluding that surface area, rather than chemical composition, is the dominant factor. Similarly, Zhu et al. [165] found that cation exchange capacity and pH predominantly influence heavy metal adsorption behavior. Recent advancements in visualization techniques have enabled in-depth analysis of adsorption behavior. Zhang et al. [166] developed a three-dimensional in-situ visualization approach using X-ray micro-computed tomography (CT) to characterize Pb adsorption on BC. The integration of K-means clustering enabled segmentation of the BC structure, providing detailed adsorption distribution profiles.

Deep learning models offer significant advantages for multicomponent adsorption systems because they can handle dimensionality reduction and complex variable analysis. Talebkeikhah et al. [167] employed a Multi-Layer Perceptron (MLP) for Pb(II) adsorption and explored performance improvements by integrating MLP with other algorithms. Singha et al. [168] demonstrated that deep learning models outperform traditional machine learning models in predicting groundwater pollution indices, with R^2 values ranging from 0.98 to 0.99 compared to 0.88 to 0.95 for machine learning models. Talebkeikhah et al. [167] also examined various models, including SVM, RF, ANFIS, MLP, Radial Basis Function Network (RBFN), and Decision Trees.

They found that SVM performed best with an R^2 of 0.9975, and coupling ANFIS and MLP with optimization algorithms like the Grasshopper Optimization Algorithm (GOA) enhanced model efficiency. Ke et al. [169] highlighted the effectiveness of combining Fuzzy C-Means Clustering with Backpropagation Neural Networks (BPNN) to predict heavy metal adsorption, achieving an R^2 of 0.987 compared to 0.977 with BPNN alone. Additionally, Ke et al. [170] developed 20 coupled models using SVM, RF, ANN, M5Tree, and Gaussian Process (GP), finding that GP-coupled models performed poorly relative to uncoupled models. They suggested that dataset characteristics might influence model performance. They proposed further exploration of clustering algorithms for coupling multiple deep learning and machine learning models to enhance the evaluation of adsorption capacities using modified BC.

Advancing ML applications require high-quality datasets, better generalizability, and integration with mechanistic models like thermodynamics and kinetics for enhanced predictive performance [171]. Small-dataset algorithms, data augmentation techniques (e.g., GAN, KDE), and feature selection help overcome data limitations [172]. Preprocessing techniques like normalization improve data comparability, and open data-sharing platforms like GitHub foster ML advancements [157]. Experimental validation, pilot-scale data, and hybrid models integrating ML with statistical methods drive real-world applications [171, 173]. Chen et al. [174] improved predictive accuracy by training RF, GBR, and SVM models on experimental and literature datasets, increasing R^2 from 0.95 to 0.97–0.98. Traditional ML techniques (MLR, SVM, RF, ANN) are widely used, but emerging methods like Reinforcement Learning (RL) could enhance interpretability and adaptive optimization [147]. Despite challenges like computational demands and overfitting risks, integrating ML and AI deepens our understanding of BC's effectiveness, making it a promising area for future research.

2.4.4. Life Cycle Assessment (LCA) and Techno-economic assessment (TEA) studies

Life Cycle Assessment (LCA) is a critical tool for analyzing the potential environmental impacts associated with products, processes, or activities. By evaluating the entire life cycle from raw material acquisition, production, and use to disposal or recycling, LCA provides comprehensive insights into the ecological effects of a product or system [175, 176]. Conducting a proper LCA involves gathering detailed data on energy, materials, and environmental outputs, including soil, water, air, and waste impacts. This data is analyzed with specific methodologies to assess environmental impacts and identify areas for improvement across the life cycle stages, from raw material acquisition to end-of-life. LCA is extensively used in industry, policymaking, and research to support sustainable decision-making, optimize product designs, and develop environmental policies, aiming to reduce the overall environmental burden [177]. The ISO 14,040 and 14,044 standards guide LCA through four major phases: defining the aim and scope, inventory analysis, impact assessment, and interpretation or improvement analysis. Common LCA software includes SimaPro, GaBi, and Open LCA. SimaPro is particularly valued for its comprehensive inventory data and effective graphical interface, especially in evaluating waste-to-energy processes like BC production [178].

Several studies have investigated BC production's life-cycle assessment (LCA), emphasizing how feedstock type and biomass conversion temperatures significantly affect the environmental impacts. LCA has been extensively employed to assess these impacts, with most studies focusing on the potential reduction of greenhouse gas (GHG) emissions, a primary advantage of BC. However, there are concerns regarding the environmental implications of dedicating agricultural land specifically for BC production [178, 179]. Additionally, comparisons between BC, activated carbon, and metal-based catalysts have been explored in recent research [180, 181]. Gallego-Ramírez et al. [175] found that the energy source and the gasification process predominantly influence the environmental impacts of producing raw and Fe-modified BCs via gasification. Moreover, they highlighted that the additional steps and reagents required for Fe modification further contribute to these impacts, as evaluated using the SimaPro software.

Techno-economic assessment (TEA) is a framework used to evaluate the technical and economic performance of processes, products, or services by integrating process modeling, engineering design, and economic evaluation. TEA assesses the economic significance of new technologies by examining costs, profits, risks, uncertainties, and timeframes [178]. In the context of bioenergy, factors like facility location, biomass supply insecurity, and the supply chain network significantly impact economic viability [182]. Relocating facilities can be an effective strategy to mitigate biomass supply risks. The supply chain is categorized into three types: centralized (Type I), decentralized (Type II), and hybrid (Type III). Type I involves large-scale biomass transformation facilities with wide draw radii, while Type II features smaller facilities with narrower draw radii. Type III combines a centralized transformation service with multiple preprocessing facilities to densify biomass before transport. Research suggests that Type II supply chains may have lower end-product costs than Type I despite higher logistics and investment expenses. While reducing handling and transportation costs, Type III requires higher total investments due to a lack of scale economies at preprocessing sites. All three types contribute to higher bioenergy production costs, primarily due to logistics or infrastructure expenses [183, 184].

During this review, we found limited articles on the LCA and TEA of BC-based wastewater systems and their improvements. The main challenge is the scarcity of comprehensive and reliable technical data for systematic evaluation. While LCA and TEA aim to identify effective methodologies for swift commercialization, significant gaps in the literature hinder the advancement of innovative waste-to-product conversion methods. Despite existing knowledge on biomass conversion, by-products, feed composition, and process parameters, research remains limited.

2.5. Innovative trends, emerging challenges, and future research directions

2.5.1. Advancements, novel perspectives in BC development

One promising avenue is the development of multi-functionalized BC designed for selective heavy metal adsorption. Traditional BC exhibits a broad affinity for various contaminants, but surface modifications, such as N-doping, metal impregnation, and hierarchical pore structuring, can enhance selectivity toward specific metal ions [185]. A recent study proposes that tuning the electron density of functional groups via heteroatom doping (e.g., N, S, P) can significantly improve affinity toward target pollutants, potentially leading to more efficient and cost-effective remediation systems [186].

Another novel perspective gaining traction is the functionalization of BC with microbial consortia for bioaugmentation strategies. Engineered BC with microbial inoculants (e.g., metal-resistant bacteria, fungi, or biofilms) could facilitate in-situ bioremediation while enhancing adsorption efficiency [187, 188]. BC’s porous architecture provides a stable microhabitat, promoting microbial colonization and enzymatic activity for long-term heavy metal sequestration in contaminated environments.

2.5.2. Challenges in industrializing BC-based material for heavy metal remediation

Challenges regarding the existing results' variability

There is a considerable number of variations in existing results, which makes the standardization of BC-based adsorbents difficult. Specifically, although many studies report high adsorption efficiencies, there are inconsistencies in the reported removal capacities of BC. BC's varying effectiveness in heavy metal adsorption across studies can originate from several factors, including feedstock type, pyrolysis conditions, and environmental parameters. The choice of feedstock significantly influences the BC's physicochemical properties, thereby affecting its adsorption capacity. For instance, BC derived from spent mushroom substrates exhibited Pb^{2+} adsorption capacity ranging from 1.6 to 10 times higher than other modified BC [189]. Environmental factors such as pH, temperature, and the presence of competing ions (e.g., Ca^{2+}, Mg^{2+}) will also influence the adsorption efficiency of heavy metals. Studies have demonstrated that adsorption capacity generally increases with the increase in pH due to reduced competition with H+ ions. For example, the adsorption capacity of Pb^{2+} onto BC increased with rising pH levels, stabilizing beyond pH 3 [189]. Similarly, studies have shown that as the pH increases from 3 to 6, the adsorption capacity for Cu^{2+} ions improves [190]. This enhancement is attributed to reduced proton competition and decreased electrostatic repulsion between the cations and the BC surface. However, the optimal pH for adsorption varies depending on the specific metal species and BC characteristics. Additionally, the presence of competing ions can also impact adsorption efficiency. High concentrations of metal ions such as potassium, calcium, sodium, and magnesium on the BC surface can compete with other heavy metal ions, thereby reducing the effectiveness of ion exchange and hindering the adsorption process [191]. Moreover, the nature of the heavy metal itself also plays a role. Factors such as ionic charge, ionic radius, hydration energy, and chemical speciation influence how strongly a metal binds to BC-based adsorbents. For example, Pb^{2+} and Cd^{2+} are both divalent cations and often exhibit higher adsorption efficiencies compared to other metal ions due to their strong interactions with O-functional groups functional groups [192]. In contrast, metals like As and Cr exhibit variable adsorption behavior due to their different oxidation states, which influence their interaction with BC. For instance, Wang et al. [193] reported that the adsorption capacities of pine wood-derived magnetic BC for As and Cr are influenced by their chemical forms, with variations in oxidation states resulting in different interactions with the BC surfaces Understanding these variations and standardizing adsorption experimental conditions will be helpful in eliminating inconsistency in comparative studies of different adsorbents.

Challenges regarding the lack of real-life and long-term studies

The influence of actual wastewater conditions, such as the presence of competing ions (e.g., Na^+, Ca^{2+}, Cl^-), remains underexplored in many laboratory-scale studies. A major challenge is the lack of standardized testing protocols for BC performance evaluation. Most of the previous studies use synthetic wastewater with single-metal solutions, which do not fully represent real-world wastewater complexities. Future research should emphasize multi-metal adsorption experiments and field-scale validation to establish reliable performance metrics. Another limitation is the degradation of BC effectiveness over repeated adsorption cycles. While some modification strategies, such as functionalization with iron oxides, enhance reusability, BC often suffers from structural deterioration and reduced adsorption capacity after multiple regeneration cycles. Also, the regeneration of BC is often limited by the potential to cause secondary pollution and high chemical or energy demands. Additionally, improper disposal or incomplete regeneration may lead to environmental risks, such as heavy metal leaching or toxic byproduct formation. Investigating sustainable regeneration methods remains a critical research gap.

Over time, BC undergoes aging processes, including oxidation, microbial colonization, and surface functionalization changes, which can alter its adsorption performance [194, 195]. Aged BC may exhibit reduced metal adsorption due to pore blockage and loss of active sites. Additionally, interactions with dissolved organic matter can modify BC surface charge, influencing its binding affinity toward metal ions. It can enhance its durability by understanding BC aging mechanisms through long-term studies and incorporating stabilizing agents such as clay minerals or bio-based coatings.

Future perspectives

To rationalize the selection of biomass feedstock and pyrolysis conditions, future studies should explore the use of ML and AI tools to establish standardized biomass selection mechanisms and production operating parameters to optimize BC properties for targeted heavy metal removal. For example, biomass with high lignin and ash content will produce BC with superior metal adsorption properties due to increased porosity and active site availability. In contrast, high-temperature pyrolysis (>700 °C) will enhance graphitic structures, improving stability and adsorption kinetics. ML and AI tools may play a crucial role in comparing and screening candidate biomass and in precisely predicting the best feedstock-pyrolysis-modification combinations for specific adsorption applications, reducing the need for extensive experimental trials.

Moreover, future research should also focus on understanding and developing better modification strategies to improve selectivity for specific metal species. Surface functionalization with metal oxides (e.g., Fe, Mn, Al) and heteroatom doping (e.g., N, S, P) will improve the selectivity and binding affinity of BC towards specific heavy metals by enhancing surface charge and functional group availability. Additionally, integrating BC with novel carbon nanomaterials, such as graphene or carbon dots, could enhance adsorption kinetics and reusability [196, 197]. The development of multifunctional BC composites may offer tailored adsorption mechanisms for different contaminants in complex wastewater systems.

In addition, most BC adsorption studies do not fully represent real wastewater conditions where multiple metal ions coexist. The presence of competing cations (e.g., Na^+, Ca^{2+}, Mg^{2+}) and anions (e.g., Cl^-, SO_4^{2-}) in real-life water bodies might reduce BC's adsorption efficiency due to site competition, requiring modified BC with enhanced ion-exchange capacity or selective functionalization. Future studies should emphasize multi-metal adsorption experiments and real wastewater validation to ensure the practical applicability of BC in large-scale water treatment facilities.

Furthermore, the large-scale deployment of BC in wastewater treatment systems must align with circular economy principles, ensuring minimal waste generation and resource recovery. Potential applications beyond wastewater treatment, such as nutrient recovery and carbon sequestration, should be further explored. Metal-laden BC can be repurposed as a soil amendment for controlled-release fertilization or as a precursor for catalyst synthesis, enhancing resource recovery. More comprehensive LCA studies should be conducted to evaluate the environmental footprint of BC production, modification, and disposal, ensuring its feasibility as a sustainable remediation material.

2.6. Conclusion

BC and its composites hold great promise for remediating heavy metal pollutants in wastewater. However, several challenges must be addressed to unlock their full potential. One pressing need is the optimization of BC synthesis. Standardizing pyrolysis parameters like temperature, residence time, and feedstock characteristics will help achieve BC with consistent and enhanced adsorption properties. Moreover, exploring unconventional biomass sources and advanced activation techniques could yield materials with superior performance for specific heavy metals. Magnetic BC represents a significant advancement, offering easier recovery and enhanced adsorption efficiency. However, more research is required to assess the environmental impacts and stability of magnetic components during long-term use. Additionally, developing sustainable and efficient regeneration methods for BC is essential for extending its usability and reducing costs. Understanding the fundamental adsorption mechanisms of heavy metal removal remains a critical area for further study. Advanced techniques such as spectroscopic analysis and molecular simulations can provide valuable insights into the interaction dynamics between BC surfaces and heavy metal ions. Integrating ML and AI into BC research offers exciting opportunities to accelerate progress. These technologies can optimize process parameters, predict adsorption performance, and streamline modification strategies, saving time and resources in experimental studies. Finally, LCA and TEA tools can be very helpful in understanding the long-term feasibility and environmental sustainability of BC-based solutions. Therefore, future research should consider incorporating these analysis tools.

References

[1] A. G. Adeniyi, K. O. Iwuozor, E. C. Emenike, O. J. Ajala, S. Ogunniyi, and K. B. Muritala, "Thermochemical co-conversion of biomass-plastic waste to biochar: A review," *Green Chemical Engineering,* vol. 5, no. 1, pp. 31-49, 2024.

[2] A. Ajien, J. Idris, N. Md Sofwan, R. Husen, and H. Seli, "Coconut shell and husk biochar: A review of production and activation technology, economic, financial aspect and application," *Waste Management & Research,* vol. 41, no. 1, pp. 37-51, 2023.

[3] B. Wang, M. Ran, G. Fang, T. Wu, and Y. Ni, "Biochars from Lignin-rich Residue of Furfural Manufacturing Process for Heavy Metal Ions Remediation," *Materials,* vol. 13, no. 5, p. 1037, 2020. [Online]. Available: https://www.mdpi.com/1996-1944/13/5/1037.

[4] J. O. Ighalo *et al.*, "Biochar from coconut residues: An overview of production, properties, and applications," *Industrial Crops and Products,* vol. 204, p. 117300, 2023/11/15/ 2023, doi: https://doi.org/10.1016/j.indcrop.2023.117300.

[5] A. B. Duwiejuah, A. H. Abubakari, A. K. Quainoo, and Y. Amadu, "Review of biochar properties and remediation of metal pollution of water and soil," *Journal of Health and Pollution,* vol. 10, no. 27, p. 200902, 2020.

[6] D. Vaičiukynienė, R. Alaburdaitė, D. Nizevičienė, and G. Tamošaitis, "Sorption properties of Pb2+ ions from water by alkali activated slag/biochar composites," *Biomass Conversion and Biorefinery,* 2024/02/20 2024, doi: 10.1007/s13399-024-05434-3.

[7] A. Herath, C. A. Layne, F. Perez, E. I. B. Hassan, C. U. Pittman, and T. E. Mlsna, "KOH-activated high surface area Douglas Fir biochar for adsorbing aqueous Cr(VI), Pb(II) and Cd(II)," *Chemosphere,* vol. 269, p. 128409, 2021/04/01/ 2021, doi: https://doi.org/10.1016/j.chemosphere.2020.128409.

[8] M. J. Bardi, J. M. Mutunga, H. Ndiritu, and K. Koch, "Effect of pyrolysis temperature on the physiochemical properties of biochar and its potential use in anaerobic digestion: A critical review," *Environmental Technology & Innovation,* vol. 32, p. 103349, 2023/11/01/ 2023, doi: https://doi.org/10.1016/j.eti.2023.103349.

[9] L. Leng *et al.*, "Nitrogen containing functional groups of biochar: an overview," *Bioresource technology,* vol. 298, p. 122286, 2020.

[10] B. Ma, J. Zhu, B. Sun, C. Chen, and D. Sun, "Influence of pyrolysis temperature on characteristics and Cr(VI) adsorption performance of carbonaceous nanofibers derived from bacterial cellulose," *Chemosphere,* vol. 291, p. 132976, 2022/03/01/ 2022, doi: https://doi.org/10.1016/j.chemosphere.2021.132976.

[11] Z. Wang, J. Xu, D. Yellezuome, and R. Liu, "Effects of cotton straw-derived biochar under different pyrolysis conditions on Pb (II) adsorption properties in aqueous solutions," *Journal of Analytical and Applied Pyrolysis,* vol. 157, p. 105214, 2021/08/01/ 2021, doi: https://doi.org/10.1016/j.jaap.2021.105214.

[12] L. Leng *et al.*, "An overview of sulfur-functional groups in biochar from pyrolysis of biomass," *Journal of Environmental Chemical Engineering,* vol. 10, no. 2, p. 107185, 2022/04/01/ 2022, doi: https://doi.org/10.1016/j.jece.2022.107185.

[13] A. Tomczyk, Z. Sokołowska, and P. Boguta, "Biochar physicochemical properties: pyrolysis temperature and feedstock kind effects," *Reviews in Environmental Science and Bio/Technology,* vol. 19, no. 1, pp. 191-215, 2020/03/01 2020, doi: 10.1007/s11157-020-09523-3.

[14] M. B. Soares, F. H. dos Santos, and L. R. F. Alleoni, "Iron-Modified Biochar from Sugarcane Straw to Remove Arsenic and Lead from Contaminated Water," *Water, Air, & Soil Pollution,* vol. 232, no. 9, p. 391, 2021/09/15 2021, doi: 10.1007/s11270-021-05343-5.

[15] C. Li *et al.*, "Impact of heating rates on the evolution of function groups of the biochar from lignin pyrolysis," *Journal of Analytical and Applied Pyrolysis,* vol. 155, p. 105031, 2021/05/01/ 2021, doi: https://doi.org/10.1016/j.jaap.2021.105031.

[16] A. A. Shagali *et al.*, "Comparative study on one-step pyrolysis activation of walnut shells to biochar at different heating rates," *Energy Reports,* vol. 7, pp. 388-396, 2021/11/01/ 2021, doi: https://doi.org/10.1016/j.egyr.2021.10.021.

[17] W. A. Rasaq, M. Golonka, M. Scholz, and A. Białowiec, "Opportunities and Challenges of High-Pressure Fast Pyrolysis of Biomass: A Review," *Energies,* vol. 14, no. 17, p. 5426, 2021. [Online]. Available: https://www.mdpi.com/1996-1073/14/17/5426.

[18] M. D. Ibrahim, Y. A. Abakr, S. Gan, L. Y. Lee, and S. Thangalazhy-Gopakumar, "Intermediate Pyrolysis of Bambara Groundnut Shell (BGS) in Various Inert Gases (N2, CO2, and N2/CO2)," *Energies,* vol. 15, no. 22, p. 8421, 2022. [Online]. Available: https://www.mdpi.com/1996-1073/15/22/8421.

[19] B. Mahanty and S. Mondal, "Synthesis of magnetic biochar using agricultural waste for the separation of Cr (VI) from aqueous solution," *Arabian Journal for Science and Engineering,* pp. 1-16, 2021.

[20] E.-B. Son, K.-M. Poo, J.-S. Chang, and K.-J. Chae, "Heavy metal removal from aqueous solutions using engineered magnetic biochars derived from waste marine macro-algal biomass," *Science of The Total Environment,* vol. 615, pp. 161-168, 2018/02/15/ 2018, doi: https://doi.org/10.1016/j.scitotenv.2017.09.171.

[21] Y. Peng *et al.*, "Zirconium hydroxide nanoparticle encapsulated magnetic biochar composite derived from rice residue: Application for As(III) and As(V) polluted water purification," *Journal of Hazardous Materials,* vol. 423, p. 127081, 2022/02/05/ 2022, doi: https://doi.org/10.1016/j.jhazmat.2021.127081.

[22] S. Zeng, Y.-K. Choi, and E. Kan, "Iron-activated bermudagrass-derived biochar for adsorption of aqueous sulfamethoxazole: effects of iron impregnation ratio on biochar

properties, adsorption, and regeneration," *Science of the Total Environment,* vol. 750, p. 141691, 2021.

[23] M. Sun, Y. Ma, Y. Yang, and X. Zhu, "Effect of iron impregnation ratio on the properties and adsorption of KOH activated biochar for removal of tetracycline and heavy metals," *Bioresource Technology,* vol. 380, p. 129081, 2023/07/01/ 2023, doi: https://doi.org/10.1016/j.biortech.2023.129081.

[24] L. Liu, X. Liu, D. Wang, H. Lin, and L. Huang, "Removal and reduction of Cr(VI) in simulated wastewater using magnetic biochar prepared by co-pyrolysis of nano-zero-valent iron and sewage sludge," *Journal of Cleaner Production,* vol. 257, p. 120562, 2020/06/01/ 2020, doi: https://doi.org/10.1016/j.jclepro.2020.120562.

[25] Y. Zhao *et al.*, "Green preparation of magnetic biochar for the effective accumulation of Pb(II): Performance and mechanism," *Chemical Engineering Journal,* vol. 375, p. 122011, 2019/11/01/ 2019, doi: https://doi.org/10.1016/j.cej.2019.122011.

[26] M. Zubair *et al.*, "Production of magnetic biochar-steel dust composites for enhanced phosphate adsorption," *Journal of Water Process Engineering,* vol. 47, p. 102793, 2022/06/01/ 2022, doi: https://doi.org/10.1016/j.jwpe.2022.102793.

[27] L. Wang *et al.*, "Performance and mechanisms for remediation of Cd(II) and As(III) co-contamination by magnetic biochar-microbe biochemical composite: Competition and synergy effects," *Science of The Total Environment,* vol. 750, p. 141672, 2021/01/01/ 2021, doi: https://doi.org/10.1016/j.scitotenv.2020.141672.

[28] J. Li, X. Chen, S. Yu, and M. Cui, "Removal of pristine and aged microplastics from water by magnetic biochar: Adsorption and magnetization," *Science of The Total Environment,* vol. 875, p. 162647, 2023/06/01/ 2023, doi: https://doi.org/10.1016/j.scitotenv.2023.162647.

[29] I. Wani, A. Sharma, V. Kushvaha, P. Madhushri, and L. Peng, "Effect of pH, Volatile Content, and Pyrolysis Conditions on Surface Area and O/C and H/C Ratios of Biochar: Towards Understanding Performance of Biochar Using Simplified Approach," *Journal of Hazardous, Toxic, and Radioactive Waste,* vol. 24, no. 4, p. 04020048, 2020/10/01 2020, doi: 10.1061/(ASCE)HZ.2153-5515.0000545.

[30] S. Dou, X.-X. Ke, Z.-D. Shao, L.-B. Zhong, Q.-B. Zhao, and Y.-M. Zheng, "Fish scale-based biochar with defined pore size and ultrahigh specific surface area for highly efficient

adsorption of ciprofloxacin," *Chemosphere,* vol. 287, p. 131962, 2022/01/01/ 2022, doi: https://doi.org/10.1016/j.chemosphere.2021.131962.

[31] D. Guo *et al.*, "Mechanism of efficient magnetic biochar for typical aqueous organic contaminant combined-adsorption removal," *Fuel Processing Technology,* vol. 247, p. 107795, 2023/08/01/ 2023, doi: https://doi.org/10.1016/j.fuproc.2023.107795.

[32] V. Gupta *et al.*, "Study on the removal of heavy metal ions from industry waste by carbon nanotubes: effect of the surface modification: a review," *Critical Reviews in Environmental Science and Technology,* vol. 46, no. 2, pp. 93-118, 2016.

[33] X. Yang *et al.*, "Surface functional groups of carbon-based adsorbents and their roles in the removal of heavy metals from aqueous solutions: A critical review," *Chemical Engineering Journal,* vol. 366, pp. 608-621, 2019/06/15/ 2019, doi: https://doi.org/10.1016/j.cej.2019.02.119.

[34] H. Li, X. Dong, E. B. da Silva, L. M. de Oliveira, Y. Chen, and L. Q. Ma, "Mechanisms of metal sorption by biochars: Biochar characteristics and modifications," *Chemosphere,* vol. 178, pp. 466-478, 2017/07/01/ 2017, doi: https://doi.org/10.1016/j.chemosphere.2017.03.072.

[35] J. Wu, T. Wang, Y. Zhang, and W.-P. Pan, "The distribution of Pb(II)/Cd(II) adsorption mechanisms on biochars from aqueous solution: Considering the increased oxygen functional groups by HCl treatment," *Bioresource Technology,* vol. 291, p. 121859, 2019/11/01/ 2019, doi: https://doi.org/10.1016/j.biortech.2019.121859.

[36] F. Hussin, M. K. Aroua, and M. Szlachta, "Biochar derived from fruit by-products using pyrolysis process for the elimination of Pb(II) ion: An updated review," *Chemosphere,* vol. 287, p. 132250, 2022/01/01/ 2022, doi: https://doi.org/10.1016/j.chemosphere.2021.132250.

[37] Y. Li *et al.*, "How does zero valent iron activating peroxydisulfate improve the dewatering of anaerobically digested sludge?," *Water research,* vol. 163, p. 114912, 2019.

[38] J. Yu *et al.*, "Magnetic nitrogen-doped sludge-derived biochar catalysts for persulfate activation: Internal electron transfer mechanism," *Chemical Engineering Journal,* vol. 364, pp. 146-159, 2019.

[39] Z. Wan and K. Li, "Effect of pre-pyrolysis mode on simultaneous introduction of nitrogen/oxygen-containing functional groups into the structure of bagasse-based

mesoporous carbon and its influence on Cu(II) adsorption," *Chemosphere,* vol. 194, pp. 370-380, 2018/03/01/ 2018, doi: https://doi.org/10.1016/j.chemosphere.2017.11.181.

[40] J. N. Knudsen, P. A. Jensen, W. Lin, F. J. Frandsen, and K. Dam-Johansen, "Sulfur transformations during thermal conversion of herbaceous biomass," *Energy & Fuels,* vol. 18, no. 3, pp. 810-819, 2004.

[41] K. Han, J. Gao, and J. Qi, "The study of sulphur retention characteristics of biomass briquettes during combustion," *Energy,* vol. 186, p. 115788, 2019.

[42] T. Velempini and K. Pillay, "Sulphur functionalized materials for Hg (II) adsorption: A review," *Journal of environmental Chemical engineering,* vol. 7, no. 5, p. 103350, 2019.

[43] M. Yin *et al.*, "Sulfur-functional group tunning on biochar through sodium thiosulfate modified molten salt process for efficient heavy metal adsorption," *Chemical Engineering Journal,* vol. 433, p. 134441, 2022/04/01/ 2022, doi: https://doi.org/10.1016/j.cej.2021.134441.

[44] L. Qian *et al.*, "Effective removal of heavy metal by biochar colloids under different pyrolysis temperatures," *Bioresource Technology,* vol. 206, pp. 217-224, 2016/04/01/ 2016, doi: https://doi.org/10.1016/j.biortech.2016.01.065.

[45] N.-H. Hsu, S.-L. Wang, Y.-C. Lin, G. D. Sheng, and J.-F. Lee, "Reduction of Cr(VI) by Crop-Residue-Derived Black Carbon," *Environmental Science & Technology,* vol. 43, no. 23, pp. 8801-8806, 2009/12/01 2009, doi: 10.1021/es901872x.

[46] H. Tounsadi *et al.*, "Highly efficient activated carbon from Glebionis coronaria L. biomass: Optimization of preparation conditions and heavy metals removal using experimental design approach," *Journal of Environmental Chemical Engineering,* vol. 4, no. 4, pp. 4549-4564, 2016.

[47] H. Yuan, T. Lu, H. Huang, D. Zhao, N. Kobayashi, and Y. Chen, "Influence of pyrolysis temperature on physical and chemical properties of biochar made from sewage sludge," *Journal of Analytical and Applied Pyrolysis,* vol. 112, pp. 284-289, 2015/03/01/ 2015, doi: https://doi.org/10.1016/j.jaap.2015.01.010.

[48] Y. Chen, X. Zhang, W. Chen, H. Yang, and H. Chen, "The structure evolution of biochar from biomass pyrolysis and its correlation with gas pollutant adsorption performance," *Bioresource Technology,* vol. 246, pp. 101-109, 2017/12/01/ 2017, doi: https://doi.org/10.1016/j.biortech.2017.08.138.

[49] Z. Xiong *et al.*, "Physicochemical and adsorption properties of biochar from biomass-based pyrolytic polygeneration: effects of biomass species and temperature," *Biochar,* vol. 3, no. 4, pp. 657-670, 2021/12/01 2021, doi: 10.1007/s42773-021-00102-5.

[50] C. Yang, J. Liu, and S. Lu, "Pyrolysis temperature affects pore characteristics of rice straw and canola stalk biochars and biochar-amended soils," *Geoderma,* vol. 397, p. 115097, 2021/09/01/ 2021, doi: https://doi.org/10.1016/j.geoderma.2021.115097.

[51] J. Dobrzyńska, A. Wysokińska, and R. Olchowski, "Raspberry stalks-derived biochar, magnetic biochar and urea modified magnetic biochar - Synthesis, characterization and application for As(V) and Cr(VI) removal from river water," *Journal of Environmental Management,* vol. 316, p. 115260, 2022/08/15/ 2022, doi: https://doi.org/10.1016/j.jenvman.2022.115260.

[52] J. Wang, C. Sun, Q.-X. Huang, Y. Chi, and J.-H. Yan, "Adsorption and thermal degradation of microplastics from aqueous solutions by Mg/Zn modified magnetic biochars," *Journal of Hazardous Materials,* vol. 419, p. 126486, 2021/10/05/ 2021, doi: https://doi.org/10.1016/j.jhazmat.2021.126486.

[53] L. Zheng *et al.*, "A novel, recyclable magnetic biochar modified by chitosan–EDTA for the effective removal of Pb (II) from aqueous solution," *RSC advances,* vol. 10, no. 66, pp. 40196-40205, 2020.

[54] Z. H. Khan, M. Gao, W. Qiu, and Z. Song, "Properties and adsorption mechanism of magnetic biochar modified with molybdenum disulfide for cadmium in aqueous solution," *Chemosphere,* vol. 255, p. 126995, 2020/09/01/ 2020, doi: https://doi.org/10.1016/j.chemosphere.2020.126995.

[55] H. Wang, W. Zhao, Y. Chen, and Y. Li, "Nickel aluminum layered double oxides modified magnetic biochar from waste corncob for efficient removal of acridine orange," *Bioresource Technology,* vol. 315, p. 123834, 2020/11/01/ 2020, doi: https://doi.org/10.1016/j.biortech.2020.123834.

[56] Y. Shi *et al.*, "Removal of nanoplastics from aqueous solution by aggregation using reusable magnetic biochar modified with cetyltrimethylammonium bromide," *Environmental Pollution,* vol. 318, p. 120897, 2023/02/01/ 2023, doi: https://doi.org/10.1016/j.envpol.2022.120897.

[57] Y. Chen, W. Mao, W. Yang, N. K. Niazi, B. Wang, and P. Wu, "A novel phosphate rock-magnetic biochar for Pb2+ and Cd2+ removal in wastewater: Characterization, performance and mechanisms," *Environmental Technology & Innovation,* vol. 32, p. 103268, 2023/11/01/ 2023, doi: https://doi.org/10.1016/j.eti.2023.103268.

[58] J. Zhu, T. Rui, Y. You, D. Shen, and T. Liu, "Magnetic biochar with Mg/La modification for highly effective phosphate adsorption and its potential application as an algaecide and fertilizer," *Environmental Research,* vol. 231, p. 116252, 2023/08/15/ 2023, doi: https://doi.org/10.1016/j.envres.2023.116252.

[59] S. Fan, X. Fan, S. Wang, B. Li, N. Zhou, and H. Xu, "Effect of chitosan modification on the properties of magnetic porous biochar and its adsorption performance towards tetracycline and Cu2+," *Sustainable Chemistry and Pharmacy,* vol. 33, p. 101057, 2023/06/01/ 2023, doi: https://doi.org/10.1016/j.scp.2023.101057.

[60] H. Muhammad *et al.*, "Study of soil microorganisms modified wheat straw and biochar for reducing cadmium leaching potential and bioavailability," *Chemosphere,* vol. 273, p. 129644, 2021/06/01/ 2021, doi: https://doi.org/10.1016/j.chemosphere.2021.129644.

[61] R. Azargohar and A. K. Dalai, "Steam and KOH activation of biochar: Experimental and modeling studies," *Microporous and Mesoporous Materials,* vol. 110, no. 2, pp. 413-421, 2008/04/15/ 2008, doi: https://doi.org/10.1016/j.micromeso.2007.06.047.

[62] J.-H. Kwak *et al.*, "Biochar properties and lead(II) adsorption capacity depend on feedstock type, pyrolysis temperature, and steam activation," *Chemosphere,* vol. 231, pp. 393-404, 2019/09/01/ 2019, doi: https://doi.org/10.1016/j.chemosphere.2019.05.128.

[63] A. U. Rajapaksha *et al.*, "Enhanced sulfamethazine removal by steam-activated invasive plant-derived biochar," *Journal of Hazardous Materials,* vol. 290, pp. 43-50, 2015/06/15/ 2015, doi: https://doi.org/10.1016/j.jhazmat.2015.02.046.

[64] P. R. Yaashikaa, P. Senthil Kumar, S. J. Varjani, and A. Saravanan, "Advances in production and application of biochar from lignocellulosic feedstocks for remediation of environmental pollutants," *Bioresource Technology,* vol. 292, p. 122030, 2019/11/01/ 2019, doi: https://doi.org/10.1016/j.biortech.2019.122030.

[65] M. H. Su *et al.*, "Simultaneous removal of toxic ammonia and lettuce cultivation in aquaponic system using microwave pyrolysis biochar," *Journal of hazardous materials,* vol. 396, p. 122610, 2020.

[66] R.-Z. Wang *et al.*, "Synergistic removal of copper and tetracycline from aqueous solution by steam-activated bamboo-derived biochar," *Journal of Hazardous Materials,* vol. 384, p. 121470, 2020/02/15/ 2020, doi: https://doi.org/10.1016/j.jhazmat.2019.121470.

[67] B. Sajjadi, W.-Y. Chen, and N. O. Egiebor, "A comprehensive review on physical activation of biochar for energy and environmental applications," vol. 35, no. 6, pp. 735-776, 2019, doi: doi:10.1515/revce-2017-0113.

[68] A. K. Dalai and R. Azargohar, "Production of Activated Carbon from Biochar Using Chemical and Physical Activation: Mechanism and Modeling," in *Materials, Chemicals, and Energy from Forest Biomass*, vol. 954, (ACS Symposium Series, no. 954): American Chemical Society, 2007, ch. 29, pp. 463-476.

[69] H. Zhang, X. Yue, F. Li, R. Xiao, Y. Zhang, and D. Gu, "Preparation of rice straw-derived biochar for efficient cadmium removal by modification of oxygen-containing functional groups," *Science of The Total Environment,* vol. 631-632, pp. 795-802, 2018/08/01/ 2018, doi: https://doi.org/10.1016/j.scitotenv.2018.03.071.

[70] M. Chen, F. Wang, D.-l. Zhang, W.-m. Yi, and Y. Liu, "Effects of acid modification on the structure and adsorption NH4+-N properties of biochar," *Renewable Energy,* vol. 169, pp. 1343-1350, 2021/05/01/ 2021, doi: https://doi.org/10.1016/j.renene.2021.01.098.

[71] P. Boguta, Z. Sokołowska, K. Skic, and A. Tomczyk, "Chemically engineered biochar – Effect of concentration and type of modifier on sorption and structural properties of biochar from wood waste," *Fuel,* vol. 256, p. 115893, 2019/11/15/ 2019, doi: https://doi.org/10.1016/j.fuel.2019.115893.

[72] C. Liu *et al.*, "Preparation of Acid- and Alkali-Modified Biochar for Removal of Methylene Blue Pigment," *ACS Omega,* vol. 5, no. 48, pp. 30906-30922, 2020/12/08 2020, doi: 10.1021/acsomega.0c03688.

[73] P. M. Godwin, Y. Pan, H. Xiao, and M. T. Afzal, "Progress in Preparation and Application of Modified Biochar for Improving Heavy Metal Ion Removal From Wastewater," *Journal of Bioresources and Bioproducts,* vol. 4, no. 1, pp. 31-42, 2019/02/01/ 2019, doi: https://doi.org/10.21967/jbb.v4i1.180.

[74] Q. An, Y. Miao, B. Zhao, Z. Li, and S. Zhu, "An alkali modified biochar for enhancing Mn2+ adsorption: Performance and chemical mechanism," *Materials Chemistry and*

Physics, vol. 248, p. 122895, 2020/07/01/ 2020, doi: https://doi.org/10.1016/j.matchemphys.2020.122895.

[75] V.-T. Nguyen, T.-B. Nguyen, C. P. Huang, C.-W. Chen, X.-T. Bui, and C.-D. Dong, "Alkaline modified biochar derived from spent coffee ground for removal of tetracycline from aqueous solutions," *Journal of Water Process Engineering,* vol. 40, p. 101908, 2021/04/01/ 2021, doi: https://doi.org/10.1016/j.jwpe.2020.101908.

[76] Q. Tao *et al.*, "An integrated method to produce fermented liquid feed and biologically modified biochar as cadmium adsorbents using corn stalks," *Waste Management,* vol. 127, pp. 112-120, 2021/05/15/ 2021, doi: https://doi.org/10.1016/j.wasman.2021.04.027.

[77] G. J. F. Cruz *et al.*, "Agrowaste derived biochars impregnated with ZnO for removal of arsenic and lead in water," *Journal of Environmental Chemical Engineering,* vol. 8, no. 3, p. 103800, 2020/06/01/ 2020, doi: https://doi.org/10.1016/j.jece.2020.103800.

[78] Y. Ma *et al.*, "A novel, efficient and sustainable magnetic sludge biochar modified by graphene oxide for environmental concentration imidacloprid removal," *Journal of Hazardous Materials,* vol. 407, p. 124777, 2021/04/05/ 2021, doi: https://doi.org/10.1016/j.jhazmat.2020.124777.

[79] J. S. d. S. Carneiro *et al.*, "Biochar-graphene oxide composite is efficient to adsorb and deliver copper and zinc in tropical soil," *Journal of Cleaner Production,* vol. 360, p. 132170, 2022/08/01/ 2022, doi: https://doi.org/10.1016/j.jclepro.2022.132170.

[80] J.-G. Kim, H.-B. Kim, and K. Baek, "Novel electrochemical method to activate biochar derived from spent coffee grounds for enhanced adsorption of lead (Pb)," *Science of The Total Environment,* vol. 886, p. 163891, 2023/08/15/ 2023, doi: https://doi.org/10.1016/j.scitotenv.2023.163891.

[81] W. Mao, Y. Zhang, J. Luo, L. Chen, and Y. Guan, "Novel co-polymerization of polypyrrole/polyaniline on ferrate modified biochar composites for the efficient adsorption of hexavalent chromium in water," *Chemosphere,* vol. 303, p. 135254, 2022/09/01/ 2022, doi: https://doi.org/10.1016/j.chemosphere.2022.135254.

[82] S. Zhu *et al.*, "Green sustainable and highly efficient hematite nanoparticles modified biochar-clay granular composite for Cr(VI) removal and related mechanism," *Journal of Cleaner Production,* vol. 276, p. 123009, 2020/12/10/ 2020, doi: https://doi.org/10.1016/j.jclepro.2020.123009.

[83] S. Cheng, Y. Liu, B. Xing, X. Qin, C. Zhang, and H. Xia, "Lead and cadmium clean removal from wastewater by sustainable biochar derived from poplar saw dust," *Journal of Cleaner Production,* vol. 314, p. 128074, 2021.

[84] T. Chen, Z. Zhou, R. Han, R. Meng, H. Wang, and W. Lu, "Adsorption of cadmium by biochar derived from municipal sewage sludge: impact factors and adsorption mechanism," *Chemosphere,* vol. 134, pp. 286-293, 2015.

[85] H. Fu, S. Ma, S. Xu, R. Duan, G. Cheng, and P. Zhao, "Hierarchically porous magnetic biochar as an efficient amendment for cadmium in water and soil: Performance and mechanism," *Chemosphere,* vol. 281, p. 130990, 2021/10/01/ 2021, doi: https://doi.org/10.1016/j.chemosphere.2021.130990.

[86] S. Fendorf, B. W. Wielinga, and C. M. Hansel, "Chromium transformations in natural environments: the role of biological and abiological processes in chromium (VI) reduction," *International Geology Review,* vol. 42, no. 8, pp. 691-701, 2000.

[87] A. Ekanayake, A. U. Rajapaksha, R. Selvasembian, and M. Vithanage, "Amino-functionalized biochars for the detoxification and removal of hexavalent chromium in aqueous media," *Environmental Research,* vol. 211, p. 113073, 2022/08/01/ 2022, doi: https://doi.org/10.1016/j.envres.2022.113073.

[88] M. A. Hashem, M. A. Momen, M. Hasan, M. S. Nur-A-Tomal, and M. H. R. Sheikh, "Chromium removal from tannery wastewater using Syzygium cumini bark adsorbent," *International Journal of Environmental Science and Technology,* vol. 16, no. 3, pp. 1395-1404, 2019/03/01 2019, doi: 10.1007/s13762-018-1714-y.

[89] J.-j. Pan, J. Jiang, and R.-k. Xu, "Removal of Cr(VI) from aqueous solutions by Na2SO3/FeSO4 combined with peanut straw biochar," *Chemosphere,* vol. 101, pp. 71-76, 2014/04/01/ 2014, doi: https://doi.org/10.1016/j.chemosphere.2013.12.026.

[90] R. Sinha *et al.*, "Single-step synthesis of activated magnetic biochar derived from rice husk for hexavalent chromium adsorption: Equilibrium mechanism, kinetics, and thermodynamics analysis," *Groundwater for Sustainable Development,* vol. 18, p. 100796, 2022/08/01/ 2022, doi: https://doi.org/10.1016/j.gsd.2022.100796.

[91] H. Wang, M. Zhang, and Q. Lv, "Removal efficiency and mechanism of Cr (VI) from aqueous solution by maize straw biochars derived at different pyrolysis temperatures," *Water,* vol. 11, no. 4, p. 781, 2019.

[92] V.-P. Dinh *et al.*, "Adsorption of Pb(II) from aqueous solution by pomelo fruit peel-derived biochar," *Materials Chemistry and Physics,* vol. 285, p. 126105, 2022/06/01/ 2022, doi: https://doi.org/10.1016/j.matchemphys.2022.126105.

[93] L. Gao *et al.*, "Impacts of pyrolysis temperature on lead adsorption by cotton stalk-derived biochar and related mechanisms," *Journal of Environmental Chemical Engineering,* vol. 9, no. 4, p. 105602, 2021/08/01/ 2021, doi: https://doi.org/10.1016/j.jece.2021.105602.

[94] J. Wu, T. Wang, J. Wang, Y. Zhang, and W.-P. Pan, "A novel modified method for the efficient removal of Pb and Cd from wastewater by biochar: Enhanced the ion exchange and precipitation capacity," *Science of The Total Environment,* vol. 754, p. 142150, 2021/02/01/ 2021, doi: https://doi.org/10.1016/j.scitotenv.2020.142150.

[95] S. Wang, J.-H. Kwak, M. S. Islam, M. A. Naeth, M. Gamal El-Din, and S. X. Chang, "Biochar surface complexation and Ni(II), Cu(II), and Cd(II) adsorption in aqueous solutions depend on feedstock type," *Science of The Total Environment,* vol. 712, p. 136538, 2020/04/10/ 2020, doi: https://doi.org/10.1016/j.scitotenv.2020.136538.

[96] Y. Deng, S. Huang, C. Dong, Z. Meng, and X. Wang, "Competitive adsorption behaviour and mechanisms of cadmium, nickel and ammonium from aqueous solution by fresh and ageing rice straw biochars," *Bioresource Technology,* vol. 303, p. 122853, 2020/05/01/ 2020, doi: https://doi.org/10.1016/j.biortech.2020.122853.

[97] Z. Shen, Y. Zhang, O. McMillan, F. Jin, and A. Al-Tabbaa, "Characteristics and mechanisms of nickel adsorption on biochars produced from wheat straw pellets and rice husk," *Environmental Science and Pollution Research,* vol. 24, no. 14, pp. 12809-12819, 2017/05/01 2017, doi: 10.1007/s11356-017-8847-2.

[98] G. Qi *et al.*, "Microwave biochar produced with activated carbon catalyst: Characterization and adsorption of heavy metals," *Environmental Research,* vol. 216, p. 114732, 2023/01/01/ 2023, doi: https://doi.org/10.1016/j.envres.2022.114732.

[99] A. Medyńska-Juraszek, I. Ćwieląg-Piasecka, M. Jerzykiewicz, and J. Trynda, "Wheat Straw Biochar as a Specific Sorbent of Cobalt in Soil," *Materials,* vol. 13, no. 11, p. 2462, 2020. [Online]. Available: https://www.mdpi.com/1996-1944/13/11/2462.

[100] V. G. Georgieva, L. Gonsalvesh, and M. P. Tavlieva, "Thermodynamics and kinetics of the removal of nickel (II) ions from aqueous solutions by biochar adsorbent made from

agro-waste walnut shells," *Journal of Molecular Liquids,* vol. 312, p. 112788, 2020/08/15/ 2020, doi: https://doi.org/10.1016/j.molliq.2020.112788.

[101] E. Baltrėnaitė-Gedienė, T. Leonavičienė, and P. Baltrėnas, "Comparison of CU(II), MN(II) and ZN(II) adsorption on biochar using diagnostic and simulation models," *Chemosphere,* vol. 245, p. 125562, 2020/04/01/ 2020, doi: https://doi.org/10.1016/j.chemosphere.2019.125562.

[102] S. Lin, W. Huang, H. Yang, S. Sun, and J. Yu, "Recycling application of waste long-root Eichhornia crassipes in the heavy metal removal using oxidized biochar derived as adsorbents," *Bioresource Technology,* vol. 314, p. 123749, 2020/10/01/ 2020, doi: https://doi.org/10.1016/j.biortech.2020.123749.

[103] M. Wu, B. Liu, J. Li, X. Su, W. Liu, and X. Li, "Influence of pyrolysis temperature on sludge biochar: the ecological risk assessment of heavy metals and the adsorption of Cd(II)," *Environmental Science and Pollution Research,* vol. 30, no. 5, pp. 12608-12617, 2023/01/01 2023, doi: 10.1007/s11356-022-22827-x.

[104] X. He, J. Jiang, Z. Hong, X. Pan, Y. Dong, and R. Xu, "Effect of aluminum modification of rice straw–based biochar on arsenate adsorption," *Journal of Soils and Sediments,* vol. 20, no. 8, pp. 3073-3082, 2020/08/01 2020, doi: 10.1007/s11368-020-02595-2.

[105] D. Xu, T. Sun, H. Jia, Y. Sun, and X. Zhu, "The performance and mechanism of Cr(VI) adsorption by biochar derived from Potamogeton crispus at different pyrolysis temperatures," *Journal of Analytical and Applied Pyrolysis,* vol. 167, p. 105662, 2022/10/01/ 2022, doi: https://doi.org/10.1016/j.jaap.2022.105662.

[106] L. Chen *et al.*, "Microwave-assisted pyrolysis of waste lignin to prepare biochar for Cu2+ highly-efficient adsorption: Performance, kinetics and mechanism resolution," *Separation and Purification Technology,* vol. 342, p. 127070, 2024/08/21/ 2024, doi: https://doi.org/10.1016/j.seppur.2024.127070.

[107] X. Guo, M. Li, A. Liu, M. Jiang, X. Niu, and X. Liu, "Adsorption Mechanisms and Characteristics of Hg2+ Removal by Different Fractions of Biochar," *Water,* vol. 12, no. 8, p. 2105, 2020. [Online]. Available: https://www.mdpi.com/2073-4441/12/8/2105.

[108] M. A. Hashem, M. Hasan, M. A. Momen, S. Payel, and M. S. Nur-A-Tomal, "Water hyacinth biochar for trivalent chromium adsorption from tannery wastewater,"

Environmental and Sustainability Indicators, vol. 5, p. 100022, 2020/02/01/ 2020, doi: https://doi.org/10.1016/j.indic.2020.100022.

[109] Q.-M. Truong *et al.*, "Magnetic biochar derived from macroalgal Sargassum hemiphyllum for highly efficient adsorption of Cu(II): Influencing factors and reusability," *Bioresource Technology,* vol. 361, p. 127732, 2022/10/01/ 2022, doi: https://doi.org/10.1016/j.biortech.2022.127732.

[110] P. Maneechakr and S. Mongkollertlop, "Investigation on adsorption behaviors of heavy metal ions (Cd2+, Cr3+, Hg2+ and Pb2+) through low-cost/active manganese dioxide-modified magnetic biochar derived from palm kernel cake residue," *Journal of Environmental Chemical Engineering,* vol. 8, no. 6, p. 104467, 2020/12/01/ 2020, doi: https://doi.org/10.1016/j.jece.2020.104467.

[111] V. Singh *et al.*, "Adsorption Studies of Pb(II) and Cd(II) Heavy Metal Ions from Aqueous Solutions Using a Magnetic Biochar Composite Material," *Separations,* vol. 10, no. 7, p. 389, 2023. [Online]. Available: https://www.mdpi.com/2297-8739/10/7/389.

[112] K. Shirvanimoghaddam *et al.*, "Sustainable synthesis of rose flower-like magnetic biochar from tea waste for environmental applications," *Journal of Advanced Research,* vol. 34, pp. 13-27, 2021/12/01/ 2021, doi: https://doi.org/10.1016/j.jare.2021.08.001.

[113] B. C. Nyamunda, T. Chivhanga, U. Guyo, and F. Chigondo, "Removal of Zn (II) and Cu (II) ions from industrial wastewaters using magnetic biochar derived from water hyacinth," *Journal of Engineering,* vol. 2019, no. 1, p. 5656983, 2019.

[114] R. Isaac, S. Siddiqui, O. F. Aldosari, and M. Kashif Uddin, "Magnetic biochar derived from Juglans regia for the adsorption of Cu2+ and Ni2+: Characterization, modelling, optimization, and cost analysis," *Journal of Saudi Chemical Society,* vol. 27, no. 6, p. 101749, 2023/11/01/ 2023, doi: https://doi.org/10.1016/j.jscs.2023.101749.

[115] J. Azadmanjiri, P. Kumar, V. K. Srivastava, and Z. Sofer, "Surface functionalization of 2D transition metal oxides and dichalcogenides via covalent and non-covalent bonding for sustainable energy and biomedical applications," *ACS Applied Nano Materials,* vol. 3, no. 4, pp. 3116-3143, 2020.

[116] P. Heinrich, L. Hanslik, N. Kämmer, and T. Braunbeck, "The tox is in the detail: technical fundamentals for designing, performing, and interpreting experiments on toxicity of

microplastics and associated substances," *Environmental Science and Pollution Research,* vol. 27, pp. 22292-22318, 2020.

[117] Z. Liu *et al.*, "Nanoporous biochar with high specific surface area based on rice straw digestion residue for efficient adsorption of mercury ion from water," *Bioresource Technology,* vol. 359, p. 127471, 2022/09/01/ 2022, doi: https://doi.org/10.1016/j.biortech.2022.127471.

[118] J. Shin *et al.*, "Facilitated physisorption of ibuprofen on waste coffee residue biochars through simultaneous magnetization and activation in groundwater and lake water: Adsorption mechanisms and reusability," *Journal of Environmental Chemical Engineering,* vol. 10, no. 3, p. 107914, 2022/06/01/ 2022, doi: https://doi.org/10.1016/j.jece.2022.107914.

[119] S. Lee, J. Han, and H.-M. Ro, "Mechanistic insights into Cd(II) and As(V) sorption on Miscanthus biochar at different pH values and pyrolysis temperatures," *Chemosphere,* vol. 287, p. 132179, 2022/01/01/ 2022, doi: https://doi.org/10.1016/j.chemosphere.2021.132179.

[120] I. W. Almanassra *et al.*, "Palm leaves based biochar: advanced material characterization and heavy metal adsorption study," *Biomass Conversion and Biorefinery,* vol. 14, no. 13, pp. 14811-14830, 2024/07/01 2024, doi: 10.1007/s13399-022-03590-y.

[121] Y. Li, S. Wang, X. F. Ouyang, Z. Dang, and H. Yin, "Acetate anions intercalated Fe/Mg-layered double hydroxides modified biochar for efficient adsorption of anionic and cationic heavy metal ions from polluted water," *Chemosphere,* vol. 362, p. 142652, 2024/08/01/ 2024, doi: https://doi.org/10.1016/j.chemosphere.2024.142652.

[122] G. Midekessa *et al.*, "Zeta potential of extracellular vesicles: toward understanding the attributes that determine colloidal stability," *ACS omega,* vol. 5, no. 27, pp. 16701-16710, 2020.

[123] Y. Chen *et al.*, "Novel Magnetic Pomelo Peel Biochar for Enhancing Pb(II) And Cu(II) Adsorption: Performance and Mechanism," *Water, Air, & Soil Pollution,* vol. 231, no. 8, p. 404, 2020/07/25 2020, doi: 10.1007/s11270-020-04788-4.

[124] W. Yu *et al.*, "Facile preparation of sulfonated biochar for highly efficient removal of toxic Pb(II) and Cd(II) from wastewater," *Science of The Total Environment,* vol. 750, p. 141545, 2021/01/01/ 2021, doi: https://doi.org/10.1016/j.scitotenv.2020.141545.

[125] C.-K. Chen, J.-J. Chen, N.-T. Nguyen, T.-T. Le, N.-C. Nguyen, and C.-T. Chang, "Specifically designed magnetic biochar from waste wood for arsenic removal," *Sustainable Environment Research,* vol. 31, no. 1, p. 29, 2021/09/22 2021, doi: 10.1186/s42834-021-00100-z.

[126] Y. Wang, X. Chen, J. Yan, T. Wang, X. Xie, and S. Yang, "Efficient removal arsenate from water by biochar-loaded Ce3+-enriched ultra-fine ceria nanoparticles through adsorption-precipitation," *Science of The Total Environment,* vol. 794, p. 148691, 2021/11/10/ 2021, doi: https://doi.org/10.1016/j.scitotenv.2021.148691.

[127] X. Guo *et al.*, "Adsorption mechanism of hexavalent chromium on biochar: kinetic, thermodynamic, and characterization studies," *ACS omega,* vol. 5, no. 42, pp. 27323-27331, 2020.

[128] X. Liu, G. Li, C. Chen, X. Zhang, K. Zhou, and X. Long, "Banana stem and leaf biochar as an effective adsorbent for cadmium and lead in aqueous solution," *Scientific Reports,* vol. 12, no. 1, p. 1584, 2022.

[129] Y.-P. Wang, Y.-L. Liu, S.-Q. Tian, J.-J. Yang, L. Wang, and J. Ma, "Straw biochar enhanced removal of heavy metal by ferrate," *Journal of Hazardous Materials,* vol. 416, p. 126128, 2021.

[130] M. Guo, W. Song, and J. Tian, "Biochar-facilitated soil remediation: mechanisms and efficacy variations," *Frontiers in Environmental Science,* vol. 8, p. 521512, 2020.

[131] R. Shan *et al.*, "Photocatalytic degradation of methyl orange by Ag/TiO2/biochar composite catalysts in aqueous solutions," *Materials Science in Semiconductor Processing,* vol. 114, p. 105088, 2020/08/01/ 2020, doi: https://doi.org/10.1016/j.mssp.2020.105088.

[132] D. Guo *et al.*, "Natural adsorption of methylene blue by waste fallen leaves of Magnoliaceae and its repeated thermal regeneration for reuse," *Journal of Cleaner Production,* vol. 267, p. 121903, 2020/09/10/ 2020, doi: https://doi.org/10.1016/j.jclepro.2020.121903.

[133] M. Vakili *et al.*, "Regeneration of exhausted adsorbents after PFAS adsorption: A critical review," *Journal of Hazardous Materials,* vol. 471, p. 134429, 2024/06/05/ 2024, doi: https://doi.org/10.1016/j.jhazmat.2024.134429.

[134] T. Alsawy, E. Rashad, M. El-Qelish, and R. H. Mohammed, "A comprehensive review on the chemical regeneration of biochar adsorbent for sustainable wastewater treatment," *Npj Clean Water,* vol. 5, no. 1, p. 29, 2022.

[135] T. Fazal *et al.*, "Macroalgae and coal-based biochar as a sustainable bioresource reuse for treatment of textile wastewater," *Biomass Conversion and Biorefinery,* vol. 11, no. 5, pp. 1491-1506, 2021/10/01 2021, doi: 10.1007/s13399-019-00555-6.

[136] S. Sireesha, U. Upadhyay, and I. Sreedhar, "Comparative studies of heavy metal removal from aqueous solution using novel biomass and biochar-based adsorbents: characterization, process optimization, and regeneration," *Biomass Conversion and Biorefinery,* 2022/01/15 2022, doi: 10.1007/s13399-021-02186-2.

[137] H. Zeng, W. Qi, L. Zhai, F. Wang, J. Zhang, and D. Li, "Preparation and characterization of sludge-based magnetic biochar by pyrolysis for methylene blue removal," *Nanomaterials,* vol. 11, no. 10, p. 2473, 2021.

[138] W. Ahmed *et al.*, "Adsorption of Pb(II) from wastewater using a red mud modified rice-straw biochar: Influencing factors and reusability," *Environmental Pollution,* vol. 326, p. 121405, 2023/06/01/ 2023, doi: https://doi.org/10.1016/j.envpol.2023.121405.

[139] D. R. Kandel *et al.*, "Cold plasma-assisted regeneration of biochar for dye adsorption," *Chemosphere,* vol. 309, p. 136638, 2022/12/01/ 2022, doi: https://doi.org/10.1016/j.chemosphere.2022.136638.

[140] Z. Jia, W. Zeng, H. Xu, S. Li, and Y. Peng, "Adsorption removal and reuse of phosphate from wastewater using a novel adsorbent of lanthanum-modified platanus biochar," *Process Safety and Environmental Protection,* vol. 140, pp. 221-232, 2020/08/01/ 2020, doi: https://doi.org/10.1016/j.psep.2020.05.017.

[141] S. F. Soares, C. O. Amorim, J. S. Amaral, T. Trindade, and A. L. Daniel-da-Silva, "On the efficient removal, regeneration and reuse of quaternary chitosan magnetite nanosorbents for glyphosate herbicide in water," *Journal of Environmental Chemical Engineering,* vol. 9, no. 3, p. 105189, 2021/06/01/ 2021, doi: https://doi.org/10.1016/j.jece.2021.105189.

[142] U. Kingsley and J. Tien-Chien, "Biochar and Application of Machine Learning: A Review," in *Biochar*, B. Mattia, G. Mauro, and T. Alberto Eds. Rijeka: IntechOpen, 2022, p. Ch. 14.

[143] A. El Hanandeh, Z. Mahdi, and M. S. Imtiaz, "Modelling of the adsorption of Pb, Cu and Ni ions from single and multi-component aqueous solutions by date seed derived biochar: Comparison of six machine learning approaches," *Environmental Research,* vol. 192, p. 110338, 2021/01/01/ 2021, doi: https://doi.org/10.1016/j.envres.2020.110338.

[144] S. Kumari, J. Chowdhry, M. Kumar, and M. C. Garg, "Machine learning (ML): An emerging tool to access the production and application of biochar in the treatment of contaminated water and wastewater," *Groundwater for Sustainable Development,* vol. 26, p. 101243, 2024/08/01/ 2024, doi: https://doi.org/10.1016/j.gsd.2024.101243.

[145] K. V. Supraja *et al.*, "Biochar production and its environmental applications: Recent developments and machine learning insights," *Bioresource Technology,* vol. 387, p. 129634, 2023/11/01/ 2023, doi: https://doi.org/10.1016/j.biortech.2023.129634.

[146] Y. Zhao, Y. Li, D. Fan, J. Song, and F. Yang, "Application of kernel extreme learning machine and Kriging model in prediction of heavy metals removal by biochar," *Bioresource Technology,* vol. 329, p. 124876, 2021/06/01/ 2021, doi: https://doi.org/10.1016/j.biortech.2021.124876.

[147] W. Zhang *et al.*, "Synthesis optimization and adsorption modeling of biochar for pollutant removal via machine learning," *Biochar,* vol. 5, no. 1, p. 25, 2023/04/23 2023, doi: 10.1007/s42773-023-00225-x.

[148] X. Zhu, Y. Li, and X. Wang, "Machine learning prediction of biochar yield and carbon contents in biochar based on biomass characteristics and pyrolysis conditions," *Bioresource Technology,* vol. 288, p. 121527, 2019/09/01/ 2019, doi: https://doi.org/10.1016/j.biortech.2019.121527.

[149] L. Leng *et al.*, "Machine learning predicting and engineering the yield, N content, and specific surface area of biochar derived from pyrolysis of biomass," *Biochar,* vol. 4, no. 1, p. 63, 2022/11/29 2022, doi: 10.1007/s42773-022-00183-w.

[150] A. Hai *et al.*, "Machine learning models for the prediction of total yield and specific surface area of biochar derived from agricultural biomass by pyrolysis," *Environmental Technology & Innovation,* vol. 30, p. 103071, 2023/05/01/ 2023, doi: https://doi.org/10.1016/j.eti.2023.103071.

[151] R. Potnuri, D. V. Suriapparao, C. Sankar Rao, V. Sridevi, and A. Kumar, "Effect of dry torrefaction pretreatment of the microwave-assisted catalytic pyrolysis of biomass using

the machine learning approach," *Renewable Energy,* vol. 197, pp. 798-809, 2022/09/01/ 2022, doi: https://doi.org/10.1016/j.renene.2022.08.006.

[152] S. R. Narde and N. Remya, "Biochar production from agricultural biomass through microwave-assisted pyrolysis: predictive modelling and experimental validation of biochar yield," *Environment, Development and Sustainability,* vol. 24, no. 9, pp. 11089-11102, 2022/09/01 2022, doi: 10.1007/s10668-021-01898-9.

[153] Y. Li, R. Gupta, and S. You, "Machine learning assisted prediction of biochar yield and composition via pyrolysis of biomass," *Bioresource Technology,* vol. 359, p. 127511, 2022/09/01/ 2022, doi: https://doi.org/10.1016/j.biortech.2022.127511.

[154] D. Lakshmi *et al.*, "Artificial intelligence (AI) applications in adsorption of heavy metals using modified biochar," *Science of The Total Environment,* vol. 801, p. 149623, 2021/12/20/ 2021, doi: https://doi.org/10.1016/j.scitotenv.2021.149623.

[155] H. Shahbeik *et al.*, "Characterizing sludge pyrolysis by machine learning: Towards sustainable bioenergy production from wastes," *Renewable Energy,* vol. 199, pp. 1078-1092, 2022/11/01/ 2022, doi: https://doi.org/10.1016/j.renene.2022.09.022.

[156] J. C. Ang *et al.*, "Development of predictive model for biochar surface properties based on biomass attributes and pyrolysis conditions using rough set machine learning," *Biomass and Bioenergy,* vol. 174, p. 106820, 2023/07/01/ 2023, doi: https://doi.org/10.1016/j.biombioe.2023.106820.

[157] H. Li *et al.*, "Machine learning assisted predicting and engineering specific surface area and total pore volume of biochar," *Bioresource Technology,* vol. 369, p. 128417, 2023/02/01/ 2023, doi: https://doi.org/10.1016/j.biortech.2022.128417.

[158] Y. J. Wong, S. K. Arumugasamy, C. H. Chung, A. Selvarajoo, and V. Sethu, "Comparative study of artificial neural network (ANN), adaptive neuro-fuzzy inference system (ANFIS) and multiple linear regression (MLR) for modeling of Cu (II) adsorption from aqueous solution using biochar derived from rambutan (Nephelium lappaceum) peel," *Environmental Monitoring and Assessment,* vol. 192, no. 7, p. 439, 2020/06/17 2020, doi: 10.1007/s10661-020-08268-4.

[159] M. Li *et al.*, "EDTA functionalized magnetic biochar for Pb(II) removal: Adsorption performance, mechanism and SVM model prediction," *Separation and Purification*

Technology, vol. 227, p. 115696, 2019/11/15/ 2019, doi: https://doi.org/10.1016/j.seppur.2019.115696.

[160] B. K. Nath, C. Chaliha, and E. Kalita, "Iron oxide Permeated Mesoporous rice-husk nanobiochar (IPMN) mediated removal of dissolved arsenic (As): Chemometric modelling and adsorption dynamics," *Journal of Environmental Management,* vol. 246, pp. 397-409, 2019/09/15/ 2019, doi: https://doi.org/10.1016/j.jenvman.2019.06.008.

[161] V. Chakraborty and P. Das, "Synthesis of nano-silica-coated biochar from thermal conversion of sawdust and its application for Cr removal: kinetic modelling using linear and nonlinear method and modelling using artificial neural network analysis," *Biomass Conversion and Biorefinery,* vol. 13, no. 2, pp. 821-831, 2023/01/01 2023, doi: 10.1007/s13399-020-01024-1.

[162] C. Yan, X. Wang, S. Xia, and J. Zhao, "Mechanistic insights into the removal of As(III) and As(V) by iron modified carbon based materials with the aid of machine learning," *Chemosphere,* vol. 321, p. 138125, 2023/04/01/ 2023, doi: https://doi.org/10.1016/j.chemosphere.2023.138125.

[163] X. Zhu *et al.*, "Machine learning exploration of the direct and indirect roles of Fe impregnation on Cr(VI) removal by engineered biochar," *Chemical Engineering Journal,* vol. 428, p. 131967, 2022/01/15/ 2022, doi: https://doi.org/10.1016/j.cej.2021.131967.

[164] T.-X. Da, H.-K. Ren, W.-K. He, S.-Y. Gong, and T. Chen, "Prediction of uranium adsorption capacity on biochar by machine learning methods," *Journal of Environmental Chemical Engineering,* vol. 10, no. 5, p. 108449, 2022/10/01/ 2022, doi: https://doi.org/10.1016/j.jece.2022.108449.

[165] X. Zhu, X. Wang, and Y. S. Ok, "The application of machine learning methods for prediction of metal sorption onto biochars," *Journal of Hazardous Materials,* vol. 378, p. 120727, 2019/10/15/ 2019, doi: https://doi.org/10.1016/j.jhazmat.2019.06.004.

[166] H. Zhang *et al.*, "A particle scale micro-CT approach for 3D in-situ visualizing the Pb (II) adsorption in different crop residue-derived chars," *Bioresource Technology,* vol. 344, p. 126269, 2022/01/01/ 2022, doi: https://doi.org/10.1016/j.biortech.2021.126269.

[167] F. Talebkeikhah, S. Rasam, M. Talebkeikhah, M. Torkashvand, A. Salimi, and M. K. Moraveji, "Investigation of effective processes parameters on lead (II) adsorption from wastewater by biochar in mild air oxidation pyrolysis process," *International Journal of*

Environmental Analytical Chemistry, vol. 102, no. 16, pp. 3975-3995, 2022/12/16 2022, doi: 10.1080/03067319.2020.1777291.

[168] S. Singha, S. Pasupuleti, S. S. Singha, and S. Kumar, "Effectiveness of groundwater heavy metal pollution indices studies by deep-learning," *Journal of Contaminant Hydrology,* vol. 235, p. 103718, 2020/11/01/ 2020, doi: https://doi.org/10.1016/j.jconhyd.2020.103718.

[169] B. Ke, H. Nguyen, X.-N. Bui, H.-B. Bui, and T. Nguyen-Thoi, "Prediction of the sorption efficiency of heavy metal onto biochar using a robust combination of fuzzy C-means clustering and back-propagation neural network," *Journal of Environmental Management,* vol. 293, p. 112808, 2021/09/01/ 2021, doi: https://doi.org/10.1016/j.jenvman.2021.112808.

[170] B. Ke *et al.*, "Predicting the sorption efficiency of heavy metal based on the biochar characteristics, metal sources, and environmental conditions using various novel hybrid machine learning models," *Chemosphere,* vol. 276, p. 130204, 2021/08/01/ 2021, doi: https://doi.org/10.1016/j.chemosphere.2021.130204.

[171] W. Wang, J.-S. Chang, and D.-J. Lee, "Machine learning applications for biochar studies: A mini-review," *Bioresource Technology,* vol. 394, p. 130291, 2024/02/01/ 2024, doi: https://doi.org/10.1016/j.biortech.2023.130291.

[172] S. Ascher, I. Watson, and S. You, "Machine learning methods for modelling the gasification and pyrolysis of biomass and waste," *Renewable and Sustainable Energy Reviews,* vol. 155, p. 111902, 2022/03/01/ 2022, doi: https://doi.org/10.1016/j.rser.2021.111902.

[173] M.-W. Chen, M.-S. Chang, Y. Mao, S. Hu, and C.-C. Kung, "Machine learning in the evaluation and prediction models of biochar application: A review," *Science Progress,* vol. 106, no. 1, p. 00368504221148842, 2023, doi: 10.1177/00368504221148842.

[174] J. Chen *et al.*, "The Estimation of the Higher Heating Value of Biochar by Data-Driven Modeling," *Journal of Renewable Materials,* vol. 10, no. 6, pp. 1555-1574, 2022/01/18/ 2022, doi: https://doi.org/10.32604/jrm.2022.018625.

[175] C. Gallego-Ramírez, E. Chica, and A. Rubio-Clemente, "Life Cycle Assessment of Raw and Fe-Modified Biochars: Contributing to Circular Economy," *Materials,* vol. 16, no. 17, p. 6059, 2023. [Online]. Available: https://www.mdpi.com/1996-1944/16/17/6059.

[176] J. Pryshlakivsky and C. Searcy, "Life Cycle Assessment as a decision-making tool: Practitioner and managerial considerations," *Journal of Cleaner Production,* vol. 309, p. 127344, 2021/08/01/ 2021, doi: https://doi.org/10.1016/j.jclepro.2021.127344.

[177] G. Yadav *et al.*, "Techno-economic analysis and life cycle assessment for catalytic fast pyrolysis of mixed plastic waste," *Energy & Environmental Science,* 10.1039/D3EE00749A vol. 16, no. 9, pp. 3638-3653, 2023, doi: 10.1039/D3EE00749A.

[178] R. Kumar Mishra, D. Jaya Prasanna Kumar, A. Narula, S. Minnat Chistie, and S. Ullhas Naik, "Production and beneficial impact of biochar for environmental application: A review on types of feedstocks, chemical compositions, operating parameters, techno-economic study, and life cycle assessment," *Fuel,* vol. 343, p. 127968, 2023/07/01/ 2023, doi: https://doi.org/10.1016/j.fuel.2023.127968.

[179] P. Brassard, S. Godbout, F. Pelletier, V. Raghavan, and J. H. Palacios, "Pyrolysis of switchgrass in an auger reactor for biochar production: A greenhouse gas and energy impacts assessment," *Biomass and Bioenergy,* vol. 116, pp. 99-105, 2018/09/01/ 2018, doi: https://doi.org/10.1016/j.biombioe.2018.06.007.

[180] J. Shaheen, Y. H. Fseha, and B. Sizirici, "Performance, life cycle assessment, and economic comparison between date palm waste biochar and activated carbon derived from woody biomass," *Heliyon,* vol. 8, no. 12, p. e12388, 2022/12/01/ 2022, doi: https://doi.org/10.1016/j.heliyon.2022.e12388.

[181] C. Huang, B. A. Mohamed, and L. Y. Li, "Comparative life-cycle assessment of pyrolysis processes for producing bio-oil, biochar, and activated carbon from sewage sludge," *Resources, Conservation and Recycling,* vol. 181, p. 106273, 2022/06/01/ 2022, doi: https://doi.org/10.1016/j.resconrec.2022.106273.

[182] K. Sahoo, G. L. Hawkins, X. A. Yao, K. Samples, and S. Mani, "GIS-based biomass assessment and supply logistics system for a sustainable biorefinery: A case study with cotton stalks in the Southeastern US," *Applied Energy,* vol. 182, pp. 260-273, 2016/11/15/ 2016, doi: https://doi.org/10.1016/j.apenergy.2016.08.114.

[183] K. Sahoo, S. Mani, L. Das, and P. Bettinger, "GIS-based assessment of sustainable crop residues for optimal siting of biogas plants," *Biomass and Bioenergy,* vol. 110, pp. 63-74, 2018/03/01/ 2018, doi: https://doi.org/10.1016/j.biombioe.2018.01.006.

[184] X. Chen, H. Zhang, and R. Xiao, "Mobile Autothermal Pyrolysis System for Local Biomass Conversion: Process Simulation and Techno-Economic Analysis," *Energy & Fuels,* vol. 32, no. 4, pp. 4178-4188, 2018/04/19 2018, doi: 10.1021/acs.energyfuels.7b03172.

[185] Y. Li, B. Xing, X. Wang, K. Wang, L. Zhu, and S. Wang, "Nitrogen-Doped Hierarchical Porous Biochar Derived from Corn Stalks for Phenol-Enhanced Adsorption," *Energy & Fuels,* vol. 33, no. 12, pp. 12459-12468, 2019/12/19 2019, doi: 10.1021/acs.energyfuels.9b02924.

[186] S. Liu *et al.*, "Heteroatom doping in metal-free carbonaceous materials for the enhancement of persulfate activation," *Chemical Engineering Journal,* vol. 427, p. 131655, 2022/01/01/ 2022, doi: https://doi.org/10.1016/j.cej.2021.131655.

[187] X. Qi *et al.*, "Biochar-based microbial agent reduces U and Cd accumulation in vegetables and improves rhizosphere microecology," *Journal of Hazardous Materials,* vol. 436, p. 129147, 2022/08/15/ 2022, doi: https://doi.org/10.1016/j.jhazmat.2022.129147.

[188] Y. Xia, M. Deng, T. Zhang, J. Yu, and X. Lin, "An efficient fungi-biochar-based system for advancing sustainable management of combined pollution," *Environmental Pollution,* vol. 367, p. 125649, 2025/02/15/ 2025, doi: https://doi.org/10.1016/j.envpol.2025.125649.

[189] Q. Wu *et al.*, "Adsorption characteristics of Pb(II) using biochar derived from spent mushroom substrate," *Scientific Reports,* vol. 9, no. 1, p. 15999, 2019/11/05 2019, doi: 10.1038/s41598-019-52554-2.

[190] R. Ahuja, A. Kalia, R. Sikka, and C. P, "Nano Modifications of Biochar to Enhance Heavy Metal Adsorption from Wastewaters: A Review," *ACS Omega,* vol. 7, no. 50, pp. 45825-45836, 2022/12/20 2022, doi: 10.1021/acsomega.2c05117.

[191] Y. Wang, H. Li, and S. Lin, "Advances in the Study of Heavy Metal Adsorption from Water and Soil by Modified Biochar," *Water,* vol. 14, no. 23, p. 3894, 2022. [Online]. Available: https://www.mdpi.com/2073-4441/14/23/3894.

[192] T. Wang, J. Zheng, H. Liu, Q. Peng, H. Zhou, and X. Zhang, "Adsorption characteristics and mechanisms of Pb2+ and Cd2+ by a new agricultural waste–Caragana korshinskii biomass derived biochar," *Environmental Science and Pollution Research,* vol. 28, no. 11, pp. 13800-13818, 2021/03/01 2021, doi: 10.1007/s11356-020-11571-9.

[193] L. Wang *et al.*, "Fe-biochar for simultaneous stabilization of chromium and arsenic in soil: Rational design and long-term performance," *Science of The Total Environment,* vol. 862, p. 160843, 2023/03/01/ 2023, doi: https://doi.org/10.1016/j.scitotenv.2022.160843.

[194] Z. Wang, C. Geng, Y. Bian, G. Zhang, C. Zheng, and C. An, "Effect of oxidative aging of biochar on relative distribution of competitive adsorption mechanism of Cd2+ and Pb2+," *Scientific Reports,* vol. 12, no. 1, p. 11308, 2022/07/04 2022, doi: 10.1038/s41598-022-15494-y.

[195] Z. Cui, Y. Wang, N. Wang, F. Ma, and Y. Yuan, "Effects of Ageing on Surface Properties of Biochar and Bioavailability of Heavy Metals in Soil," *Agriculture,* vol. 14, no. 9, p. 1631, 2024. [Online]. Available: https://www.mdpi.com/2077-0472/14/9/1631.

[196] H. Ashebir, S. Tibebu, D. Bedada, J. Fito, E. Kassahun, and A. Worku, "Advanced methylene blue adsorption with a tailored biochar/graphene oxide/magnetite nanocomposite: characterization, optimization, and reusability," *Biomass Conversion and Biorefinery,* 2024/11/01 2024, doi: 10.1007/s13399-024-06288-5.

[197] S. Sudan, J. Kaushal, and A. Khajuria, "Efficient adsorption of anionic dye (congo red) using copper-carbon dots doped magnetic biochar: kinetic, isothermal, and regeneration studies," *Clean Technologies and Environmental Policy,* vol. 26, no. 2, pp. 481-497, 2024.

Chapter 3 Efficient iron anchoring strategy for magnetic biochar synthesis: Material characteristics and functional mechanism in dye removal

Abstract

Magnetic biochar (MBC) is a novel bio-metallic composite material with high potential in sustainable water cleaning. Iron anchoring is a critical step in forming MBC and will fundamentally impact its characteristics and functionality in dye removal applications. However, the mechanism is not well-revealed. To understand the iron anchoring mechanism and to identify the most efficient, this study investigates three methods for preparing MBC, including impregnation pyrolysis, post-treatment with Fe salts, and one-step co-pyrolysis. The MBC is synthesized from maple wood and different types of Fe-containing chemicals, including FeO, $FeSO_4$, and $FeCl_3$, and the products are characterized comprehensively and evaluated for the adsorption of Remazol Brilliant Blue R (RBBR) dye. Key results indicate that the one-step co-pyrolysis method yields the highest adsorption efficiency, with BC produced at 700 °C exhibiting optimal performance. The adsorption capacity of RBBR dye was found to be highest at acidic pH levels, with the 1:1 FeO to biomass ratio achieving a removal efficiency of 100% at a dosage of 0.4 g. Kinetic studies revealed that the adsorption process follows a pseudo-second-order model, suggesting chemisorption as the primary mechanism. Isotherm analysis indicated that the *Langmuir* model best describes the adsorption process, with a maximum adsorption capacity of 11.33 mg/g. This study provides new insights into the design and optimization of MBC synthesis for environmental applications, which could help address growing concerns about water pollution.

*Chapter 3 is submitted for publication in a peer-reviewed journal

3.1. Introduction

Water pollution remediation has long been a research hot spot. In recent years, rapid industrialization has led to an alarming increase in the generation of wastewater containing synthetic dyes. The global production of dye exceeds 1,000,000 tons annually due to the increasing consumption of dyes in various industries, including textiles, tanneries, food, cosmetics, and medicine manufacturing [1]. Remazol Brilliant Blue R (RBBR), an anthraquinone-based reactive dye, is extensively used in textile industries due to its vibrant color. Its discharge into water bodies poses severe environmental and health risks, such as chronic toxicity, surface water discoloration, sunlight disruption, complex treatment, oxygen depletion, metal ion toxicity, and eutrophication [2]. Many methods have been developed to treat dye-containing wastewater, such as coagulation and flocculation, etc. [3-5]. However, most of the existing methods are either consuming expensive chemical reagents or have the problem of high energy consumption [6, 7]. Therefore, developing innovative processes that use waste-derived materials and consume less energy to remove dyes is critical.

Adsorption is a promising approach for dye removal from wastewater due to its process simplicity, cost-effectiveness, and high efficiency [7]. Recently, biochar (BC) emerged as an environmentally friendly adsorbent and has gained significant attention due to its cost-effectiveness and good adsorption properties. BC is a carbon-rich porous material that can be produced from many biomass resources, such as wood, agricultural residues, or organic bio-waste, through pyrolysis. Traditionally, BC is produced using woody biomass. However, conventional woody biomass-based BC is very challenging to recycle and reuse, hindering its usability in wastewater treatment. In this regard, incorporating magnetic properties into BC to produce magnetic biochar (MBC) can significantly enhance its recoverability and reusability, further improving its practical applicability in wastewater treatment processes. Specifically, MBC, as a novel type of biomass-based adsorbent, shows high potential for repeatable application, further reducing the quantity required for water cleanup and preventing secondary pollution caused by the dispersion of polluted BC into natural water reservoirs [8].

Though good progress has been made in using MBC for adsorptive water decontamination, there is a need for more understanding of several critical issues in this field. First, the optimal method for incorporating Fe-containing species into MBC has not been determined. Specifically, it remains unclear whether iron should be impregnated into the biomass before pyrolysis or applied to the BC post-pyrolysis, as these two approaches could lead to varying degrees of adsorption capacity and magnetic properties. Additionally, the influence of different preparation methods on the adsorption efficiency and magnetic performance of the resulting MBC has yet to be systematically studied [8]. Lastly, there is a need to study whether a simplified, one-step co-pyrolysis process can produce MBC with performance characteristics comparable to or superior to those achieved through more complex multi-step approaches, providing more efficient and scalable production. Moreover, there is limited information on how the physicochemical properties of MBC influence its adsorption reaction mechanisms.

To answer the above questions, this study aims to bridge these knowledge gaps by systematically investigating the material characteristics and functioning mechanisms of MBC, with a particular focus on comparing their physicochemical properties resulting from different iron anchoring procedures. By conducting comprehensive analyses, this research will provide new insights into the factors affecting MBC's characteristics and adsorption functionality, identify the most efficient and practical iron anchoring approach, and thus provide valuable information for optimizing the design of MBC for environmental applications.

3.2. Materials and methods

3.2.1. Materials

Maple wood (MW) chips were obtained from local supply stores in Thunder Bay, Ontario, Canada, and were used as the biomass feedstock for MBC production. Ferrous sulfate ($FeSO_4 \cdot 7H_2O$, ≥99.0%), ferric chloride ($FeCl_3$, ≥97.0%), ferrous oxide (FeO, ≥99.6%), RBBR dye ($C_{22}H_{16}N_2Na_2O_{11}S_3$, dye content ~60%), hydrochloric acid (HCl, 36.5% solution), and sodium hydroxide (NaOH, ≥99.99%) were purchased from Sigma-Aldrich. Deionized (DI) water from Nanopure Water, Barnstead, was used for cleaning, rinsing, diluting, and preparing the stock solutions. The compressed N_2 gas used for the char preparation was purchased from Linde Canada Inc.

3.2.2. Preparation of the adsorbents

The raw MW chips were washed thoroughly with DI water and rinsed repeatedly until the wash water ran clear. They were dried in a constant temperature oven (Model: DKN812, Yamato Scientific) for 48 hours at 105 °C. The MX chips were downsized using a blade grinder before use.

As illustrated in **Figure 3.1**, three different methods were used to prepare MBC, including impregnation-pyrolysis (Method 1), post-treatment of BC with Fe salts (Method 2), and direct one-step co-pyrolysis of MW with FeO (Method 3). For the first method, MW chips were impregnated with a mixture of 1M $FeSO_4$ and $FeCl_3$ solution for 4 hours under constant stirring at room temperature. For the second method, BC was first produced from the pyrolysis of MW. Then, the BC was impregnated with 1M Fe salts, followed by secondary thermal treatment to produce MBC. For the third method, the MBC was prepared by the co-pyrolysis of the FeO and MW mixture. The FeO and MW chips were first mixed in different ratios, such as 1:1 and 1:2 (FeO: MW), to create a mixture of raw materials of 30 grams. For example, 10 grams of FeO were mixed with 20 grams of MW chips to produce MBC at a 1:2 ratio to make a mixture of 30 g. For all the methods, the samples were placed in ceramic boats, loaded into a tube furnace (STF1200-60X1000, Across International, Nevada, USA), and heated to 500 to 900 °C with a constant flow of N_2 at 250 mL/min. The ramping rate was 10 °C/min, and the residence time was 3 hours. The N_2 flow continued as the furnace cooled to room temperature before removing the char sample. The pyrolysis conditions for untreated MW chips to produce pristine BC were the same as earlier. Afterward, the samples were rinsed multiple times with DI water to remove surface-attached impurities. The samples were then oven-dried at 105 °C for 12 hours and stored in a container for further characterization. The adsorbents were named "X:Y-MBC, pyrolysis temperature (°C)," where "X:Y" is the ratio of FeO to MW. For example, "1:2-MBC700″ denotes that the adsorbent is prepared by co-pyrolysis of a 1:2 mass ratio of FeO and MW at 700 °C.

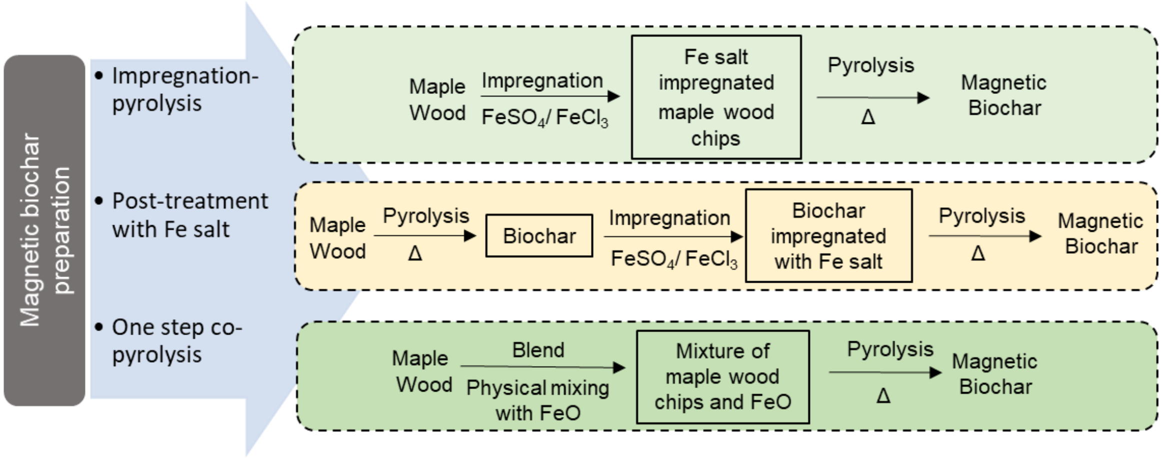

Figure 3.1 Illustration of different preparation procedures of MBC used in this study

3.2.3. Characterization methods

Elemental composition (C, H, N, S) was analyzed using a Vario EL Cube elemental analyzer, and proximate analysis (moisture, volatile matter, ash) followed ASTM 2019 standards using a Thermolyne muffle furnace (FB1415M, Thermo Scientific, Asheville, USA). Surface morphology and elemental distribution were examined using SEM-EDS (Hitachi SU-70 Schottky Field Emission SEM, Hitachi, Japan). Functional groups were identified using FTIR (Bruker Tensor 37 with ATR), and crystal structures were analyzed via XRD (PANalytical X'pert Pro) using Cu Kα radiation. XPS (Kratos AXIS Supra, Japan) was used for surface chemical state analysis, and data were processed using ESCApe software. Surface area and porosity were evaluated using N_2 adsorption-desorption isotherms (BET method) with a Quantachrome NOVA 2200E after degassing the samples at 150 °C for 4 hours.

3.2.4. Magnetic strength test

The magnetic strength of the MBC samples was tested using an "Electricity and Magnetism Kit" by EUDAX (Shenzhen Tianzhiyi Trading Co., Ltd). It was operated at an electric current of 0.5 A. First, the electromagnet was activated and kept on for 2 minutes. Then, each 0.1 g sample of MBC was placed under the electromagnet. The electromagnet hovered over the MBC samples at a controlled height of 2 mm for 1 minute. Then, the sample attached to the device was detached and weighed, and the lifting capacity of the electromagnet was recorded for each sample. The separation efficiency was calculated based on how much the electromagnet could lift the sample. The efficiency was calculated using **Equation (3.1)**.

$$Magnetic\ seperation\ efficiency = \frac{Mass\ of\ seperated\ MBC}{Initial\ mass\ of\ MBC} \times 100 \qquad (3.1)$$

3.2.5. Adsorption capacity, kinetic, and isotherm experiments

The batch adsorption experiment was used to assess the adsorption capacity, thermodynamic, and kinetic properties of the MBC. Briefly, for each test, in 50 mL tubes, 30 mL of various concentrations of RBBR dye and different adsorbent doses were mixed. The adsorption experiments utilized various pH values (3, 5, 7, 9, and 11). 0.1 M HCl or 0.1 M NaOH was used to adjust the sample pH to the required values. The mixtures were shaken at 300 rpm using a shaker (Excella E5, New Brunswick Scientific, Edison, New Jersey, USA) for 2 hours. After that, the tubes were removed from the shaker, and the mixtures were filtered using nylon syringe filters of 0.2 µm pore size (Sartorius, CA-based). The RBBR dye concentrations in the liquid phase samples were determined using a UV-visible spectrophotometer (Varian Cary 50 Bio UV Visible Spectrophotometer, Santa Clara, CA, USA). Spectrophotometry at λ_{max} 593 nm was used to assess the amount of RBBR dye in the solution. The samples were analyzed three times each, and the average absorbance from those measurements was used. The adsorption capacities of RBBR dye at equilibrium (q_e) were calculated based on **Equation (3.2)**.

$$q_e = \frac{C_o - C_e}{W} \times \mathrm{V} \tag{3.2}$$

Here, C_o and C_e (mg/L) stand for the initial and final dye concentrations in the liquid phase, respectively; V denotes the volume of the solution (L), and W represents the MBC mass in grams.

Adsorption kinetics of RBBR dye on MBC were examined using an initial RBBR dye concentration of 100 mg/L and contact times ranging from 5 minutes to 4 hours. The initial solution was adjusted to pH 3, the optimum condition. Various models were utilized to analyze the adsorption kinetics, including pseudo-first-order, pseudo-second-order, Intraparticle diffusion model (IPDM), and Film diffusion model (FDM). The corresponding equations for these models are presented below, as **Equations (3.3 - 3.6)** [9-12].

Pseudo-first-order kinetic model:

$$\ln(q_e - q_t) = ln q_e - k_1 t \tag{3.3}$$

Pseudo-second-order kinetic model:

$$\frac{t}{q} = \frac{1}{k_2 q_e^2} + \frac{t}{q_e} \tag{3.4}$$

Intraparticle diffusion model (IPDM):

$$q_t = k_i t^{\frac{1}{2}} + C \tag{3.5}$$

Film diffusion model:

$$\ln(1 - F) = -k_f t \tag{3.6}$$

Where q_t = amount of adsorbate adsorbed at time t (mg/g), q_e = Amount of adsorbate adsorbed at equilibrium (mg/g), k_1 = Rate constant, t = Contact time (min). k_2 = Rate constant of the pseudo-second-order q_t = Amount of adsorbate adsorbed at time t (mg/g), k_i = Intraparticle diffusion rate constant, t = Contact time (min), C = Intercept, which indicates the boundary layer effect F = Fractional attainment of equilibrium (F = q_t/q_e), k_f = Film diffusion rate constant, t = Contact time (min).

In isotherm experiments, the initial concentrations of RBBR dye ranged from 100 to 500 mg/L for 24 hours. The *Langmuir*, *Freundlich*, and *Temkin* adsorption isotherm models were employed to fit the data from the adsorption isotherms. The equations for these models are provided below as **Equations 3.7**, **3.8**, and **3.9**, respectively [13-15].

Langmuir isotherm model:

$$\frac{C_e}{q_e} = \frac{1}{q_m K_L} + \frac{C_e}{q_m} \tag{3.7}$$

Freundlich isotherm model:

$$ln q_e = ln\, K_F + \frac{1}{n}\, ln\, C_e \tag{3.8}$$

Temkin isotherm model:

$$q_e = B\, ln\, C_e + B\, ln\, A \tag{3.9}$$

Where q_e = Amount of adsorbate adsorbed (mg/g), q_m = Maximum adsorption capacity (mg/g), K_L = *Langmuir* constant (L/mg), C_e = Equilibrium concentration (mg/L), K_F = *Freundlich* constant, n = Heterogeneity factor. A = *Temkin* isotherm constant (L/g), B = Constant related to the heat of adsorption (J/mol).

3.2.6. Statistical analysis

Statistical analysis of the factors, including different FeO to biomass ratio, dosage, contact time, and pH was performed by two-way ANOVA using Microsoft Excel.

3.3. Results and discussions

3.3.1. Characterization

Effect of preparation method on biochar yield and performance

The influence of different preparation methods and pyrolysis temperatures on the physicochemical properties and adsorption capabilities of MBC is demonstrated in **Fig. A3.1**. Char produced using method 1 exhibited relatively lower dye removal efficiency than the other two methods. This could be attributed to the limited activation of the MBC surface due to insufficient impregnation of iron salts and pyrolysis, which results in a less developed porous structure and fewer active sites for adsorption. Additionally, the high temperatures involved in pyrolysis may cause the decomposition of functional groups. On the other hand, methods 2 and 3 demonstrated comparable performance in RBBR dye removal. However, the MBC produced via the direct co-pyrolysis method (method 3) exhibited marginally better efficiency compared to method 2. This improved removal efficiency is likely due to better mixing of FeO with the biomass, which creates more active sites for adsorption. The presence of FeO during co-pyrolysis can act as a catalyst, catalyzing the formation of the carbon matrix and facilitating the protection of functional groups like hydroxyl (-OH) and carboxyl (-COOH) from excessive decomposition. As a result, more adsorption sites are preserved compared to post-treatment methods.

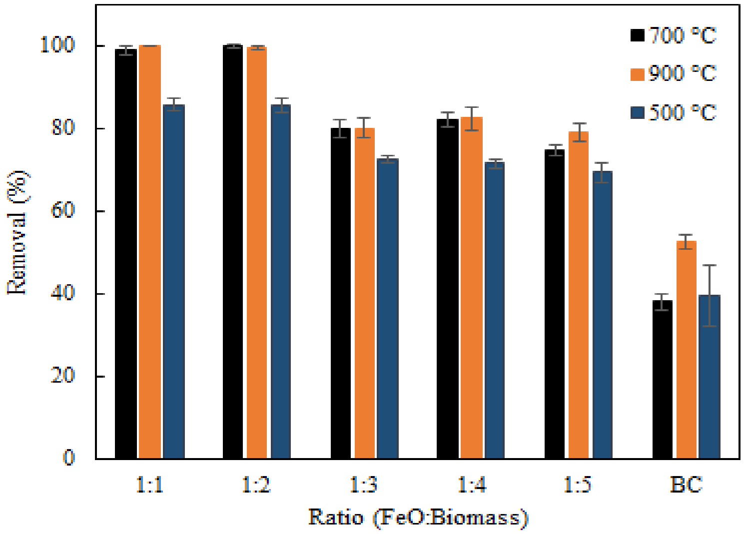

Figure 3.2 Effect of pyrolysis temperatures, FeO-to-biomass ratio, on RBBR dye removal efficiency on RBBR dye removal efficiency

Fig. 3.2 illustrates the influence of pyrolysis temperature (500 °C, 700 °C, and 900 °C) on the properties and adsorption performance of MBC. Samples produced at 700 °C and 900 °C exhibited comparable dye removal efficiency, while those prepared at 500 °C showed significantly lower performance. The comparable adsorption performance at 700 °C and 900 °C suggests that key structural and chemical properties necessary for dye adsorption were already developed at 700 °C, with minimal improvement at higher temperatures. Selvarajoo et al. [16] reported that BC produced at 700 °C and 900 °C exhibited similar carbon conversion rates and reduced volatile matter content compared to those produced at lower temperatures. These findings indicate comparable characteristics, such as reactivity and surface properties, between the two higher-temperature BCs. Given the similar adsorption performance but lower energy input at 700 °C, this temperature was selected as the optimal condition for later experiments.

Basic properties of the adsorbents

Table A3.1 presents the proximate analysis of MW and its MBC derivatives, prepared with varying Mw to FeO ratios. All samples showed low moisture content, with 1:1-MBC700 showing the lowest value (0.78 ± 0.16%), indicating efficient water removal during pyrolysis. This low moisture content in MW can be attributed to their naturally lower initial water content, as hardwoods like maple typically retain less moisture compared to softwoods [17]. MW exhibited high volatile matter (VM) content (85.36 ± 0.48%) due to its organic constituents (cellulose, hemicellulose, lignin). In contrast, MBC samples showed significantly reduced VM, as pyrolysis and the catalytic effect of Fe enhanced thermal decomposition and promoted carbon formation at lower temperatures [18]. Interestingly, higher biomass-to-FeO ratios increase VM content, as reduced FeO content limits catalytic effects, allowing greater retention of volatiles. Ash content also differs notably between samples. Raw MW has very low ash content due to its minimal inorganic components as a woody material. By contrast, MBC samples have higher ash levels, particularly those with higher FeO content. For instance, 1:1-MBC700 exhibited 85.08 ± 0.50% ash, compared to 44.45 ± 0.14% in 1:5-MBC700. This difference is attributed to the higher Fe content in 1:1-MBC700, which increases the inorganic fraction remaining after pyrolysis, thereby raising the ash content [19]. Increasing the FeO ratio in MBC significantly alters the proximate characteristics, enhancing thermal decomposition and increasing the ash content due to the higher inorganic load.

The physicochemical properties of the adsorbents are shown in **Table 3.1**. Initially, the char yield from co-pyrolysis across all ratios exceeds that of the standard BC sample (22.8 %). A notable trend observed among the MBC is that higher FeO to MW ratios result in increased yield, with the 1:1-MBC700 achieving the highest yield of 57.35 %. This trend is consistent with findings from other studies [20]. This trend is attributed to the addition of Fe, which will not decompose and lose weight during the pyrolysis process, unlike biomass [21].

BET analysis

BET analysis results for raw MW, BC700, and MBC samples are presented in **Table 3.1**. BC700 showed a surface area of 109 m^2/g, pore volume of 0.953 cm^3/g, and a pore diameter of 13.82 Å, indicating a well-developed porous structure suitable for adsorption. Compared to BC700, all MBC samples exhibited lower surface areas due to iron loading. The 1:1-MBC700 had a surface area of 83.37 m^2/g, showing a 23.5% reduction, while 1:2-MBC700 and 1:5-MBC700 had slightly higher values of 87.69 and 86.97 m^2/g, respectively. This reduction is likely due to iron oxide particles blocking some of the pores. In terms of pore volume, MBC samples (0.945–0.952 cm^3/g) remained quite similar to BC700, suggesting that the overall porous structure was mostly retained despite the drop in surface area. However, the average pore diameter significantly decreased in MBCs (1.30–1.35 Å), compared to 13.82 Å in BC700, likely due to partial pore blockage or narrowing caused by iron deposition. This shift toward smaller pores could influence the accessibility and diffusion of larger adsorbate molecules.

Table 3.1 Yield%, surface area, pore volume, and elemental analysis of the adsorbents

Sample name	**Yield (%)**	**Surface area (m^2/g)**	**Average pore volume (cm^3/g)**	**Average pore diameter (Å)**	**N%**	**C%**	**H%**	**S%**	**H/C molar ratio**
MW	-	-	-	-	16.24	47.54	3.4	0.069	0.86
BC700	22.8	109	0.953	13.82	0.37	90.42	2.78	0.082	0.37
1:1-MBC700	57.35	83.37	0.947	1.3	0.09	16.85	2.3	0.129	1.64
1:2-MBC700	43.75	87.69	0.952	1.32	0.13	29.79	2.14	0.109	0.86
1:5-MBC700	34.94	86.97	0.945	1.35	0.21	48.87	1.9	0.112	0.47

Surface morphology

Figure 3.3 shows the structural and morphological differences between BC700 and 1:2-MBC700. The SEM image of BC700 (**Figure 3.3a**) displays a highly porous structure with a rough surface, formed due to the pyrolysis of biomass. EDS analysis confirmed carbon as the major element, along with traces of O, Ca, and K, typical of biomass-derived BC. Compared to BC700, 1:2-MBC700 (**Figure 3.3b** and **3.3c**) retained a similar porous framework but showed increased surface roughness and a higher pore density. These changes are likely due to the incorporation of

Fe particles during co-pyrolysis. EDS analysis confirmed the presence of iron in the MBC sample, indicating successful magnetic modification. The deposition of iron oxides also helps explain the reduced surface area observed in BET analysis, likely due to partial pore blockage.

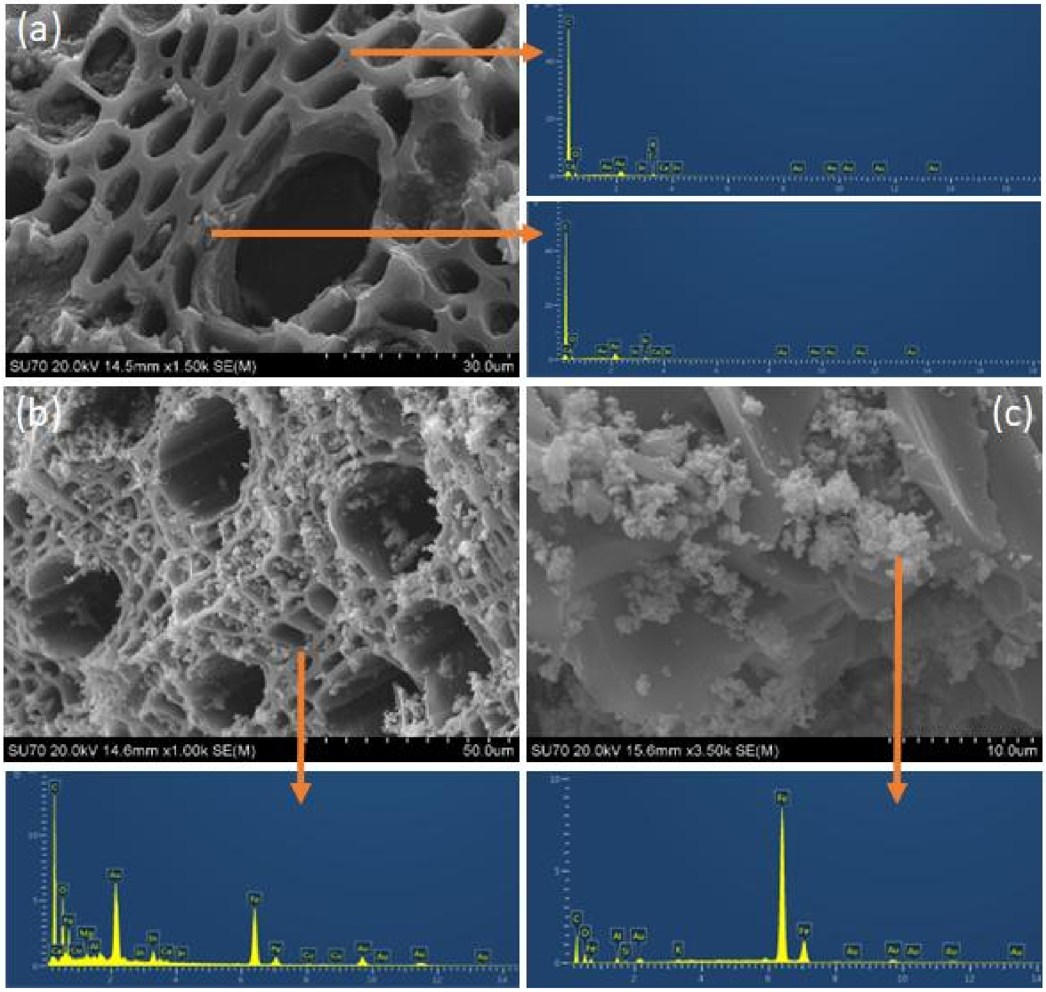

Figure 3.3 SEM images of (a) BC700 in 1.50k magnification, (b) 1:2-MBC700 in 1k magnification, and (c) 1:2-MBC700 in 3.50k magnification

FTIR analysis

The FTIR spectra of MW, BC700, 1:1-MBC700, 1:2-MBC700, and 1:5-MBC700 are presented in **Figure 3.4**. O-H stretching vibrations of hydroxyl groups in cellulose and lignin are observed as a broad peak at 3369 cm^{-1} [22]. A small peak at 2883 cm^{-1} corresponds to the asymmetric stretching vibration of C-H bonds in aliphatic hydrocarbons [23]. Aliphatic hydrocarbons consist of linear or branched chains of carbon atoms bonded to hydrogen atoms. A peak at 1724 cm^{-1} indicates carbonyl (C=O) stretching vibrations due to carboxylic acid groups and C-O stretching vibrations in ester groups [24]. A prominent peak at approximately 1593 cm^{-1} indicates aromatic C=C bonds in lignin structures [25]. A sharp peak at around 1032 cm^{-1} corresponds to C-O stretching vibrations in cellulose and hemicellulose components [26]. Upon pyrolysis, BC and MBC samples exhibited notable changes in their FTIR spectra compared to raw MW. While many of the peaks observed in the raw wood spectrum were not seen in pyrolyzed samples, indicating the degradation of major functional groups. In particular, a small peak was observed in all samples around 3884-3890 cm^{-1}, corresponding to the stretching vibrations of O-H bonds [27]. This peak suggests the presence of -OH groups on the adsorbent surfaces, possibly originating from the decomposition of cellulose and hemicellulose components during pyrolysis. In the case of the MBC samples, distinct peaks were observed around 1510-1514 cm^{-1} and at 903 cm^{-1}. These peaks may be attributed to aromatic C=C bonds and Fe-O stretching vibrations, respectively [28]. The appearance of these peaks suggests the successful incorporation of FeO nanoparticles into the BC matrix during co-pyrolysis. This also introduces additional active sites, potentially improving adsorption mechanisms through increased electrostatic interactions, metal ion coordination, and complexation [29]. These FeO nanoparticles can introduce O-H, iron-bound functional groups, which can enhance interactions with RBBR through mechanisms like hydrogen bonding, electrostatic interactions, and complexation, thereby improving the adsorption capacity [30].

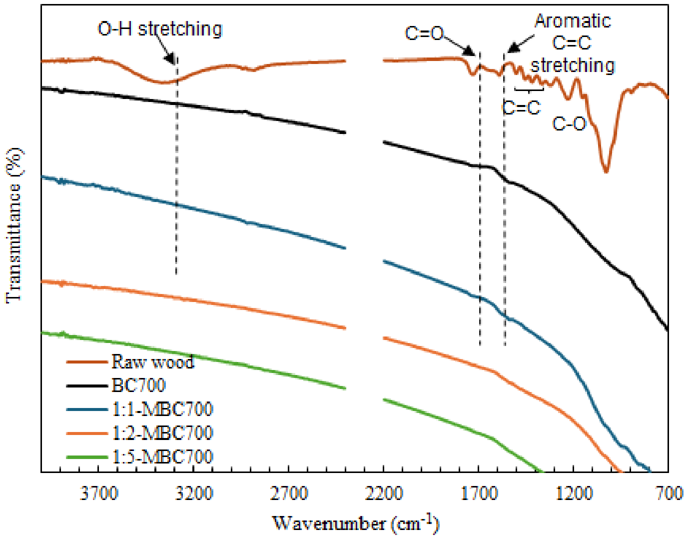

Figure 3.4 FTIR spectra of Raw wood (MW), BC700, 1:1-MBC700, 1:2-MBC700, and 1:5-MBC700

XRD analysis

XRD spectra in **Figure 3.5** display distinct peaks, indicating variations in their crystalline structures and phase compositions. MW showed a distinct peak at approximately 22.5°, indicating variations in their crystalline structures and phase compositions. MW showed a distinct peak at approximately 22.5°, indicating the presence of cellulose crystalline structures characteristic of lignocellulosic materials [31]. Upon pyrolysis, the XRD spectrum of BC700 exhibited a small bump at around 22.4°, suggesting the retention of cellulose crystalline structures in the BC matrix. Another slight bump was observed at 44.3°, indicating the (crystal plane of graphite-like structure) amorphous carbonaceous phase resulting from the thermal decomposition of lignin and other organic components. In contrast, the XRD spectra of 1:1-MBC700, 1:2-MBC700, and 1:5-MBC700 revealed notable differences. 1:1-MBC700 exhibited a peak at 30°, which resembles the characteristic of diffraction patterns of Fe_3O_4 or Fe_2O_3, indicating the presence of these iron oxide phases [32]. All the MBC samples showed diffraction peaks at around ~36°, indicating Fe_3O_4, confirming the presence of iron oxide phases [32]. Increasing FeO content in the MBC samples results in sharper, more defined peaks in that region. The peak at approximately 44.5°, associated with the Fe^0 (110) plane, indicates the crystal structures of α-Fe_2O_3 and γ-Fe_2O_3 [33]. In the MBC samples, peaks near 63° and 65° indicate the presence of iron oxide phases, such as Fe_3O_4 and Fe_2O_3 [34, 35]. These peaks suggest the successful incorporation of FeO nanoparticles into the BC matrix during co-pyrolysis, forming MBC. Furthermore, the MBC samples exhibited a small peak at around ~82.4°, which could be attributed to magnetite nanoparticles with a preferred orientation along the (311) crystallographic plane [20].

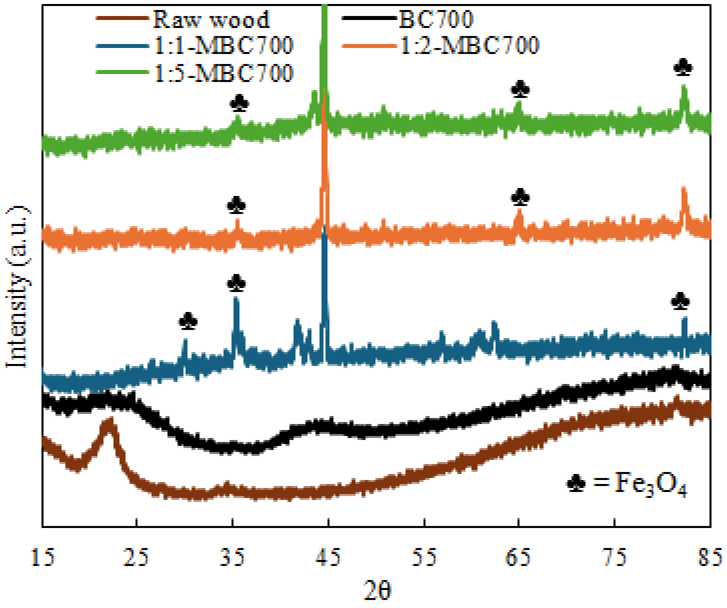

Figure 3.5 XRD spectra of Raw wood (MW), BC700, 1:1-MBC700, 1:2-MBC700, and 1:5-MBC700

XPS analysis

XPS analysis (**Figure 3.6**) shows the valence states and chemical compositions of 1:2-MBC700, 1:5-MBC700, and BC700 samples. In **Figure 3.6(a)**, the wide XPS spectra identified carbon (C 1s) and oxygen (O 1s) as the primary elements in both BC and MBC samples, while Fe 2p was the distinct feature for the MBC samples only. In **Figure 3.6(b)**, the O 1s spectra of both samples showed peaks in three regions. These O species include O in C=O at around (530.2 ~ 531.7 eV), suggesting the presence of carbonyl groups (C=O) [36] and O-C=O/C-OH at around (532.3 ~ 533 eV) [37]. The Fe 2p spectra shown in **Fig. 3.6(c)** provide insights into the iron species present in the MBC samples. The MBC sample showed Fe $2p_{3/2}$ and Fe $2p_{1/2}$ peaks at around (710.6 ~ 710.9 eV) and around (724.1 ~ 724.4 eV) due to the presence of Fe(II) and Fe(III) states of iron in Fe_3O_4 molecule [38, 39]. These binding energies indicate the presence of Fe_3O_4, confirming the MBC's magnetic properties [40]. Some satellite peaks are also at around ~728.1 eV, indicating the Fe^{3+} state [41, 42]. In **Fig. 3.6(d)**, the C 1s peak for BC showed three peaks, whereas the C 1s peak for MBC showed six distinct components. Those peaks can be fitted into these components: C-C/C=C (graphitic carbon) bonds near 284.6 eV ~ 284.7 eV, which indicates the presence of aromatic carbon structures [43], C-O bond near 285.5 ~ 286.1 eV, suggesting hydroxyl (-OH) functionalities on the surface [44], C-O or O-C=O bonds near 287.2 ~ 289.1 eV, marking the presence of carboxyl (-COOH) groups that contribute to the surface's acidic sites [37]. The metal-carbide bonds were only observed in the MBC samples at around 281.3 ~ 282.2 eV, signifying interactions between metal components and the carbon matrix [45].

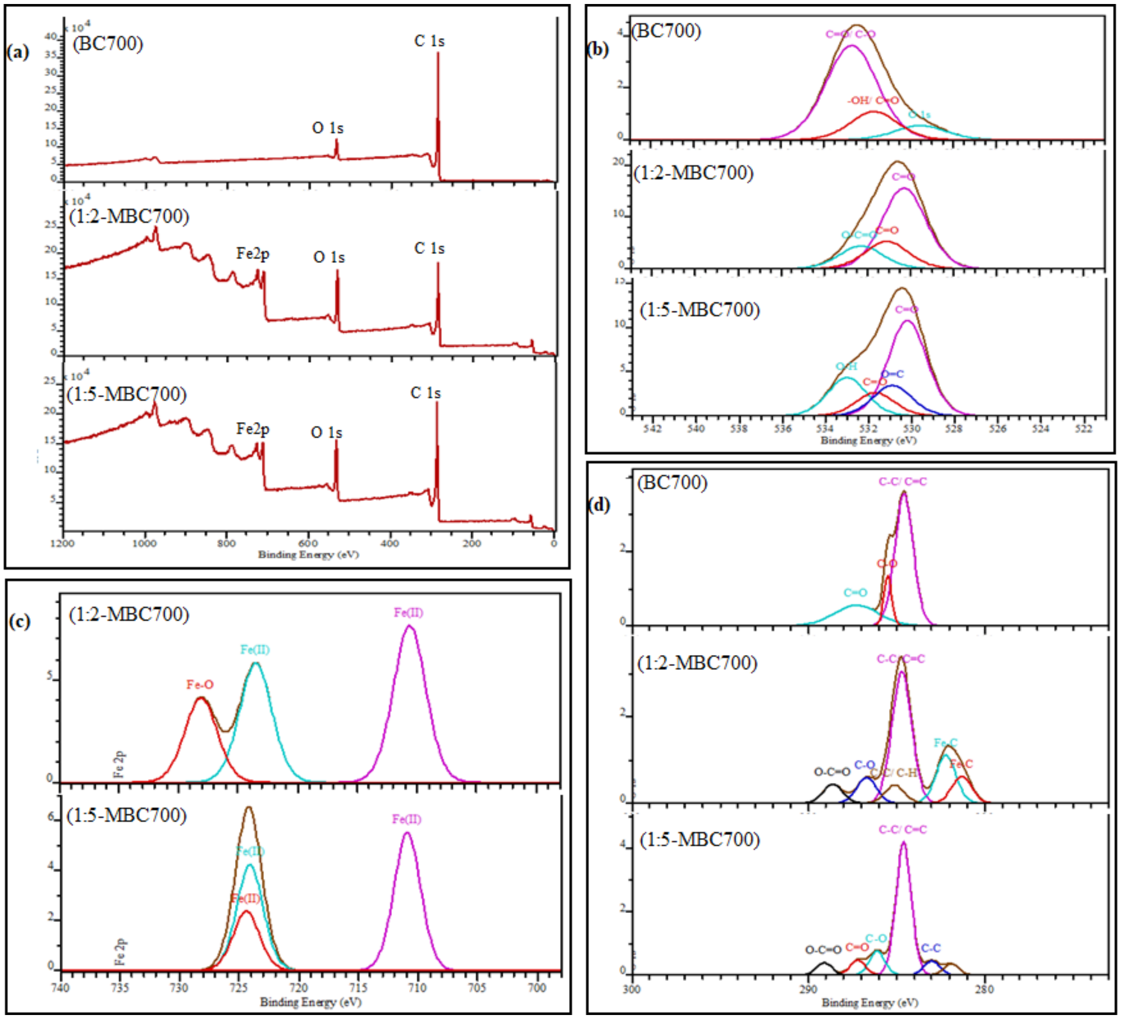

Figure 3.6 XPS spectra of BC700, 1:2-MBC700, and 1:5-MBC700 samples: (a) wide scan, (b) O 1s, (c) Fe2p, and (d) C 1s region

Magnetic strength test

Figure A3.2 shows a clear correlation between FeO content and magnetic separation efficiency. Samples with higher FeO content, like 1:1-MBC700 and 1:2-MBC700, demonstrated the strongest magnetic response and lifting capacity under an electromagnet, due to better alignment of magnetic particles. Preparation temperature also played a key role. MBC produced at 900 °C showed the highest separation efficiency, followed by those at 700 °C and 500 °C. At 900 °C, enhanced thermal decomposition promotes the formation of highly crystalline Fe_3O_4 and Fe_2O_3, improving magnetic strength. MBC prepared at 700 °C also showed good magnetic behavior, with XRD confirming Fe_3O_4 and FeO phases and XPS indicating both Fe^{3+} and Fe^{2+} states. In contrast, MBC synthesized at 500 °C likely had incomplete formation of iron oxide phases, resulting in weaker magnetism.

3.3.2. Adsorption studies

Impact of adsorbent dosage

As shown in **Figure 3.7**, dye removal efficiency increased with adsorbent dosage for all samples. MW had the lowest performance (29 ± 1.33%) due to its unmodified porous structure, while BC700 showed improved efficiency, reaching 55.75 ± 1.56% at 1 g. All MBCs outperformed BC700, particularly 1:1-MBC700 and 1:2-MBC700, showing a similar trend, achieving 98.71 ± 1.13% and 96.06 ± 1.38% removal at 0.4 g, respectively, both finally reaching 100% removal at 1 g. This superior performance is likely due to the higher FeO content, which increased surface functional groups and active sites [46]. XPS analysis confirmed more -OH and C=O groups, while XRD detected FeO crystalline phases that enhance surface heterogeneity and adsorption. On the other hand, the MBCs with high biomass content (1:3-MBC700 to 1:5-MBC700) showed a similar trend with a relatively lower adsorption efficiency compared to the high Fe-containing MBCs due to fewer magnetic nanoparticles and reduced surface activity. The regression analysis (**Table A3.2**) showed a strong fit ($R^2 = 0.805$), indicating that FeO content, MW proportion, and adsorbent dosage explain over 80% of the variation in dye removal. Adsorbent dosage (X3) had the most significant positive impact (coefficient = 63.85, $p < 0.001$), followed by FeO content (X1) (coefficient = 44.60, $p < 0.001$). In contrast, MW content (X2) had a negative effect (coefficient = -4.79, $p = 0.005$), likely due to dilution of active sites. These results highlight the importance of maximizing FeO loading and dosage while limiting unmodified biomass to enhance adsorption efficiency.

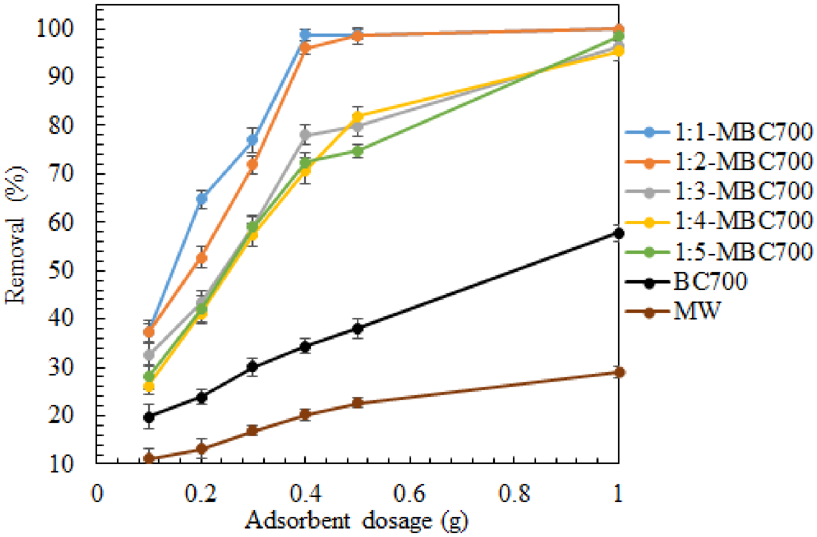

Figure 3.7 Impact of adsorbent dosage on RBBR adsorption efficiency (pH: 7; dye concentration: 100 ppm, shaking time: 2 hours)

Impact of contact time

As presented in **Figure 3.8**, all samples showed increasing dye removal with time, eventually reaching equilibrium. 1:1-MBC700 showed rapid adsorption compared to others, reaching equilibrium in less than 5 minutes of contact time. On the other hand, 1:2-MBC700 took around 120 minutes to reach equilibrium. In the initial phase, all the adsorbents exhibited rapid dye adsorption, with a significant portion of the RBBR dye being removed within the first 30 minutes. This is due to the abundant active sites on the surface, allowing for swift interaction with adsorbate molecules. During the initial stages of adsorption (from 0 to 30 minutes), MBC exhibits a substantial available surface area, leading to a rapid biosorption rate [47]. Then, the removal efficiency slowed down over 30 to 300 minutes. This is because, during this period, the saturation of active sites may occur, limiting further adsorption. After 300 minutes, equilibrium is reached, where the adsorption rate equals the desorption rate, and the dye removal efficiency stabilizes. This trend is further supported by the regression analysis (**Table A3.3**), which shows that FeO content and contact time significantly enhance dye removal ($p < 0.001$), while higher maple wood content negatively affects it. The high R^2 value (0.897) confirms that these factors strongly influence adsorption efficiency, consistent with the observed rapid initial uptake and eventual equilibrium.

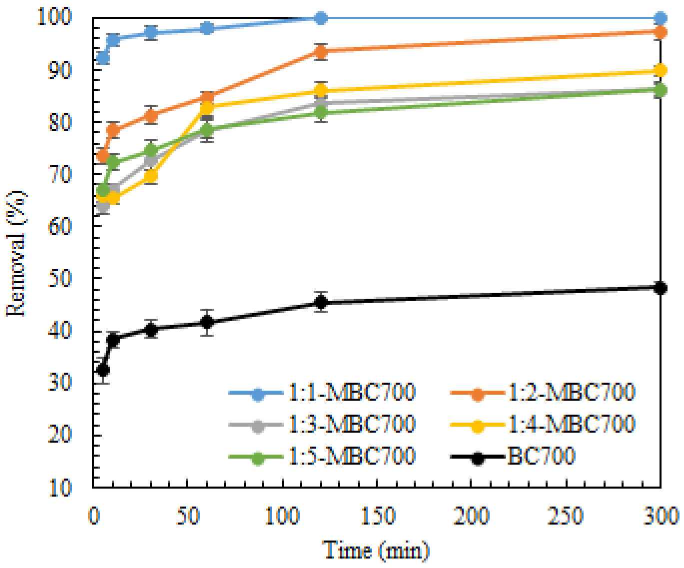

Figure 3.8 Effect of contact time on RBBR adsorption efficiency

Effect of pH

Figure 3.9 shows the effect of pH on the adsorption of RBBR dye by MBC, BC, and MW, which was used as a blank control. All adsorbents exhibit a consistent trend, especially all the magnetic adsorbents, showing more than 97% removal efficiency at pH 3. However, as the solution pH increased, a decrease in the removal efficiency for all adsorbents was observed. The decrease in removal efficiency with increasing pH for the adsorption of RBBR dye by MBC can be attributed to several factors. At lower pH levels, the surface of the MBC becomes positively charged, and the dye molecules may carry a negative charge, facilitating electrostatic attraction and enhancing adsorption [48]. However, as the pH rises, the surface of the MBC becomes more negatively charged due to the deprotonation of acidic functional groups present on the MBC surface. High pH also deprotonates RBBR molecules in the presence of excess OH^- ions, increasing their negative charge. This, coupled with negatively charged dye molecules, decreases the adsorption efficiency [49]. A multiple linear regression analysis was conducted (**Table A3.4**) to statistically evaluate the effect of pH on dye removal. The model exhibits a high coefficient of determination ($R^2 = 0.906$), indicating that the included variables can explain 90.6% of the variation in dye removal. Notably, pH (X Variable 3) shows a statistically significant negative coefficient (–1.514, $p = 0.001$), meaning that dye removal efficiency decreases by approximately 1.5% for each unit increase in pH, holding other variables constant.

The significance of the regression (ANOVA F = 83.116, $p < 0.001$) confirms that the model overall is robust. Among the variables, only pH and FeO content (Variable 1) were statistically significant predictors ($p < 0.05$), while MW content (Variable 2) was not ($p = 0.409$).

Thus, the regression results quantitatively validate the observed trend in **Figure 3.9** and confirm that pH has a statistically significant and negative impact on RBBR dye adsorption efficiency.

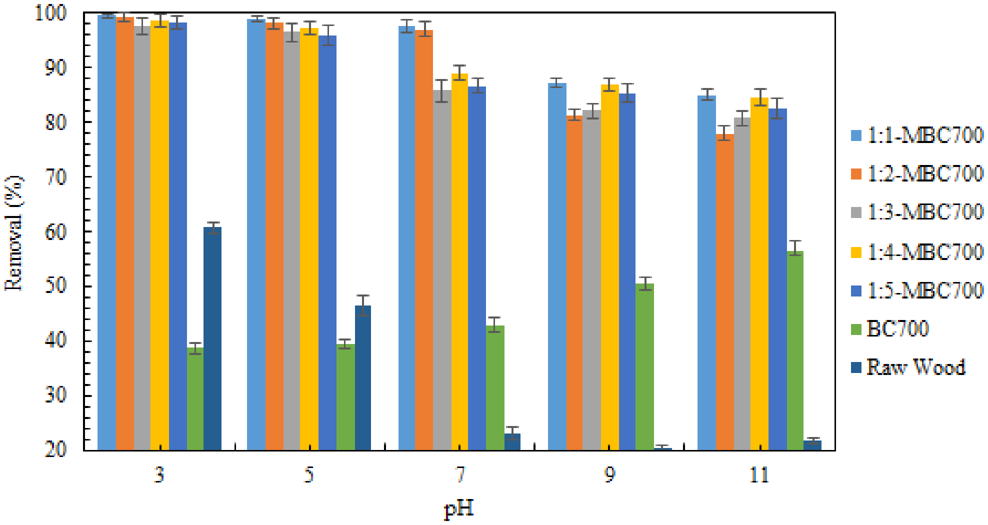

Figure 3.9 Effect of pH on RBBR adsorption efficiency

3.3.3. Adsorption kinetics

This study examined the adsorption kinetics of MBC to evaluate RBBR removal rates from aqueous solutions. The experimental data were fitted to various kinetic models, including the pseudo-first-order, pseudo-second-order, intra-particle diffusion, and film diffusion models, all shown in **Figure 3.10**.

The parameters are presented in **Tables A3.5** and **A3.6** in the Appendix. Across all dye concentrations, the correlation coefficient (R^2) for the pseudo-second-order remained consistently high (0.990-0.998), surpassing the values for the pseudo-first-order (0.688-0.859), indicating that the pseudo-second-order provided a better fit to the experimental data. This observation suggests that the adsorption of RBBR dye onto MBC likely follows chemisorption processes, as has been similarly observed in previous studies of dye adsorption on BC materials [50, 51] also yield adsorption capacities (Q_{cal}) that align closely with the experimental values of Q_{max}, reinforcing the model's applicability. As shown in **Table A3.5**, Q_{max} values for RBBR adsorption ranged from 4.84

mg/g at 100 ppm to 21.14 mg/g at 500 ppm, reflecting the concentration-dependent nature of dye uptake by MBC. This trend aligns with the saturation of adsorption sites as the initial concentration increases [52]. Furthermore, the pseudo-first-order and pseudo-second-order rate constants (k_1 and k_2, respectively) reveal their inverse relationship with RBBR concentration. The pseudo-first-order rate constant k_1 decreased from 0.0204 min^{-1} at 100 ppm to 0.0099 min^{-1} at 500 ppm, while the pseudo-second-order rate constant k_2 also diminished from 0.1458 g/mg·min at 200 ppm to 0.0099 g/mg·min at 500 ppm. This trend indicates decreased initial adsorption rates at higher concentrations due to the limited availability of active sites, as reported in other studies on BC-based adsorbents [53]. The higher accuracy of the model and the slight decrease in k_2 with increasing concentration suggest that the adsorption of RBBR onto MBC is controlled predominantly by chemical interactions, possibly involving electron-sharing or exchange interactions between RBBR dye molecules and functional groups on the MBC surface, such as hydroxyl (-OH) and carboxyl (-COOH) groups, which facilitate chemisorption [53, 54].

Table A3.6 shows poor correlation coefficients (R^2) for IPDM, ranging from 0.6080 to 0.8475. The non-linearity of the plots suggests that intraparticle diffusion may not be the sole rate-limiting step governing the adsorption process. Instead, it indicates that other mechanisms, such as surface adsorption or film diffusion, might accompany intraparticle diffusion. The correlation coefficients for FDM ranged from 0.653 to 0.911. The relatively higher R^2 values compared to the IPDM indicate that film diffusion may play a more significant role in governing the overall adsorption kinetics. This suggests that the transport of dye molecules through the liquid film surrounding the adsorbent particles contributes significantly to the adsorption rate. Compared to all the kinetic models studied, the R^2 values of IPDM and FDM are low compared to the PSOM; the adsorption was mostly chemisorption involving sharing or exchanging electrons between the MBC and dye molecules [55, 56]

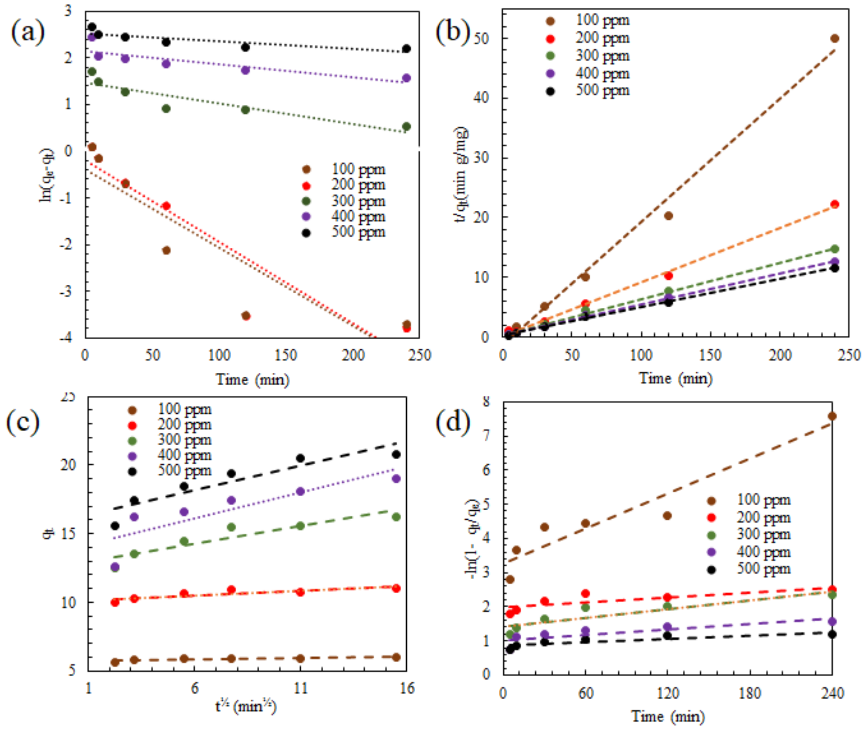

Figure 3.10 (a) Pseudo-first-order, (b) Pseudo-second-order, (c) Intra-particle diffusion, and (d) Film diffusion model of adsorption of RBBR dye by MBC

3.3.4. Adsorption Isotherm

Three commonly used isotherm models, namely the *Langmuir* isotherm model, the *Freundlich* isotherm model, and the *Temkin* isotherm model (TIM), were employed to analyze the experimental data. These models are illustrated in **Figure 3.11(a-c)**, and the parameters are presented in **Table A3.7** of the appendix section.

In **Table A3.7**, the R^2 values show that the *Langmuir* isotherm model (0.9877) was the best fit compared to the *Freundlich* isotherm model (0.9154) and the *Temkin* isotherm model (0.925). According to the *Langmuir* isotherm model, the adsorption of RBBR dye onto MBC occurs via monolayer adsorption. This happens through specific interactions between the dye molecules and binding sites on the MBC surface. As the dye molecules attach to the surface, they form a monolayer, with each binding site occupied by one dye molecule [57]. This monolayer adsorption process is characterized by a high affinity between the dye molecules and the MBC surface, resulting in a strong binding of the dye molecules to the MBC. A higher K_L(>1) value for LIM indicates stronger adsorption affinity and more efficient adsorption. Similarly, Eltaweil et al. [58]

reported that the *Langmuir* isotherm model provided the best fit ($R^2 = 0.9980$) for the adsorption of malachite green dye onto MBC derived from corn straw, indicating monolayer adsorption behavior and a strong affinity between the dye molecules and the MBC surface.

The correlation coefficient value ($R^2 = 0.9154$) suggests a reasonable fit of the experimental data to the *Freundlich* isotherm model. It indicates heterogeneous adsorption behavior and favorable dye adsorption onto the MBC. A lower n_F value (<1) and k_f value of 43.271 from **Table A3.4** indicate relatively low favourability of adsorption and moderate adsorption capacity and affinity between the adsorbate and adsorbent. The *Temkin* isotherm model showed a correlation coefficient value of $R^2 = 0.925$, indicating a reasonable fit, suggesting that the adsorption process may involve moderate adsorbent-adsorbate interactions and a degree of nonlinearity in the adsorption energy. The *Temkin* isotherm constant B_T represents the heat of adsorption and reflects the adsorbent-adsorbate interaction energy. A B_t value of 143.47 indicates a relatively strong adsorbent-adsorbate interaction energy. k_t is related to the adsorption equilibrium and indicates the adsorption capacity of the adsorbent material. The k_t value of 12.42 suggests a moderate adsorption capacity and a relatively fast rate.

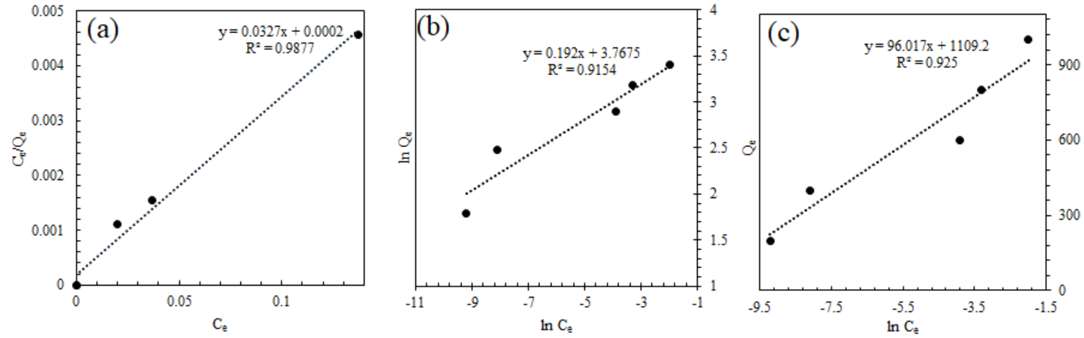

Figure 3.11 (a) *Langmuir*, (b) *Freundlich*, and (c) *Temkin* isotherm model profiles for RBBR dye on the prepared MBC

3.3.5. Point of zero charge (pH_{pzc})

The point of zero charge (pH_{pzc}) of the synthesized MBC was determined using the pH drift method, as illustrated in **Figure 3.12(a)**. The pH_{pzc} was found to be 8.4, indicating that the surface of the MBC carries a positive charge when the solution pH is below 8.4, and a negative charge when the pH is above this value. During the adsorption of RBBR, which is an anionic dye, the solution pH was maintained below the pH_{pzc}. As a result, the positively charged MBC surface promoted electrostatic attraction between the surface and the negatively charged dye molecules, enhancing dye uptake.

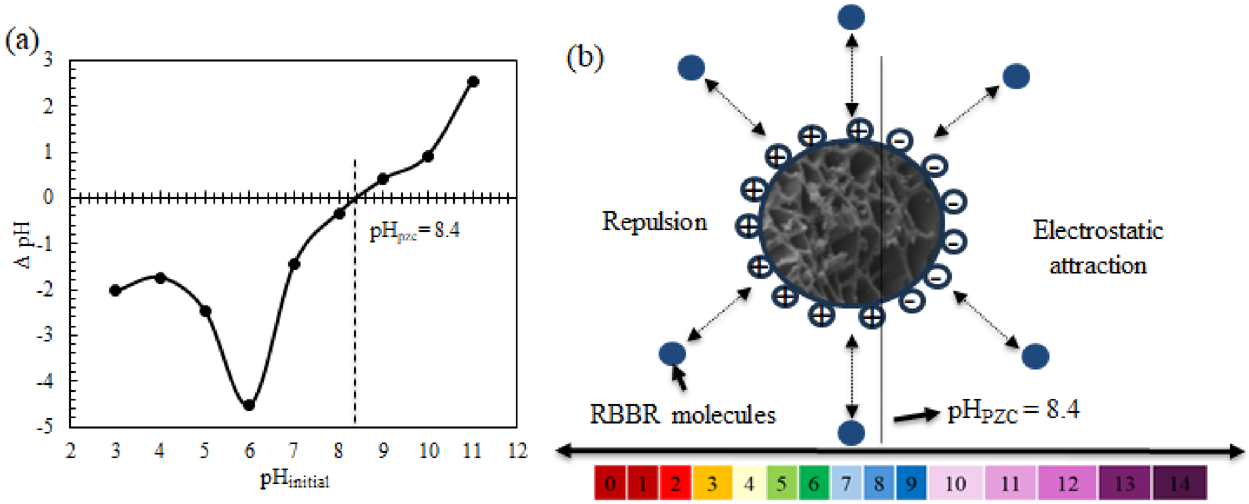

Figure 3.12 (a) Point of zero charge (pH_{PZC}) and (b) Influence of surface charge on RBBR adsorption

3.3.6. Adsorption mechanism

The adsorption of RBBR dye onto MBC occurs via multiple mechanisms, including electrostatic interaction, coordination, surface complexation, π-π stacking, and physisorption, as illustrated in **Figure 3.13**. FTIR and XPS analyses confirmed the presence of key functional groups such as -OH, C=O, C-O, C=C, and Fe-O, which facilitate dye binding. Electrostatic attraction plays a major role, especially at pH levels below the MBC's point of zero charge (pH_{Pzc} = 8.4), where the surface is positively charged and effectively attracts the dye's negatively charged sulfonate ($-SO_3^-$) groups [49]. This behavior is evident in **Fig. 3.12(b)**, where strong attraction below pH 8.4 contrasts with repulsion at higher pH. Additionally, Fe atoms in the Fe-O groups on the MBC act as coordination sites, bonding with oxygen atoms in the dye's sulfonic groups, thereby stabilizing the RBBR on the surface. Surface complexation further enhances adsorption, with FTIR and XPS analysis revealing hydroxyl (-OH) and carbonyl (C=O) groups on the adsorbent surfaces. These functional groups interact with the sulfonic and azo groups in the dye through hydrogen bonding, particularly between the -OH groups and the oxygen atoms in the dye's sulfonic groups, strengthening the adsorption process. π-π stacking interactions also play a significant role, as the carbon-carbon double bonds (C=C) in the MBC overlap with the π-electron clouds of the dye's aromatic rings, stabilizing the dye molecules through non-covalent bonding [59]. Physisorption occurs as dye molecules are initially adsorbed onto the MBC's external surface and subsequently diffuse into its internal pores, driven by the concentration gradient between the bulk solution and the MBC. Although MBC has a lower surface area than BC700, its porous structure provides sufficient sites for physical adsorption. These combined mechanisms contribute to the effective adsorption of RBBR dye by the MBC.

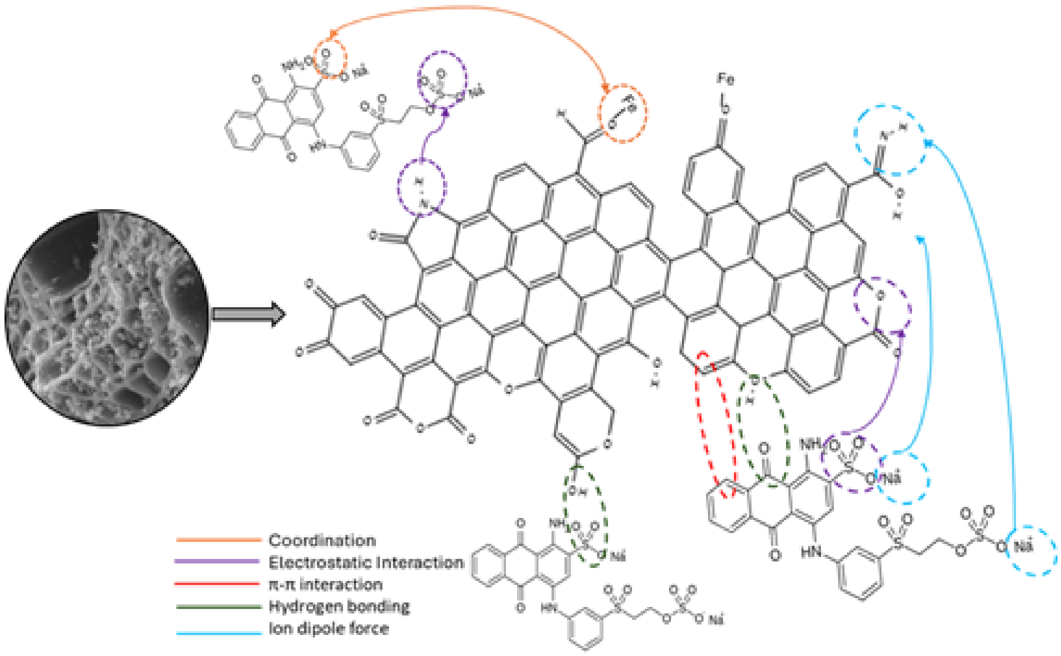

Figure 3.13 Possible adsorption mechanism of RBBR dye onto MBC

3.3.7. Comparison of results from recent studies on dye removal

Table 3.2 compares recent studies on dye removal using BC-based adsorbents derived from various biomasses, including wood chips, Patula pine wood, mulberry wood waste, southern pine, and beech wood. These studies demonstrated high dye removal efficiencies, ranging from 85.9 % to 100 %, with differing pyrolysis temperatures (500 °C to 700 °C), dye concentrations (20 PPM to 300 PPM), adsorbent dosages (0.1 g/L to 200 g/L), contact times (0.33 hours to 48 hours), and pH levels (4 to 9). In comparison, this study on MW-derived MBC achieved a maximum removal efficiency of 100 % for RBBR dye at a pyrolysis temperature of 700 °C, with a dye concentration of 100 PPM, an adsorbent dosage of 16.7 g/L, and a contact time of just 2 hours. This study stands out due to its high removal efficiency, relatively moderate adsorbent dosage, and short contact time, demonstrating a more efficient and effective approach for dye removal compared to the other studies.

Table 3.2 Recent studies on dye removal by various wood-based BC

Biomass	Pyrolysis temperature (°C)	Dye	Dye concentration (PPM)	Adsorbent dosage (g/L)	Max. removal efficiency (%)	Contact time (hour)	pH	Reference
Wood chip	Not provided	Acid Blue 161	100	20	93.5	48	7	[60]
Patula pine wood	700	Malachite Green	50	6	85.9	1	4	[61]
Mulberry wood waste	500	Methylene Blue	200	200	98	2	9	[62]
Southern pine	700	Congo red	300	0.75	98	4	4	[63]
Beechwood	650	Methylene Blue	20	0.1	100	0.33	6	[64]
Maple wood	700	RBBR	100	16.7	100	2	6.5	This study

3.4. Conclusion

In this study, we successfully synthesized MBC using different iron anchoring methods, with one-step co-pyrolysis proving to be the most effective. The 1:1 FeO-to-biomass ratio, combined with pyrolysis at 700 °C, demonstrated optimal adsorption performance for the removal of RBBR dye, achieving a removal efficiency of up to 100%. The study highlights the critical role of iron anchoring in enhancing the physicochemical properties of MBC and its adsorption efficiency. Detailed characterizations revealed the successful integration of magnetic properties and functional groups crucial for adsorption mechanisms, such as chemisorption, hydrogen bonding, and electrostatic interactions. The *Langmuir* isotherm and pseudo-second-order kinetic models accurately described the adsorption process. This research not only deepens the understanding of MBC synthesis and its functional mechanisms but also offers an energy-efficient method for producing high-performance adsorbents for sustainable water treatment applications.

References

[1] K. Maheshwari, M. Agrawal, and A. B. Gupta, "Dye Pollution in Water and Wastewater," in *Novel Materials for Dye-containing Wastewater Treatment*, S. S. Muthu and A. Khadir Eds. Singapore: Springer Singapore, 2021, pp. 1-25.

[2] M. Farhan Hanafi and N. Sapawe, "A review on the water problem associate with organic pollutants derived from phenol, methyl orange, and remazol brilliant blue dyes," *Materials Today: Proceedings,* vol. 31, pp. A141-A150, 2020/01/01/ 2020, doi: https://doi.org/10.1016/j.matpr.2021.01.258.

[3] S. Ihaddaden, D. Aberkane, A. Boukerroui, and D. Robert, "Removal of methylene blue (basic dye) by coagulation-flocculation with biomaterials (bentonite and Opuntia ficus indica)," *Journal of Water Process Engineering,* vol. 49, p. 102952, 2022/10/01/ 2022, doi: https://doi.org/10.1016/j.jwpe.2022.102952.

[4] H. Rashidi, N. N. Sulaiman, and N. Hashim, "Batik industry synthetic wastewater treatment using nanofiltration membrane," *Procedia Engineering,* vol. 44, pp. 2010-2012, 2012.

[5] M. Punzi, B. Mattiasson, and M. Jonstrup, "Treatment of synthetic textile wastewater by homogeneous and heterogeneous photo-Fenton oxidation," *Journal of Photochemistry and Photobiology A: Chemistry,* vol. 248, pp. 30-35, 2012.

[6] S. Nannu Shankar, D. R. Dinakaran, D. K. Chandran, G. Mantha, B. Srinivasan, and U. P. Nyayiru Kannaian, "Adsorption kinetics, equilibrium and thermodynamics of a textile dye V5BN by a natural nanocomplex material: Clinoptilolite," *Energy Nexus,* vol. 10, p. 100197, 2023/06/01/ 2023, doi: https://doi.org/10.1016/j.nexus.2023.100197.

[7] R. Rashid, I. Shafiq, P. Akhter, M. J. Iqbal, and M. Hussain, "A state-of-the-art review on wastewater treatment techniques: the effectiveness of adsorption method," *Environmental Science and Pollution Research,* vol. 28, pp. 9050-9066, 2021.

[8] K. Kang, Y. Hu, I. Khan, S. He, and P. Fatehi, "Recent advances in the synthesis and application of magnetic biochar for wastewater treatment," *Bioresource Technology,* vol. 390, p. 129786, 2023.

[9] Y. S. Ho and G. McKay, "Pseudo-second order model for sorption processes," *Process Biochemistry,* vol. 34, no. 5, pp. 451-465, 1999/07/01/ 1999, doi: https://doi.org/10.1016/S0032-9592(98)00112-5.

[10] S. Lagergren, "Zur theorie der sogenannten adsorption geloster stoffe," *Kungliga svenska vetenskapsakademiens. Handlingar,* vol. 24, pp. 1-39, 1898.

[11] W. J. Weber Jr and J. C. Morris, "Kinetics of adsorption on carbon from solution," *Journal of the sanitary engineering division,* vol. 89, no. 2, pp. 31-59, 1963.

[12] G. Boyd, A. Adamson, and L. Myers Jr, "The exchange adsorption of ions from aqueous solutions by organic zeolites. II. Kinetics1," *Journal of the American Chemical Society,* vol. 69, no. 11, pp. 2836-2848, 1947.

[13] I. Langmuir, "The adsorption of gases on plane surfaces of glass, mica and platinum," *Journal of the American Chemical society,* vol. 40, no. 9, pp. 1361-1403, 1918.

[14] H. Freundlich, "Über die adsorption in lösungen," *Zeitschrift für physikalische Chemie,* vol. 57, no. 1, pp. 385-470, 1907.

[15] M. Temkin, "Kinetics of ammonia synthesis on promoted iron catalysts," *Acta physiochim. URSS,* vol. 12, pp. 327-356, 1940.

[16] A. Selvarajoo and D. Oochit, "Effect of pyrolysis temperature on product yields of palm fibre and its biochar characteristics," *Materials Science for Energy Technologies,* vol. 3, pp. 575-583, 2020.

[17] V. Stagno *et al.*, "Discrimination between softwood and hardwood based on hemicellulose content obtained with portable nuclear magnetic resonance," *Cellulose,* vol. 29, no. 14, pp. 7917-7934, 2022/09/01 2022, doi: 10.1007/s10570-022-04728-x.

[18] M.-e. Zhong *et al.*, "Low-Temperature Reduction Synthesis of γ–Fe2O3− x@ biochar Catalysts and Their Combining with Peroxymonosulfate for Quinclorac Degradation," *International journal of environmental research and public health,* vol. 19, no. 24, p. 16790, 2022.

[19] L. Puri, Y. Hu, and G. Naterer, "Critical review of the role of ash content and composition in biomass pyrolysis," *Frontiers in Fuels,* vol. 2, p. 1378361, 2024.

[20] L. Zhang, Y. Dong, J. Liu, C. Liu, W. Liu, and H. Lin, "The effect of co-pyrolysis temperature for iron-biochar composites on their adsorption behavior of antimonite and antimonate in aqueous solution," *Bioresource Technology,* vol. 347, p. 126362, 2022/03/01/ 2022, doi: https://doi.org/10.1016/j.biortech.2021.126362.

[21] Y. Wang *et al.*, "Adsorption behavior of Cr(VI) by magnetically modified Enteromorpha prolifera based biochar and the toxicity analysis," *Journal of Hazardous Materials,* vol. 395, p. 122658, 2020/08/05/ 2020, doi: https://doi.org/10.1016/j.jhazmat.2020.122658.

[22] L. Hu, X.-Y. Wei, X.-H. Guo, H.-P. Lv, and G.-H. Wang, "Investigation on the kinetic behavior, thermodynamic and volatile products analysis of chili straw waste pyrolysis," *Journal of Environmental Chemical Engineering,* vol. 9, no. 5, p. 105859, 2021/10/01/ 2021, doi: https://doi.org/10.1016/j.jece.2021.105859.

[23] M. Kumar, D. Prasad, and M. K. Mondal, "Adsorption analysis of Zn (II) removal from aqueous solution onto Argemone maxicana biochar," *Biomass Conversion and Biorefinery,* vol. 13, no. 5, pp. 4135-4148, 2023.

[24] U. Younis *et al.*, "Fourier Transform Infrared Spectroscopy vibrational bands study of Spinacia oleracea and Trigonella corniculata under biochar amendment in naturally contaminated soil," *PLoS One,* vol. 16, no. 6, p. e0253390, 2021.

[25] C. Zhang *et al.*, "Evolution of the functionalities and structures of biochar in pyrolysis of poplar in a wide temperature range," *Bioresource Technology,* vol. 304, p. 123002, 2020/05/01/ 2020, doi: https://doi.org/10.1016/j.biortech.2020.123002.

[26] J. Prabahar, B. Vafaei, E. Baffoe, and A. Ghahremaninezhad, "The effect of biochar on the properties of alkali-activated slag pastes," *Construction Materials,* vol. 2, no. 1, pp. 1-14, 2021.

[27] T. C. Egbosiuba *et al.*, "Adsorption of Cr(VI), Ni(II), Fe(II) and Cd(II) ions by KIAgNPs decorated MWCNTs in a batch and fixed bed process," *Scientific Reports,* vol. 11, no. 1, p. 75, 2021/01/08 2021, doi: 10.1038/s41598-020-79857-z.

[28] E. Leng, Y. He, Y. Xue, L. Leng, and H. He, "Interactions between cellulose and lignin during pyrolysis: Evolutions of condensed-phase functional groups and gas-phase volatile fraction," *Industrial Crops and Products,* vol. 205, p. 117518, 2023/12/01/ 2023, doi: https://doi.org/10.1016/j.indcrop.2023.117518.

[29] Y. Yi, G. Tu, D. Zhao, P. E. Tsang, and Z. Fang, "Key role of FeO in the reduction of Cr(VI) by magnetic biochar synthesised using steel pickling waste liquor and sugarcane bagasse," *Journal of Cleaner Production,* vol. 245, p. 118886, 2020/02/01/ 2020, doi: https://doi.org/10.1016/j.jclepro.2019.118886.

[30] J. Song, Z. Huang, and M. Gamal El-Din, "Adsorption of metals in oil sands process water by a biochar/iron oxide composite: Influence of the composite structure and surface functional groups," *Chemical Engineering Journal,* vol. 421, p. 129937, 2021/10/01/ 2021, doi: https://doi.org/10.1016/j.cej.2021.129937.

[31] H. Ezz, M. G. Ibrahim, M. Fujii, and M. Nasr, "Dual biogas and biochar production from rice straw biomass: a techno-economic and sustainable development approach," *Biomass Conversion and Biorefinery,* vol. 13, no. 12, pp. 10807-10821, 2023.

[32] O. Tomin and M. R. Yazdani, "Production and characterization of porous magnetic biochar: before and after phosphate adsorption insights," *Journal of Porous Materials,* vol. 29, no. 3, pp. 849-859, 2022/06/01 2022, doi: 10.1007/s10934-022-01217-1.

[33] S. Mandal *et al.*, "Synergistic construction of green tea biochar supported nZVI for immobilization of lead in soil: A mechanistic investigation," *Environment International,* vol. 135, p. 105374, 2020/02/01/ 2020, doi: https://doi.org/10.1016/j.envint.2019.105374.

[34] S. Das and S. Mondal, "Synthesis of magnetic biochar derived from waste wood of acacia Auriculiformis for the removal of arsenic," *Environmental Nanotechnology, Monitoring & Management,* vol. 20, p. 100893, 2023/12/01/ 2023, doi: https://doi.org/10.1016/j.enmm.2023.100893.

[35] Y. Zhang *et al.*, "Novel carbothermal synthesis of Fe, N co-doped oak wood biochar (Fe/N-OB) for fast and effective Cr (VI) removal," *Colloids and Surfaces A: Physicochemical and Engineering Aspects,* vol. 600, p. 124926, 2020.

[36] Y. Li *et al.*, "Super-hydrophilic microporous biochar from biowaste for supercapacitor application," *Applied Surface Science,* vol. 561, p. 150076, 2021/09/30/ 2021, doi: https://doi.org/10.1016/j.apsusc.2021.150076.

[37] H. Liang, C. Zhu, S. Ji, P. Kannan, and F. Chen, "Magnetic Fe2O3/biochar composite prepared in a molten salt medium for antibiotic removal in water," *Biochar,* vol. 4, no. 1, p. 3, 2022.

[38] A. A. H. Saeed *et al.*, "Pristine and Magnetic Kenaf Fiber Biochar for Cd2+ Adsorption from Aqueous Solution," *International Journal of Environmental Research and Public Health,* vol. 18, no. 15, p. 7949, 2021. [Online]. Available: https://www.mdpi.com/1660-4601/18/15/7949.

[39] Y. Yi, G. Tu, P. Eric Tsang, and Z. Fang, "Insight into the influence of pyrolysis temperature on Fenton-like catalytic performance of magnetic biochar," *Chemical Engineering Journal,* vol. 380, p. 122518, 2020/01/15/ 2020, doi: https://doi.org/10.1016/j.cej.2019.122518.

[40] F. Meng, Z. Li, C. Lei, K. Yang, and D. Lin, "Removal of trichloroethene by iron-based biochar from anaerobic water: Key roles of Fe/C ratio and iron carbides," *Chemical Engineering Journal,* vol. 413, p. 127391, 2021/06/01/ 2021, doi: https://doi.org/10.1016/j.cej.2020.127391.

[41] Y. Wu *et al.*, "Cobalt ferrite/cellulose membrane inserted catalytic syringe filter for facile in-situ filtration/degradation of emerging organic pollutants in water via activating peroxymonosulfate," *Materials & Design,* vol. 220, p. 110817, 2022/08/01/ 2022, doi: https://doi.org/10.1016/j.matdes.2022.110817.

[42] S. T. Neeli, H. Ramsurn, C. Y. Ng, Y. Wang, and J. Lu, "Removal of Cr (VI), As (V), Cu (II), and Pb (II) using cellulose biochar supported iron nanoparticles: A kinetic and mechanistic study," *Journal of Environmental Chemical Engineering,* vol. 8, no. 5, p. 103886, 2020/10/01/ 2020, doi: https://doi.org/10.1016/j.jece.2020.103886.

[43] Y. Chen *et al.*, "The characterization of a novel magnetic biochar derived from sulfate-reducing sludge and its application for aqueous Cr (Ⅵ) removal through synergistic effects of adsorption and chemical reduction," *Chemosphere,* vol. 308, p. 136258, 2022.

[44] Z. Chen *et al.*, "Enhanced adsorption of phosphate on orange peel-based biochar activated by Ca/Zn composite: Adsorption efficiency and mechanisms," *Colloids and Surfaces A: Physicochemical and Engineering Aspects,* vol. 651, p. 129728, 2022/10/20/ 2022, doi: https://doi.org/10.1016/j.colsurfa.2022.129728.

[45] N. Zhang, F. Reguyal, S. Praneeth, and A. K. Sarmah, "A green approach of biochar-supported magnetic nanocomposites from white tea waste: Production, characterization and plausible synthesis mechanisms," *Science of The Total Environment,* vol. 886, p. 163923, 2023/08/15/ 2023, doi: https://doi.org/10.1016/j.scitotenv.2023.163923.

[46] J. Qu *et al.*, "Magnetic porous biochar with high specific surface area derived from microwave-assisted hydrothermal and pyrolysis treatments of water hyacinth for Cr(Ⅵ) and tetracycline adsorption from water," *Bioresource Technology,* vol. 340, p. 125692, 2021/11/01/ 2021, doi: https://doi.org/10.1016/j.biortech.2021.125692.

[47] X. Li, C. Wang, J. Tian, J. Liu, and G. Chen, "Comparison of adsorption properties for cadmium removal from aqueous solution by Enteromorpha prolifera biochar modified with different chemical reagents," *Environmental Research,* vol. 186, p. 109502, 2020/07/01/ 2020, doi: https://doi.org/10.1016/j.envres.2020.109502.

[48] F. Ullah *et al.*, "Adsorption performance and mechanism of cationic and anionic dyes by KOH activated biochar derived from medical waste pyrolysis," *Environmental Pollution,* vol. 314, p. 120271, 2022/12/01/ 2022, doi: https://doi.org/10.1016/j.envpol.2022.120271.

[49] V. Parimelazhagan, P. Yashwath, D. Arukkani Pushparajan, and J. Carpenter, "Rapid Removal of Toxic Remazol Brilliant Blue-R Dye from Aqueous Solutions Using Juglans nigra Shell Biomass Activated Carbon as Potential Adsorbent: Optimization, Isotherm, Kinetic, and Thermodynamic Investigation," *International Journal of Molecular Sciences,* vol. 23, no. 20, p. 12484, 2022. [Online]. Available: https://www.mdpi.com/1422-0067/23/20/12484.

[50] P. Ganguly, R. Sarkhel, and P. Das, "Synthesis of pyrolyzed biochar and its application for dye removal: Batch, kinetic and isotherm with linear and non-linear mathematical analysis," *Surfaces and Interfaces,* vol. 20, p. 100616, 2020/09/01/ 2020, doi: https://doi.org/10.1016/j.surfin.2020.100616.

[51] J. O. Ighalo, K. O. Iwuozor, C. A. Igwegbe, and A. G. Adeniyi, "Verification of pore size effect on aqueous-phase adsorption kinetics: A case study of methylene blue," *Colloids and Surfaces A: Physicochemical and Engineering Aspects,* vol. 626, p. 127119, 2021/10/05/ 2021, doi: https://doi.org/10.1016/j.colsurfa.2021.127119.

[52] T.-J. Jiang, H. M. Morgan, W.-T. Tsai, H. Chien, T.-B. Yen, and Y.-R. Lee, "Thermochemical Conversion of Biomass into Biochar: Enhancing Adsorption Kinetics and Pore Properties for Environmental Sustainability," *Sustainability,* vol. 16, no. 15, p. 6623, 2024. [Online]. Available: https://www.mdpi.com/2071-1050/16/15/6623.

[53] B. Zeng *et al.*, "Preparation of sludge biochar rich in carboxyl/hydroxyl groups by quenching process and its excellent adsorption performance for Cr(VI)," *Chemosphere,* vol. 285, p. 131439, 2021/12/01/ 2021, doi: https://doi.org/10.1016/j.chemosphere.2021.131439.

[54] L. Zhu, L. Tong, N. Zhao, X. Wang, X. Yang, and Y. Lv, "Key factors and microscopic mechanisms controlling adsorption of cadmium by surface oxidized and aminated biochars," *Journal of Hazardous Materials,* vol. 382, p. 121002, 2020.

[55] A. Eleryan *et al.*, "Kinetic and isotherm studies of Acid Orange 7 dye absorption using sulphonated mandarin biochar treated with TETA," *Biomass Conversion and Biorefinery,* vol. 14, no. 9, pp. 10599-10610, 2024/05/01 2024, doi: 10.1007/s13399-023-04089-w.

[56] H.-O. Chahinez, O. Abdelkader, Y. Leila, and H. N. Tran, "One-stage preparation of palm petiole-derived biochar: Characterization and application for adsorption of crystal violet dye in water," *Environmental Technology & Innovation,* vol. 19, p. 100872, 2020.

[57] G. F. Abu-Alsoud, K. A. Hawboldt, and C. S. Bottaro, "Comparison of Four Adsorption Isotherm Models for Characterizing Molecular Recognition of Individual Phenolic Compounds in Porous Tailor-Made Molecularly Imprinted Polymer Films," *ACS Applied Materials & Interfaces,* vol. 12, no. 10, pp. 11998-12009, 2020/03/11 2020, doi: 10.1021/acsami.9b21493.

[58] A. S. Eltaweil, H. Ali Mohamed, E. M. Abd El-Monaem, and G. M. El-Subruiti, "Mesoporous magnetic biochar composite for enhanced adsorption of malachite green dye: Characterization, adsorption kinetics, thermodynamics and isotherms," *Advanced Powder Technology,* vol. 31, no. 3, pp. 1253-1263, 2020/03/01/ 2020, doi: https://doi.org/10.1016/j.apt.2020.01.005.

[59] A. Ahmadi, M. Hajilou, S. Zavari, and S. Yaghmaei, "A comparative review on adsorption and photocatalytic degradation of classified dyes with metal/non-metal-based modification of graphitic carbon nitride nanocomposites: Synthesis, mechanism, and affecting parameters," *Journal of Cleaner Production,* vol. 382, p. 134967, 2023/01/01/ 2023, doi: https://doi.org/10.1016/j.jclepro.2022.134967.

[60] S. Ortiz-Monsalve *et al.*, "Degradation of a leather-dye by the combination of depolymerised wood-chip biochar adsorption and solid-state fermentation with Trametes villosa SCS-10," *Bioresources and Bioprocessing,* vol. 7, no. 1, p. 61, 2020/11/25 2020, doi: 10.1186/s40643-020-00349-z.

[61] A. Rubio-Clemente, J. Gutiérrez, H. Henao, A. M. Melo, J. F. Pérez, and E. Chica, "Adsorption capacity of the biochar obtained from Pinus patula wood micro-gasification for the treatment of polluted water containing malachite green dye," *Journal of King Saud*

University - Engineering Sciences, vol. 35, no. 7, pp. 431-441, 2023/11/01/ 2023, doi: https://doi.org/10.1016/j.jksues.2021.07.006.

[62] S. Mutahir *et al.*, "Synthesis of mulberry wood waste biochar through acid modification for removal of dyes: experimental and DFT-based analysis," *Biomass Conversion and Biorefinery,* 2023/07/14 2023, doi: 10.1007/s13399-023-04595-x.

[63] Z. Zhang, M. Zhang, X. Zhao, and J. Cao, "High-efficient removal and adsorption mechanism of organic dyes in wastewater by KOH-activated biochar from phenol-formaldehyde resin modified wood," *Separation and Purification Technology,* vol. 330, p. 125542, 2024.

[64] H. Zeghioud, L. Fryda, A. Mahieu, R. Visser, and A. Kane, "Potential of Flax Shives and Beech Wood-Derived Biochar in Methylene Blue and Carbamazepine Removal from Aqueous Solutions," *Materials,* vol. 15, no. 8, p. 2824, 2022. [Online]. Available: https://www.mdpi.com/1996-1944/15/8/2824.

Chapter 4 Pre-pyrolysis activation strategy to enhance heavy metal adsorption by industrial waste-based magnetic biochar

Abstract

Red mud and biomass-based magnetic biochar (MBC) are a novel type of sustainable heavy metal adsorbent that shows lots of potential for metal-polluted water cleaning. However, improving MBC's adsorption performance by post-production chemical activation is difficult due to the destruction of surface functionalities and loss of magnetic properties due to oxidation of the surface iron components. In this study, we developed a new process for MBC production by biomass activation followed by the co-pyrolysis of KOH and HNO_3-activated maple wood and red mud to enhance its adsorption capacity for Cu and Pb. The characterization data showed the presence of oxygen-containing functional groups on the produced MBC. The KOH activation introduced more oxygen-containing functional groups, such as -OH and -COOH, facilitating stronger interactions with metal ions. This resulted in high adsorption efficiency, achieving nearly 100% removal for Cu^{2+} and Pb^{2+}, while HNO_3-MBC demonstrated slightly lower removal efficiencies (~95%). The adsorption mechanism, dominated by chemisorption, involves electrostatic attraction, complexation, ion exchange, precipitation, and redox reactions. Economic analysis revealed that KOH-MBC had a lower production cost (CAD 15.47/kg) than HNO_3-MBC (CAD 41.29/kg), indicating that KOH-MBC is significantly more cost-effective for large-scale production for water treatment applications.

*Chapter 4 is submitted for publication in a peer-reviewed journal.

4.1. Introduction

The rapid expansion of industrial activities has led to the increased release of heavy metals into aquatic ecosystems, posing serious environmental and human health threats. Lead (Pb) and copper (Cu) are major environmental pollutants due to their toxicity, persistence, and bioaccumulation potential. They primarily originate from industries such as battery manufacturing, mining, metal plating, high-phosphate fertilizers, and municipal waste incineration [1, 2]. Pb and Cu exposure can lead to neurological damage, kidney dysfunction, oxidative stress, and enzymatic disruptions [3, 4]. Therefore, the development of efficient and sustainable remediation strategies is critical for mitigating such pollution.

Adsorption, particularly using biochar (BC) produced through biomass pyrolysis, is a popular method for heavy metal removal from contaminated water. Canada, with 367 million hectares of forest (9% of the world's total), is a major biomass residue producer across the globe [5]. Among available biomass sources, maple wood (MW) can be a potential feedstock for its renewability and wide availability across Canada, particularly in the eastern provinces of Ontario, Quebec, and the Atlantic provinces [6]. Its high lignocellulosic content (44-50% cellulose, 19.4-32% hemicellulose, and 24-25.5% lignin, respectively) makes it ideal for BC production due to its high carbon content, porous structure, and potential to produce abundant functional groups for adsorption [7, 8]. The utilization of MW in feedstock biomass also aligns with Canada's growing interests in bio-based solutions for environmental remediation and circular economy initiatives.

However, pristine BC often has low adsorption capacity because it lacks porosity and functional groups. Modification helps improve these properties, making it more effective for adsorption. For example, nitrogen-containing functional groups in N-doped BCs improved heavy metal adsorption through electrostatic attraction, hydrogen bonding, chelation, and complexation [9]. Similarly, nitrogen and phosphorus co-doped BC showed better Pb^{2+} adsorption due to surface complexation with oxygen-functional groups [10]. Acid modifications, such as treatment with HNO_3, have also proven effective due to the increases in the acidic functional group on BC, thereby enhancing its capacity to adsorb heavy metals like Pb^{2+} and Cd^{2+} [11]. Alkaline modifications, particularly with KOH, have been employed to increase BC's surface area and porosity. For example, KOH-activated Douglas fir BC exhibited a surface area of 1049 m^2/g, compared to 535 m^2/g for unmodified BC, resulting in higher adsorption capacities for Pb^{2+}, Cr^{2+}, and Cd^{2+} [12]. Another modification method is magnetic modification, which is widely researched for its ability to separate spent BC after use, reducing the risk of secondary pollution. Due to the non-toxic nature of Fe species, Fe-incorporated MBC is widely studied in wastewater treatment. It is typically synthesized using Fe precursors like $FeCl_3$, $FeSO_4$, FeO, etc. Recent advancements have focused on replacing conventional Fe-based chemicals with waste-derived alternatives [13, 14]. Red mud (RM), which consists of 35–65% iron oxides, has emerged as a sustainable substitute for synthetic iron salts in the production of MBC [15]. RM is a major waste byproduct of the Bayer process used for aluminum production. On average, 1.25 tonnes of RM is produced for every tonne of alumina, with global refineries generating an estimated 177.25 million tonnes in 2023 [16]. Canada, a leading aluminum producer (3.3 million tonnes in 2023), generates a substantial amount of RM [17]. The high alkalinity and metal content of RM pose environmental risks, as conventional disposal methods like landfilling and tailing ponds can lead to leaching and ecosystem degradation [18]. So, using RM for MBC synthesis not only mitigates disposal challenges but also promotes a circular economy by transforming industrial waste into a value-added material for environmental remediation.

Recent studies indicate that RM incorporation in BC enhances adsorption by introducing iron-based active sites, improving stability, and enabling easier magnetic separation [19, 20]. Despite these advantages, to the best of our knowledge, research on co-pyrolyzing chemically activated biomass with RM remains very limited. Furthermore, a simplified, one-step co-pyrolysis process incorporating RM with chemically activated biomass has not been extensively studied, and its potential for practical application remains underexplored. Moreover, acid and alkali modification of MW in combination with co-pyrolysis of the treated MW and RM to produce acid- and alkali-modified MBC has not been studied. Therefore, there is a need to study the effect of such a process on the formation pathways of such MBC materials and their functionality in adsorption applications.

This study seeks to bridge these gaps by synthesizing and characterizing MBC derived from MW and RM under two different chemical activation methods, namely, HNO_3 and KOH treatments. By comparing the physicochemical properties and adsorption performance of the resulting MBCs, this research provides insights into the role of activation chemistry in modifying surface functional groups, porosity, and magnetic characteristics. The integration of RM in MBC synthesis enhances its adsorption capabilities and contributes to sustainable waste management by repurposing a hazardous industrial byproduct. Through comprehensive adsorption experiments such as pH, contact time, and initial metal concentration, this study identifies optimal conditions for Pb^{2+} and Cu^{2+} removal while evaluating the environmental and cost analysis of the adsorbents. The findings can contribute to the advancement of MBC-based adsorbents for practical wastewater treatment applications and promote the sustainable utilization of waste biomass and metal-containing industrial waste materials.

4.2. Materials and methods

4.2.1. Materials

MW chips were bought from local stores in Thunder Bay, Ontario. Chemicals like copper (II) sulfate pentahydrate ($CuSO_4 \cdot 5H_2O$ ≥98% purity), lead (II) acetate trihydrate ($Pb(CH_3COO)_2 \cdot 3H_2O$ ≥99% purity), nitric acid (HNO_3, ultrapure grade, 69.0–70.0%), potassium hydroxide (KOH, 85–100.5% purity), hydrochloric acid (HCl, 24.5–26.0% purity), and sodium hydroxide (NaOH, reagent grade, 97%) were purchased from Sigma Aldrich. RM was collected from Alcan International Ltd., Canada, in a slurry state. The RM was dried in a muffle oven at 105 °C for 12 hours and then manually ground into powder. Deionized (DI) water from a Nanopure Water system (Barnstead) was used for cleaning, rinsing, dilution, and preparing stock solutions. Compressed nitrogen gas (N_2) for pyrolysis was supplied by Linde Canada Inc.

4.2.2. Preparation of the adsorbents

To prepare the modified MBC, the MW first underwent chemical treatment using both acid and alkali activations. For acid activation, 10 g of biomass was impregnated with 20 mL of a 1 M HNO_3 solution, stirred, and soaked for 4 hours. The treated MW was then dried overnight at 60-80 °C in a constant temperature oven (Model: DKN812, Yamato Scientific). Similarly, alkali activation was conducted using a 1 M KOH solution following the same procedure. The modified MBC was synthesized via a co-pyrolysis process by mixing the dried, chemically treated MW chips with RM at a MW-to-RM ratio of 5:1. This mixture was placed in ceramic boats and pyrolyzed in a tube furnace (Model: STF1200-60X1000, Across International, Nevada, USA) at 600 °C under a continuous N_2 flow of 250 mL/min. The heating rate was 10 °C/min, with a residence time of 3 hours. N_2 flow continued until the furnace returned to room temperature, after which the MBC samples were collected. The resulting MBC samples were designated as HNO_3-MBC and KOH-MBC, corresponding to the acid and alkali-activated processes, respectively.

4.2.3. Characterization methods

The elemental composition of carbon, hydrogen, nitrogen, and sulfur (CHNS) in the samples was determined using a Vario EL Cube analyzer. Proximate analysis (moisture, volatile matter, and ash content) was conducted according to ASTM standards (ASTM D3173-D3175) using a muffle furnace (Thermolyne, FB1415M, Thermo Scientific, Asheville, USA). The surface characteristics and pore volumes of the adsorbents were examined with a BELSORP MINI X automatic surface area and pore size analyzer, utilizing N_2 gas adsorption and desorption at 77 K. Surface textural properties and elemental composition were analyzed using a Hitachi SU-70 SEM with EDS. Surface functional groups were identified using FTIR (Bruker Tensor 37 spectrophotometer with a diamond ATR accessory). XRD analysis, performed with a PANalytical X'pert Pro diffractometer, revealed crystallographic structures and phase composition within a 6-96° range.

4.2.4. Batch adsorption, kinetics, and isotherm studies

Batch adsorption experiments were conducted to evaluate the adsorption efficiency. In each test, 30 mL of heavy metal-containing solution at varying concentrations was mixed with different adsorbent doses in 50 mL Falcon tubes. The experiments were performed across a range of pH levels (3, 5, 7, 9, and 11), with the pH adjusted using 0.1 M HCl or 0.1 M NaOH as needed. The samples were agitated at 300 rpm for 2 hours using a shaker (Excella E5, New Brunswick Scientific, Edison, NJ, USA). Following agitation, the solutions were filtered through 0.2 µm nylon syringe filters (Sartorius, CA, USA). The concentration of heavy metals in the filtered liquid samples was analyzed using an ICP-OES (Agilent 5900, equipped with SPS 4 Autosampler) instrument. The adsorption capacities at equilibrium (Q_e) were calculated based on **Equation 4.1**.

$$Q_e = \frac{C_o - C_e}{W} \times V \tag{4.1}$$

Here, C_o and C_e (mg/L) represent the initial and final concentrations after 2 hours of the metal salts in the liquid phase, respectively. V is the volume of the solution (L), and W is the mass of the adsorbent in grams.

Adsorption kinetics and isotherm studies of metal salts on MBC were analyzed using different models, including pseudo-first-order, pseudo-second-order, the *Langmuir* adsorption isotherm, and the *Freundlich* adsorption isotherm models.

Section A1 of the Appendix gives more details on these models.

4.2.5. Regeneration and reusability

After adsorption, 1.0 g of metal-loaded MBC was added to 10 mL of 0.1 M HCl solution and shaken at 250 RPM for 4 hours at room temperature to desorb the metal ions. The mixture was then filtered, and the recovered MBC was washed thoroughly with DI water to remove residual acid. The regenerated MBC was dried at 105 °C and again used in the next adsorption cycle. This process was repeated for 4 cycles to assess the stability and regeneration efficiency.

4.2.6. Statistical analysis

Statistical analysis of the factors, including adsorbent type, dosage, contact time, and pH was performed by two-way ANOVA using Microsoft Excel.

4.3. Results and discussion

4.3.1. Characterization

Basic properties

Table 4.1 shows the proximate analysis results of MW, its BC, and the modified MBC derivatives. MW has a high volatile matter content (85.36 ± 0.48%) and a low ash content (0.61 ± 0.11%), typical for woody biomass. After pyrolysis, the BC showed a drastic reduction in volatile matter (15.01 ± 0.57%) and a significant increase in fixed carbon (75.20 ± 3.70%), indicating the successful carbonization of MW. The ash content of BC increased to 8.71% compared to MW due to the concentration of inorganic components after volatile compounds were released. However, HNO_3-MBC exhibited a volatile matter content of 17.56 ± 2.23%, a much higher ash content (38.06 ± 0.54%), and a lower fixed carbon content (43.32 ± 1.31%) compared to that of the BC. This increase in ash content suggests that the RM contributed to the overall inorganic content of the product. Similarly, KOH-MBC showed even higher ash content (43.78 ± 1.31%) and volatile matter (22.51 ± 1.68%), with a lower fixed carbon content (30.52 ± 0.77%). Additionally, KOH-MBC had the highest moisture (3.20 ± 2.44%), which could be due to the hygroscopic nature of residual KOH or increased porosity.

Table 4.1 Proximate analysis of MW, its BC, and BC modified with HNO_3 and KOH (reported values represent the mean ± standard deviation)

Samples	Moisture (%)	Volatile Matter (%)	Ash (%)	Fixed Carbon (%)
MW	1.32 ± 0.09	85.36 ± 0.48	0.61 ± 0.11	12.71 ± 0.28
BC	1.08 ± 0.74	15.01 ± 0.57	8.71 ± 3.54	75.20 ± 3.70
HNO_3-MBC	1.06 ± 0.38	17.56 ± 2.23	38.06 ± 0.54	43.32 ± 1.31
KOH-MBC	3.20 ± 2.44	22.51 ± 1.68	43.78 ± 1.53	30.52 ± 0.77

The CHNS elemental analysis results are presented in **Table 4.2**. MW has a C content of 48.60%, which decreased slightly in the activated MW samples, HNO_3-MW (43.84%) and KOH-MW (43.56%). However, after pyrolysis, BC showed a sharp increase in C content (90.20%), indicating significant carbonization. After modification, HNO_3-MBC retained a moderate C content (48.43%), while KOH-MBC showed a significant reduction (31.96%), suggesting that KOH treatment led to more structural degradation. The N content was highest in HNO_3-treated samples (1.20% in HNO_3-MW and 0.83% in HNO_3-MBC), likely due to N incorporation during modification. The H/C molar ratio dropped significantly after pyrolysis (from ~1.43 in MW to 0.66 in BC), confirming the aromatization of BC. However, HNO_3-MBC and KOH-MBC showed slightly higher H/C ratios, 0.86 and 0.98, respectively, indicating some retention of aliphatic structures.

Table 4.2 Yield%, surface area, pore volume, and elemental analysis of the adsorbents

Samples	Yield (%)	S_{BET} (m^2/g)	Pore volume (cm^3/g)	Average pore volume (cm^3/g)	Average pore diameter (Å)	N%	C%	H%	S%	H/C, molar ratio
MW	-	-	-	-	-	0.06	48.60	5.80	0.02	1.43
HNO_3-MW	-	-	-	-	-	1.20	43.84	5.22	0.00	1.43
KOH-MW	-	-	-	-	-	0.08	43.56	5.89	0.01	1.62
BC	25.10 ± 0.35	41.35	0.075	0.055	26.51	0.34	90.20	4.95	0.03	0.66
HNO_3-MBC	36.90 ± 0.79	86.51	0.225	0.135	31.31	0.83	48.43	3.47	0.09	0.86
KOH-MBC	43.69 ± 0.87	3.57	0.086	0.061	344.72	0.18	31.96	2.60	0.06	0.98

BET analysis

The N_2 adsorption analysis results are presented in **Table 4.2**, and the N_2 adsorption-desorption isotherm shown in **Figure 4.1(a)** highlights the differences in surface area and pore characteristics of the samples. As shown in **Table 4.2**, HNO_3-MBC exhibited the highest surface area (86.51 m^2/g) and total pore volume (0.1354 cm^3/g), indicating a well-developed porous structure. The adsorption-desorption isotherm of HNO_3-MBC displayed a Type IV isotherm with an H_3 hysteresis loop, suggesting the presence of mesopores with slit-like structures, which facilitate enhanced ion adsorption by increasing surface-bound active sites. In contrast, BC displayed a moderate surface area (41.35 m^2/g) with a pore diameter of 26.51 Å, supporting its adsorption potential. Its isotherm showed a similar Type IV pattern- characteristic of mesoporous materials, indicating multilayer adsorption followed by capillary condensation within pores typically ranging from 2 to 50 nm, though with lower adsorption capacity than HNO_3-MBC. KOH-MBC, however, had a significantly lower surface area (3.57 m^2/g) but a much larger average pore diameter (344.72 Å), indicating a predominantly macroporous structure. The isotherm of KOH-MBC exhibited a Type II pattern with minimal hysteresis, suggesting a non-porous or macroporous material with limited N_2 uptake. Type II isotherms are typically associated with the unrestricted monolayer-multilayer adsorption on surfaces of non-porous or macroporous materials, where the point of inflection marks the completion of monolayer coverage and the onset of multilayer adsorption. These findings are further supported by the pore size distribution (**Fig. 4.1(b)**), where HNO_3-MBC displayed a sharp distribution below 100 nm, while KOH-MBC showed a broader peak toward larger pore sizes These results confirm that HNO_3 activation is more effective than KOH activation in enhancing the development of a mesoporous structure of the MBC. Speculating from the activation mechanisms, HNO_3 modification enhances the mesoporosity by removing impurities, increasing oxygen-containing functional groups, and partially oxidizing the carbon structure of the MW [21], where the mesoporosity will most likely be retained after the later co-pyrolysis. In comparison, KOH modification primarily induces macroporosity through chemical activation, leading to a low surface area of the later-produced KOH-MBC [22].

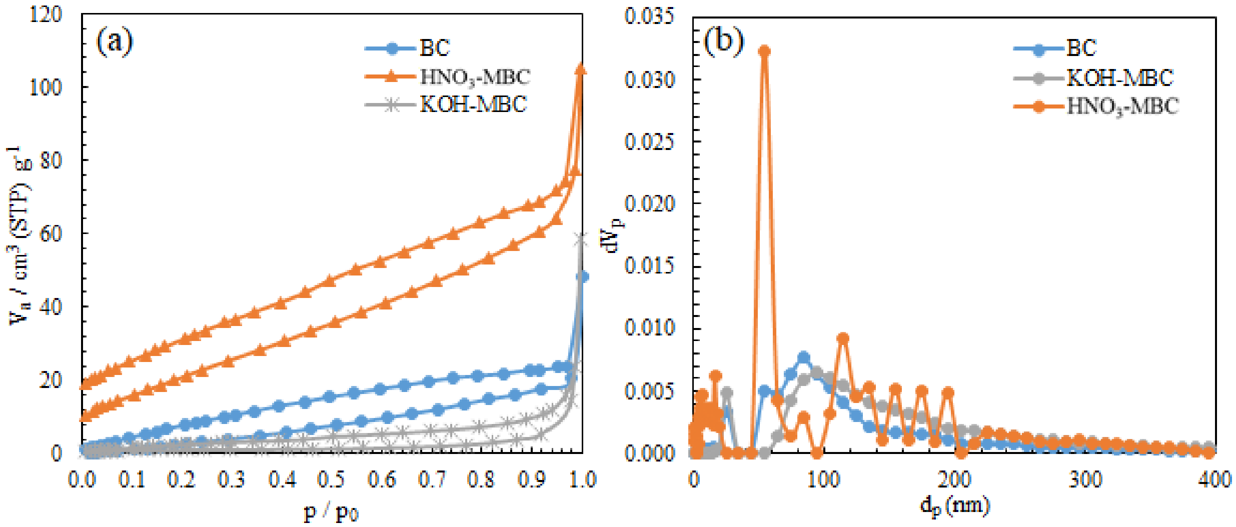

Figure 4.1 (a) N_2 adsorption-desorption isotherms, (b) Pore size distribution

SEM-EDS

SEM images of BC, KOH-MBC, and HNO_3-MBC were taken at 1.50k magnification (**Figure 4.2**), revealing distinct surface structural differences and the impact of chemical modifications. The SEM image of BC shows a well-developed, porous structure with interconnected pores and a smooth surface. The EDS analysis shows C as the dominant element, accounting for 91.92% by weight, with O making up 8.08%. The high carbon content suggests that the pyrolysis process effectively converted the MW into a C-rich material [23]. In contrast, the KOH-MBC displays a rougher surface morphology, with visible cracks and cavities. KOH reacts with C to form compounds like K_2CO_3 and K_2O, which etch the KOH-MBC's surface, creating micropores and increasing porosity [24]. The EDS spectrum for KOH-MBC shows the presence of C and O, along with significant peaks for Fe, K, and traces of Mg. The detection of Fe suggests successful impregnation of magnetic nanoparticles during the synthesis process, while the presence of K indicates residues from the KOH modification. The HNO_3-MBC sample exhibits a more fragmented and disordered surface compared to BC and KOH-MBC. The SEM image shows smaller pores and particle aggregation, which may result from the HNO_3 modification process that alters the BC's surface structure [25]. The EDS spectrum for HNO_3-MBC highlights the presence of C, O, Fe, and N. The detection of N is likely due to the introduction of N-containing functional groups through the HNO_3 treatment. In addition, comparing the openness of Fig. 2 (b) and (c), it is clear that KOH-MBC showed apparent signs of pore mouth collapse but better anchoring of inorganic particles. This is in coherence with its much higher average pore diameter compared to that of the HNO_3-MBC (**Table 4.2**).

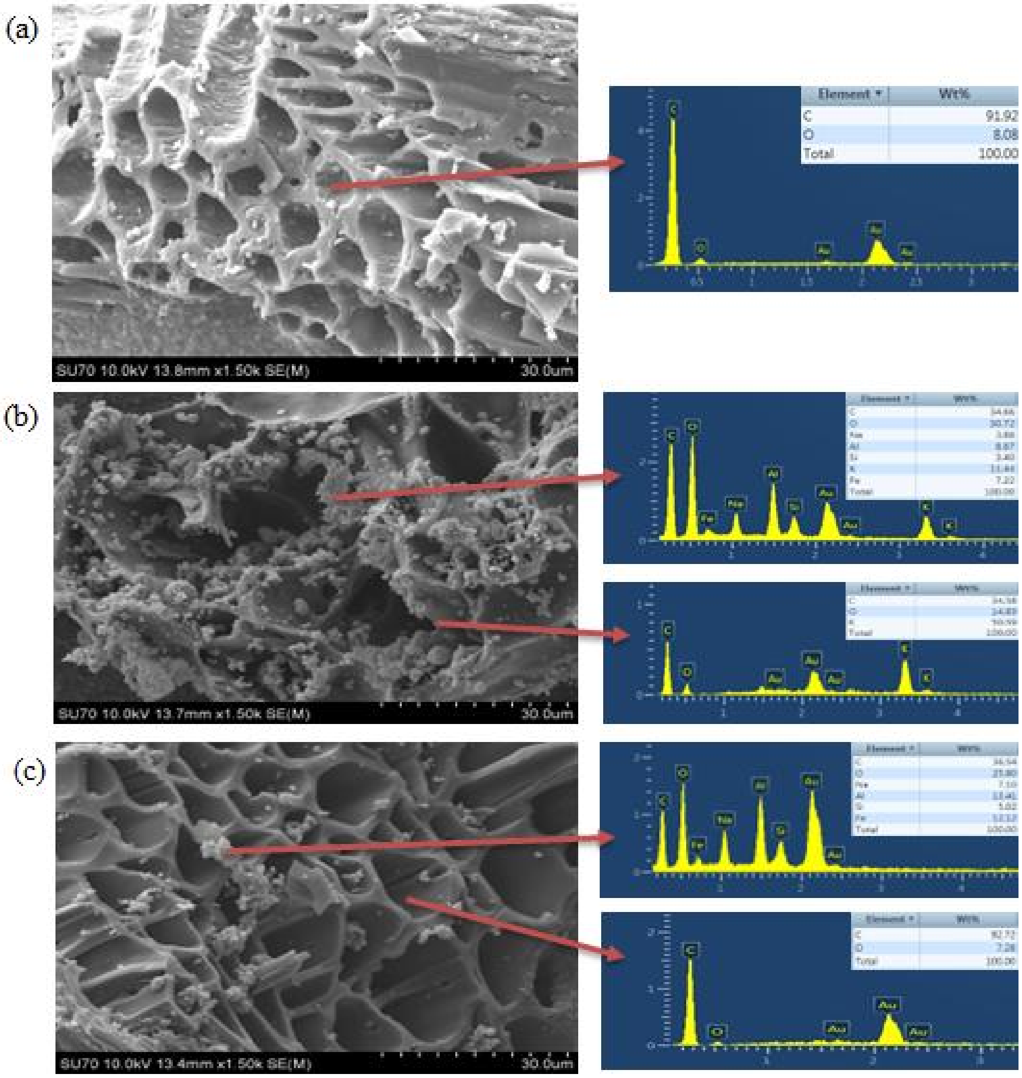

Figure 4.2 SEM images of (a) BC, (b) KOH-MBC, and (c) HNO_3-MBC at 1.50k magnification with corresponding EDS spectra

FTIR analysis

The FTIR spectra of MW, chemically activated MW samples (KOH-MW, HNO_3-MW), and their chars (BC, KOH-MBC, HNO_3-MBC) are presented in **Figure 4.3**. MW exhibits characteristic peaks associated with lignocellulosic biomass. The C=O stretching vibration appears around 1732 cm^{-1}, corresponding to aldehyde and carboxyl functional groups, while the C=C stretching band near 1585 cm^{-1} is attributed to cyclic alkene structures. Peaks at approximately 1465 and 1450 cm^{-1} are associated with C-H bending in alkanes, whereas the strong bands between 1100 and 1000

cm^{-1} correspond to C-O stretching in polysaccharides. KOH-MW exhibits sharper and broader peaks, suggesting a more pronounced structural change, while HNO_3-MW displays less distinct peak features, likely due to differences in degradation and modification caused by the activation. Pyrolysis of MW into BC results in significant structural transformations. The intensity of the C=O stretching band in MW and activated MW diminishes in BC, indicating the thermal decomposition of carbonyl-containing groups. BC also shows a weak band around 1560.34 cm^{-1}, suggesting C=C stretching in aromatic structures, while additional peaks at ~864.07, ~815.85, and ~736.77 cm^{-1} correspond to C=C bending vibrations, indicative of an increasingly condensed aromatic framework. Co-pyrolysis with RM (KOH-MBC, HNO_3-MBC) introduces further spectral modifications. For both KOH-MBC and HNO_3-MBC, a new peak at 1430 cm^{-1} appears, corresponding to O-H bending from carboxyl functional groups, suggesting surface interactions with RM components. Additionally, a strong band around 980 cm^{-1} is observed, which is attributed to aromatic C=C bending, confirming the retention of BC's graphitic structure after modification.

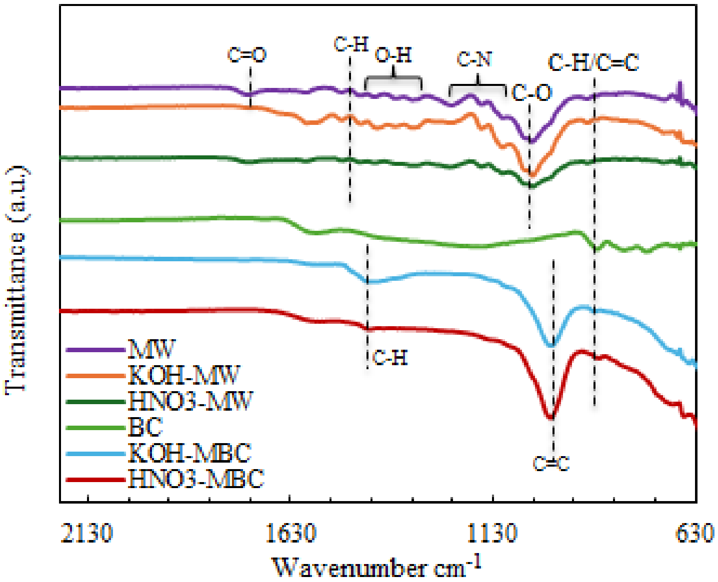

Figure 4.3 FTIR spectra of MW, activated biomass, and MBCs derived from the activated biomass

XRD analysis

The structural differences between MW, BC, KOH-MBC, and HNO_3-MBC are shown in **Figure 4.4**. The broad diffraction peak observed in the MW spectrum at ~22° corresponds to the amorphous cellulose and hemicellulose structure [26]. After pyrolysis, this characteristic peak gradually broadened, indicating thermal degradation of cellulose, hemicellulose, and lignin. The small peak observed in the BC sample at 2θ values around 43~44° is associated with carbon, indicating that MW has undergone a transformation into graphite [27]. Chemically modified KOH-MBC and HNO3-MBC display distinct diffraction peaks, indicative of phase changes induced by the respective chemical treatments. The XRD spectra of KOH-MBC exhibit characteristic peaks at 2θ = 30.53°, 31.98°, 35.81°, and 44.82°, corresponding to the (200), (220), (400), and (422) crystallographic planes, which are indicative of the presence of magnetite [28]. Additionally, a broad diffraction peak at 2θ ≈ 24° corresponds to the (002) plane of amorphous graphitic carbon, suggesting the presence of disordered carbon structures [29]. In contrast, HNO_3 treatment introduces oxygen-containing functional groups and modifies the crystalline phases of iron oxides. The diffraction peaks observed for HNO_3-MBC at 2θ values of 30.48°, 36.89°, 43.53°, 57.45°, and 63.01° correspond to the (200), (400), (422), (511), and (440) crystalline planes respectively, which are characteristic of magnetite [28]. Furthermore, additional peaks at 2θ = 14.042° (101 plane) and 24.36° (002 plane) are characteristic of amorphous graphitic carbon [30].

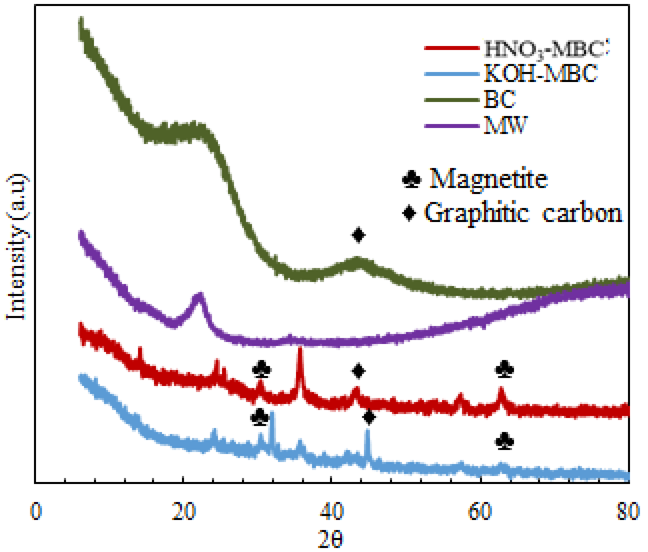

Figure 4.4 XRD spectra of MW, BC, and modified KOH-MBC and HNO_3-MBC

4.3.2. Adsorption studies

Effect of adsorbent dosage

Figure 4.5 shows the influence of adsorbent dosage on the removal efficiency of Cu and Pb. For Cu adsorption (**Figure 4.5(a)**), the removal efficiency showed a sharp increase with increasing dosage for all adsorbents. KOH-MBC exhibited the highest Cu removal efficiency, reaching nearly

100% at a dosage of 0.2 g. Similarly, the HNO_3-MBC demonstrated a rapid increase in removal, achieving 95.59 ± 1.29% efficiency at a 0.6 g dosage. In contrast, BC and MW showed lower adsorption performance, with the removal efficiency gradually increasing to a maximum of 12.24 ± 0.76% and 7.84 ± 1.52%, respectively, at the highest dosage. For Pb adsorption (**Figure 4.5(b)**), a similar trend was observed, with KOH-MBC and HNO_3-MBC achieving superior performance compared to BC and MW. KOH-MBC achieved near-complete Pb removal (~100%) at a dosage of 0.3 g, while HNO_3-MBC also showed high removal efficiency, reaching ~95% at 0.6 g dosage. Both BC and MW exhibited a more gradual increase in removal efficiency, with BC reaching approximately 34.80 ± 3.00% and MW around 65.64 ± 2.12% at the highest dosage. The improved removal efficiency with increasing adsorbent dosage can be attributed to the higher availability of active adsorption sites, which facilitates greater metal ion binding. The superior performance of KOH-MBC and HNO_3-MBC can be linked to their enhanced porosity and the presence of oxygen-containing functional groups, as confirmed by the FTIR and XRD.

The regression analysis supports the observed trends in **Table A4.1** and **Table A4.2** by quantitatively affirming the strong relationship between adsorbent type, dosage, and heavy metal removal efficiency. For both Cu and Pb, the models showed high coefficients of determination ($R^2 = 0.924$ for Cu and 0.927 for Pb), indicating that over 92% of the variation in removal efficiency is explained by the model variables. Among the adsorbents, the regression coefficients for KOH-modified biochar (X1) were set to zero due to being used as the baseline (reference), while the significantly negative coefficients for HNO_3-modified (X2) and pristine biochar (X3) reflect their relatively lower performance compared to KOH-MBC. Additionally, the positive and statistically significant coefficients for dosage (X4) in both models (Cu: 69.552, Pb: 81.678; $p < 0.01$) confirm that increasing the dosage substantially enhances removal efficiency. The model's strong F-statistics (Cu: 57.09, Pb: 59.27; $p < 0.001$) further validate the overall significance of the regression. These findings statistically reinforce the experimental observation that higher dosage and KOH-MBC treatment led to superior Cu and Pb removal, likely due to increased active site availability and enhanced surface functionality.

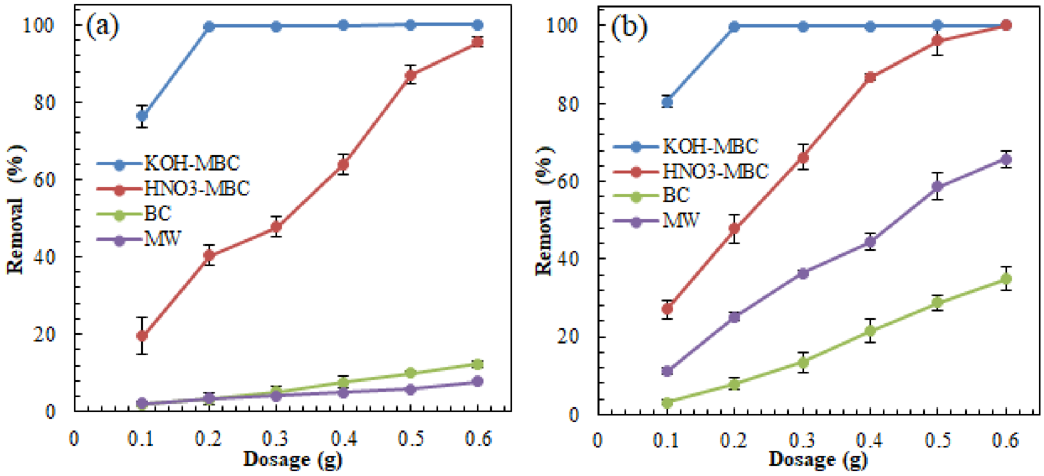

Figure 4.5 Effect of adsorbent dosage on the adsorption efficiency of (a) Cu and (b) Pb (pH: 6.5; salt concentration: 500 ppm)

Effect of contact time

The effect of contact time on the adsorption efficiency of Cu and Pb, shown in **Figure 4.6**, was evaluated at pH ~7 with an initial metal ion concentration of 500 ppm. In the case of Cu (**Figure 4.6(a)**), KOH-MBC demonstrated the highest removal efficiency, reaching nearly 100% within the first 20 minutes of contact time. HNO_3-MBC also showed a rapid increase in Cu removal, achieving 80.01 ± 1.92% efficiency within 60 minutes, after which it gradually stabilized. In contrast, BC exhibited a slower and less efficient adsorption process, with Cu removal reaching around 14.33 ± 1.79% after 120 minutes. Similarly, the Pb adsorption efficiency (**Figure 4.6(b)**) followed a comparable trend. KOH-MBC achieved near-complete Pb removal (~100%) within 20 minutes, indicating fast and effective adsorption. HNO_3-MBC also demonstrated significant Pb adsorption, reaching 85.94 ± 4.33% removal efficiency within 50 minutes. However, BC showed a slower Pb removal rate, achieving only around 52 ± 2.17% after 120 minutes of contact time. The rapid initial adsorption of Cu and Pb onto both KOH-MBC and HNO_3-MBC can be attributed to the abundant availability of active adsorption sites on the MBC surface. In the early stages, metal ions readily interact with functional groups such as $-COO^-$, -OH, and $-O^-$ via electrostatic attraction, complexation, and ion exchange mechanisms. As adsorption progresses, these sites become occupied, slowing the adsorption due to increased resistance to mass transfer and diffusion limitations. Similar trends have been reported in previous studies on BC-based adsorbents for heavy metal removal [31, 32].

In the regression model (**Table A4.3** and **Table A4.4**), the high R^2 values (0.932 for Cu and 0.901 for Pb) indicate that over 90% of the variability in removal efficiency is explained by the model. For both metals, the KOH-modified BC (X1) served as the reference category, while the significantly negative coefficients for HNO_3-MBC (Cu: –32.806; Pb: -27.216) and pristine BC (Cu: -85.931; Pb: -72.251) underscore their lower performance relative to KOH-MBC. Most notably, the positive and statistically significant coefficients for contact time (X4) in both models (Cu: 0.304, Pb: 0.340; $p < 0.001$) reinforce that increased contact time enhances metal removal efficiency. The high F-values (Cu: 117.97, Pb: 79.24; $p < 0.001$) confirm the overall significance of the regression. These findings are consistent with the experimental results, where KOH-MBC rapidly achieved near-complete removal of both Cu and Pb within 20 minutes, indicating efficient interaction between metal ions and the functionalized surface of the adsorbent during early contact periods.

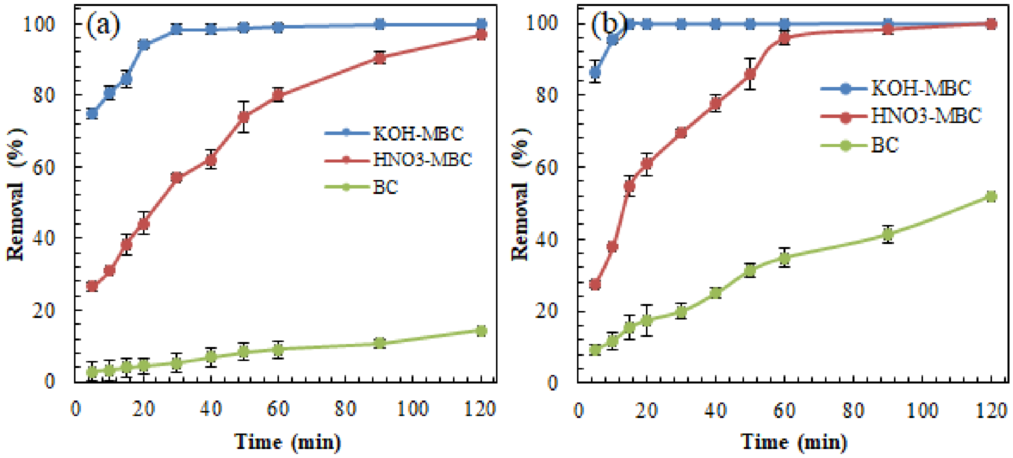

Figure 4.6 Effect of contact time on the adsorption efficiency of (a) Cu and (b) Pb (pH: 7; metal concentration: 500 ppm)

Effect of pH

The adsorption efficiency of Cu and Pb onto the adsorbents was significantly influenced by the solution pH, as shown in **Figure 4.7**. For Cu (**Figure 4.7(a)**), the removal efficiency increased with rising pH, reaching 99.66 ± 0.001% KOH-MBC at pH 7 and above. Similarly, HNO_3-MBC exhibited high adsorption efficiency, achieving almost complete Cu removal (~100%) at pH 9. In contrast, BC showed significantly lower removal efficiency across all pH values, with maximum adsorption of around 76.49 ± 1.90% at pH 11. Similarly, for Pb adsorption (**Figure 4.7(b)**), KOH-

MBC achieved 99.74 ± 0.06% removal efficiency at pH 7, with HNO_3-MBC closely following at around 96.26 ± 3.72%. BC exhibited a relatively lower Pb removal efficiency, reaching approximately 72.22 ± 3.81% at pH 11. The sharp increase in adsorption efficiency at pH values above 3 can be attributed to the reduced competition between H^+ ions and metal ions for active adsorption sites on the BC surface. At lower pH values, the high concentration of H^+ ions leads to the protonation of functional groups (e.g., carboxyl and hydroxyl groups) on the MBC surface, reducing their ability to bind with metal ions [33]. As the pH increases, deprotonation of these functional groups occurs, enhancing electrostatic interactions and complexation with metal ions, thereby improving adsorption efficiency [34]. The higher performance of KOH-MBC compared to HNO_3-MBC and BC across varying pH levels can be attributed to several factors. Although KOH-MBC has a lower surface area, the KOH activation introduces more oxygen-containing functional groups, such as -OH and -COOH, which facilitate stronger interactions with metal ions. In contrast, HNO_3 modification primarily introduces acidic functional groups, which may not interact as effectively with metal cations [35, 36].

The statistical analysis supports the observed trends in the effect of pH on Cu and Pb adsorption efficiencies (**Table A4.5** and **Table A4.6**). For Cu, the regression model showed a strong relationship between the independent variables (BC type and pH) and removal efficiency, with an R^2 of 0.821 and an adjusted R^2 of 0.682. Similarly, for Pb, the model showed a slightly higher R^2 of 0.837 and an adjusted R^2 of 0.702. In both cases, the models were statistically significant ($p < 0.001$), indicating that the predictors reliably explain the variation in metal removal. Notably, the coefficients for pH (X4) were statistically significant ($p < 0.001$) and positive for both Cu ($\beta = 9.673$) and Pb ($\beta = 9.848$), confirming that increasing pH enhances adsorption efficiency. The positive coefficients for HNO_3-modified (X2) and pristine BC (X3) also reflect their respective contributions to adsorption performance compared to the reference (KOH-MBC), with HNO_3-MBC showing a stronger effect. These findings are consistent with the experimental data, where higher pH levels facilitated deprotonation of surface functional groups, improving electrostatic attraction and complexation with metal ions. Overall, the regression outcomes validate the role of pH and BC type in influencing metal ion uptake.

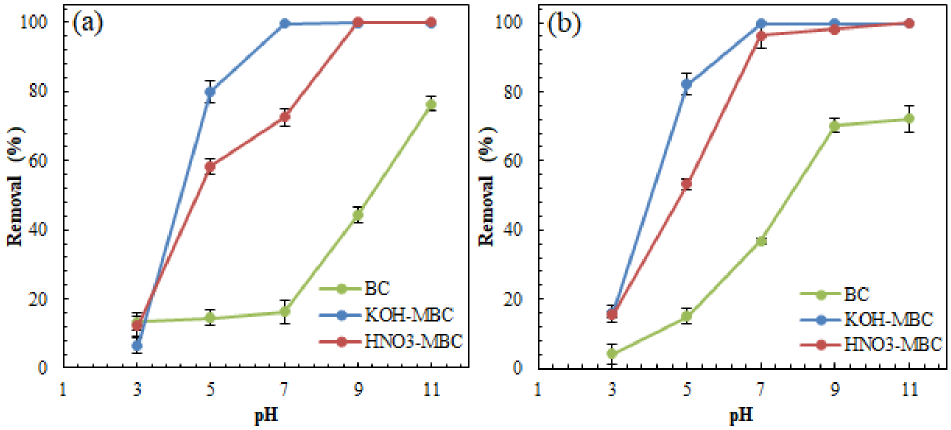

Figure 4.7 Effect of pH on the adsorption of (a) Cu and (b) Pb onto the adsorbents

4.3.3. Kinetic studies

The adsorption kinetics of Cu and Pb onto KOH and HNO_3-modified MBC were evaluated using pseudo-first-order and pseudo-second-order models. The kinetic data, along with corresponding parameters, are presented in **Table 4.3**, while the model fitting is illustrated in **Figure 4.8**. Across all tested concentrations (500–700 ppm), the pseudo-second-order model provided a better fit for Cu and Pb adsorption onto both KOH-MBC and HNO_3-MBC, with R^2 values consistently higher (0.959–1) than those of the pseudo-first-order model (0.721–0.971). This suggests that chemisorption governs the adsorption process on both samples. Also, this explains why KOH-MBC had a lower surface area but performed better than HNO_3-MBC.

For KOH-MBC, Cu adsorption showed an increase in pseudo-second-order equilibrium adsorption capacity (Q_e), rising from 65.36 mg/g at 500 ppm to 87.72 mg/g at 700 ppm, with high R^2 values (0.98–0.99), confirming the model's applicability. A similar trend was observed for Pb adsorption, where Q_e increased from 69.93 mg/g at 500 ppm to 87.72 mg/g at 700 ppm. In contrast, HNO_3-MBC exhibited lower adsorption capacities, with Cu adsorption Q_e values of 31.85 mg/g, 1.94 mg/g, and 19.23 mg/g at 500, 600, and 700 ppm, respectively. Similarly, Pb adsorption onto HNO_3-MBC showed a maximum Q_e of 32.47 mg/g at 500 ppm, decreasing to 30.40 mg/g at 700 ppm. These results indicate that KOH modification leads to better adsorption than HNO_3 modification, possibly due to differences in functional group composition and surface reactivity.

The pseudo-second-order rate constant (k_2) varied across different conditions, generally decreasing with increasing concentration, suggesting a gradual transition toward diffusion-controlled adsorption as active sites become saturated. For instance, Cu adsorption onto KOH-MBC decreased k_2 from 0.5222 g/mg·min at 500 ppm to 0.0550 g/mg·min at 700 ppm. Pb adsorption followed a similar trend, with k_2 values decreasing from 0.8266 to 0.0550 g/mg·min. This trend suggests that while initial adsorption is rapid, subsequent adsorption becomes slower due to the reduced availability of active sites. These findings align with previous studies on heavy metal adsorption using engineered BC materials [37, 38].

Table 4.3 Kinetic parameters for the adsorption of Cu and Pb on KOH-MBC and HNO_3-MBC: pseudo-first-order and pseudo-second-order models

Adsorbent	**Metal salt**	**Conc. (PPM)**	**Pseudo-first-order**			**Pseudo-second-order**		
			Q_{max} (mg/g)	**k_1**	**R^2**	**Q_e (mg/g)**	**k_2**	**R^2**
KOH-MBC	Cu	500	13.29	0.0474	0.965	65.36	0.5222	0.999
		600	1.25	0.0234	0.786	8.00	0.8675	1.000
		700	74.04	0.0425	0.943	87.72	0.0550	0.985
	Pb	500	24.43	0.0956	0.887	69.93	0.8266	0.999
		600	41.29	0.0001	0.841	5.26	0.6810	0.999
		700	10.94	0.0356	0.967	87.72	0.0550	0.985
HNO_3-MBC	Cu	500	31.40	0.0397	0.971	31.85	0.0353	0.971
		600	1.92	0.0365	0.826	1.94	0.0557	0.979
		700	35.24	0.0035	0.916	19.23	0.0328	0.959
	Pb	500	56.34	0.0034	0.763	32.47	0.0580	0.994
		600	3.33	0.0409	0.721	3.16	0.0765	0.975
		700	24.19	0.0454	0.864	30.40	0.1143	0.998

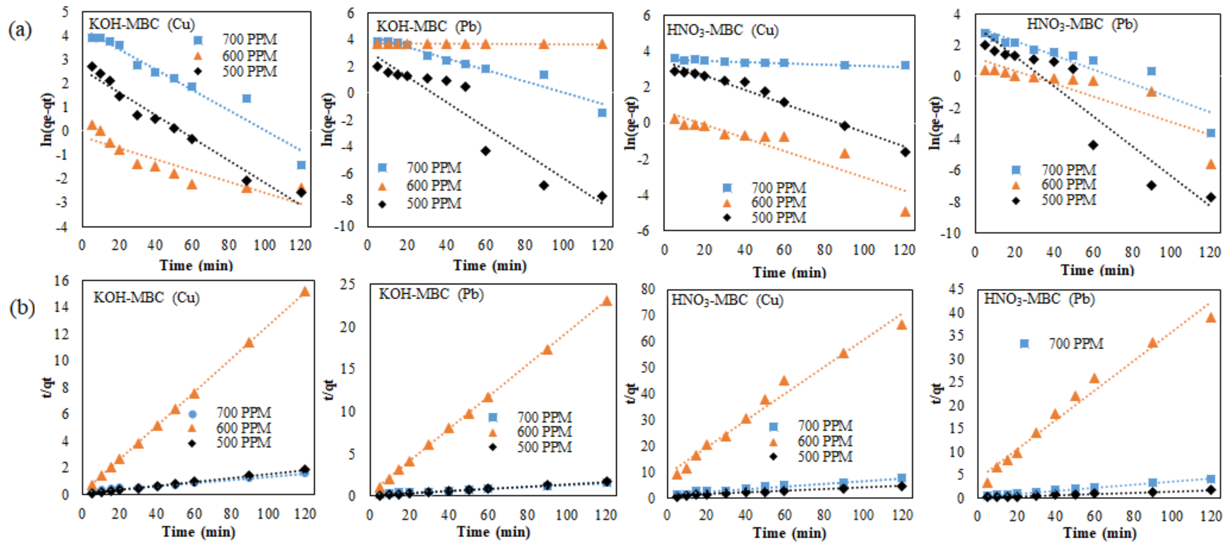

Figure 4.8 Adsorption kinetics of Cu and Pb on KOH-MBC and HNO_3-MBC: (a) Pseudo-first-order and (b) Pseudo-second-order model

4.3.4. Isotherm studies

The *Langmuir* and *Freundlich* isotherm models are presented in **Figure 4.9**, with the isotherm parameters summarized in **Table 4.4**. For both Cu and Pb, the *Langmuir* isotherm model provided better fits, with R^2 values above 0.90, indicating that adsorption occurred predominantly as a monolayer on the modified MBC surfaces. The maximum adsorption capacities (Q_{max}) were significantly higher for KOH-MBC (80 mg/g for Cu and 92.59 mg/g for Pb) than for HNO_3-MBC (37.59 mg/g for Cu and 38.61 mg/g for Pb), suggesting that KOH activation enhanced the adsorption capacity by increasing available binding sites. The *Freundlich* isotherm model also showed a reasonable fit, particularly for KOH-MBC, with high K_f values (33.50 for Cu and 28.92 for Pb), indicating strong adsorption affinity. However, the lower R^2 values for HNO_3-MBC in the *Freundlich* isotherm model (0.6716 for Cu and 0.732 for Pb) suggest that the adsorption on this MBC was less heterogeneous. The n_f values were greater than 1 for all cases, confirming favorable adsorption [39]. Overall, KOH-MBC exhibited superior adsorption capacity compared to HNO_3-MBC, likely due to its greater porosity and surface reactivity, making it a more effective adsorbent for Cu and Pb removal.

Table 4.4 Isotherm parameters for the adsorption of Cu and Pb on KOH-MBC and HNO_3-MBC: the *Langmuir* and the *Freundlich* isotherm models.

Metal salt	**Adsorbents**	***Langmuir***			***Freundlich***		
		Q_{max}	**K_l**	**R^2**	**K_f**	**n_f**	**R^2**
Cu	KOH-MBC	80.00	0.414	0.954	33.50	5.206	0.899
	HNO_3-MBC	37.59	0.017	0.906	7.04	3.791	0.672
Pb	KOH-MBC	92.59	0.053	0.981	28.92	4.627	0.721
	HNO_3-MBC	38.61	0.055	0.980	11.31	4.305	0.732

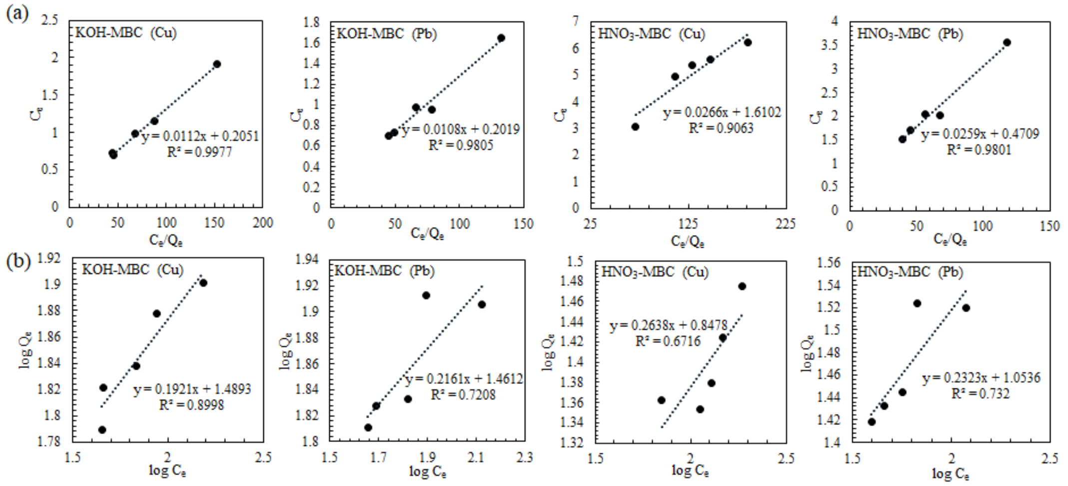

Figure 4.9 Adsorption isotherms of Cu and Pb on KOH-MBC and HNO_3-MBC: (a) *Langmuir* model and (b) *Freundlich* adsorption isotherm model

4.3.5. Point of zero charge (pH_{pzc})

The point of zero charge (pH_{pzc}) is the pH at which the net surface charge of an adsorbent is zero. As shown in **Figure 4.10**, the ΔpH becomes zero at an initial pH of approximately 10.5, which is defined as the pH_{pzc} for both KOH-MBC and HNO_3-MBC. The high pH_{pzc} can be attributed to the presence of metal oxides from RM and alkaline functional groups introduced during chemical activation. This property is critical for cation adsorption. Since both Pb^{2+} and Cu^{2+} are positively charged, their removal is more favorable at $pH > pH_{pzc}$ due to electrostatic attraction with the negatively charged surface sites. At $pH < pH_{pzc}$, surface sites are protonated, leading to electrostatic repulsion between the adsorbent and cationic metals, thereby reducing adsorption efficiency.

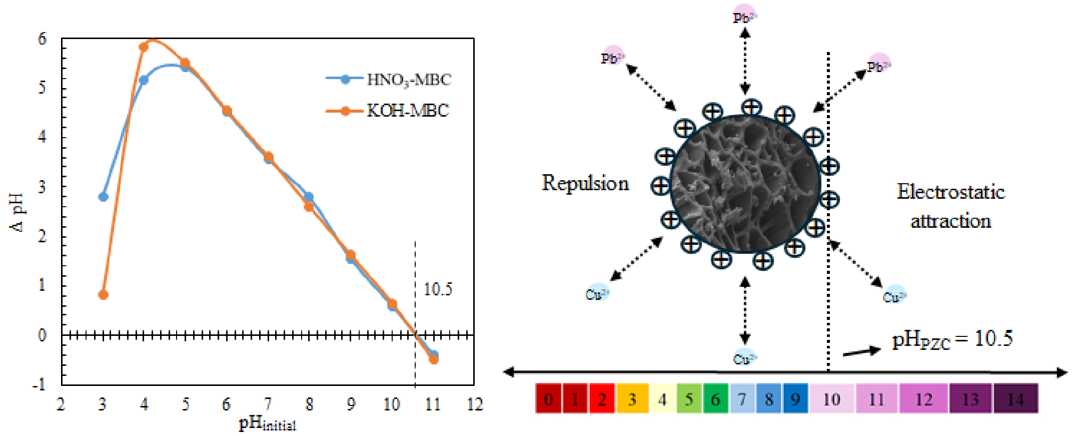

Figure 4.10 Point of zero charge and influence of surface charge on Cu^{2+} and Pb^{2+} adsorption onto KOH-MBC and HNO_3-MBC

4.3.6. Possible adsorption mechanisms

The possible adsorption of Cu^{2+} and Pb^{2+} onto KOH-MBC and HNO_3-MBBC can involve multiple mechanisms, including electrostatic attraction, complexation, ion exchange, precipitation, and redox reactions, as illustrated in **Figure 4.11**. The post-adsorption FTIR spectra (**Fig. A4.1(a)**) show a notable shift at 1438 cm^{-1}, which appeared as a weaker shoulder at 1406 cm^{-1} in Cu and Pb-loaded KOH-MBC. This shift suggests a possible complexation between the metal ions and C=O or -OH functional groups. The downshift in wavenumber indicates a change in electron density, likely due to metal coordination, where Pb^{2+} or Cu^{2+} binds with oxygen-containing groups on the MBC surface. Additionally, the peak at 983 cm^{-1} in KOH-MBC and HNO_3-MBC slightly shifted to 987 cm^{-1} and weakened upon metal adsorption. This peak is typically associated with C–O stretching vibrations or phosphate-related groups. The shift and intensity reduction imply interactions between Cu^{2+}/Pb^{2+} and oxygen-rich functional sites, further supporting the formation of inner-sphere complexes. The disappearance of most original functional group peaks after adsorption highlights the role of ion exchange, surface complexation, and electrostatic interactions in the metal uptake process. The XRD patterns (**Fig. A4.1(b)**) further confirmed metal adsorption through precipitation and redox reactions. The appearance of a new diffraction peak at $2\theta = 36.63°$ after Cu^{2+} adsorption suggests the formation of Cu_2O [40]. Along with that, additional minor peaks of Cu_2O was seen at $2\theta = 12.83°, 42.46°, 61.63°$, and $63.20°$ [41]. HNO_3-MBC displayed a new peak at 35.83°, corresponding to crystal planes (002) of CuO [42]. For Pb^{2+} adsorption, the presence of PbO ($2\theta = 28.14°$) and PbO_2 ($2\theta = 35.87°$) suggests lead immobilization through oxidation and carbonate precipitation [43, 44]. Additionally, HNO_3-MBC exhibited peaks at $2\theta =$

20.89°, 27.23° represented the formation of $Pb_3(CO_3)_2(OH)_2$ [40], while a new peak at $2\theta = 40.27°$ indicates the presence of amorphous $Pb(OH)_2$ [45]. Small peaks at $2\theta = 54.09°$ also suggest the possible formation of lead-containing phases, such as $Pb(OH)_2$ [46]. These findings suggest that metal retention is enhanced through surface complexation and precipitation. Notably, KOH-MBC displayed stronger peak shifts and additional crystalline phases compared to HNO_3-MBC. This is likely due to its O-rich surface.

Furthermore, the pH_{pzc} for both KOH-MBC and HNO_3-MBC was determined to be 10.5 (**Fig. 4.10**). As the solution pH during adsorption was lower than the pH_{pzc}, the MBC surfaces remained positively charged, generating a moderately repulsive environment for Cu^{2+} and Pb^{2+} ions. Despite this, strong metal adsorption occurred due to inner-sphere complexation and chemical interactions at oxygen-containing active sites.

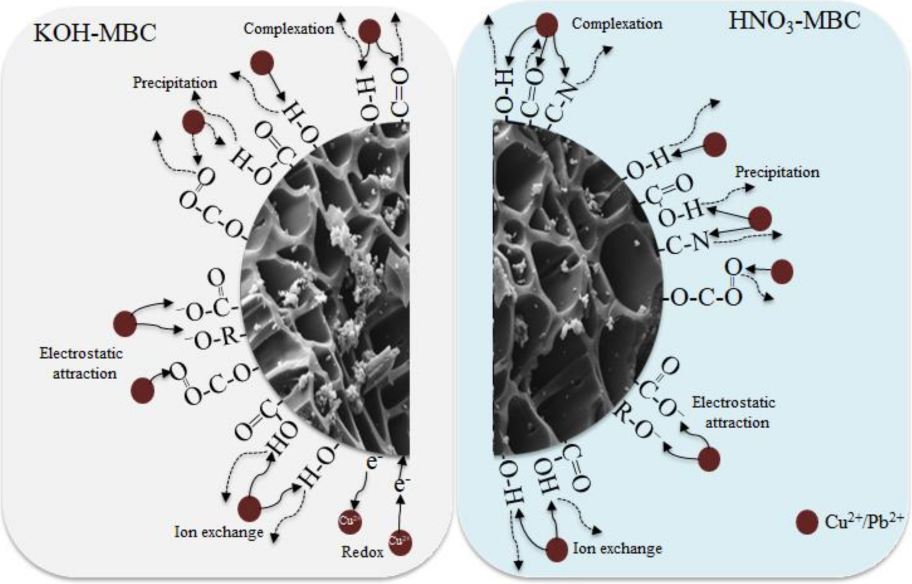

Figure 4.11 Adsorption mechanism of Cu^{2+} and Pb^{2+} onto the KOH-MBC and HNO_3-MBC

4.3.7. Regeneration and reusability

Figure 4.12 shows the reusability performance of KOH-MBC and HNO_3-MBC, tested over four cycles to assess their ability to be reused for removing Cu^{2+} and Pb^{2+}. For KOH-MBC, the initial removal efficiency was 6.17% for Cu^{2+} and 16.12% for Pb^{2+}. However, with each reuse, the efficiency dropped significantly. For example, by the second cycle, Cu^{2+} removal decreased to 3.34%, and by the fourth cycle, it was only 0.24%. Pb^{2+} removal also followed a similar trend, dropping to 4.84% in the second cycle and 1.25% in the fourth cycle. This decline suggests that the BC lost its adsorption capacity over time, possibly due to the saturation of active sites and structural changes. HNO_3-MBC performed slightly differently. It had a higher initial Pb^{2+} removal (17.34%), but lower Cu^{2+} removal (2.96%) compared to KOH-MBC. However, its performance also dropped quickly, with Pb^{2+} removal decreasing to 7.23% in the second cycle and only 0.56% by the fourth. Cu^{2+} removal was already low and dropped to nearly zero (0.03%) in the fourth cycle. This rapid decline indicates that HNO_3-MBC might have lost its effectiveness faster, likely due to stronger metal binding that made regeneration difficult.

Considering that all feedstock materials used for MBC production in this study are wastes, reduced efficiency in cycled applications might not be a serious issue. However, admittedly, it will be better to develop adsorbent materials that can be used repeatedly. In this study, regeneration was performed using acid washing (0.1M HCL), a method chosen to desorb the adsorbed metal ions and restore the active sites. Given the chemisorption-dominated mechanism of our MBCs, two possible explanations for the observed decline in adsorption performance across cycles are proposed. One is that the solvent that we used for regeneration might have destroyed the surface functional groups of the MBC. The second is that the chemisorption activity can not be reversed by our method of regeneration using solvent washing. While acid regeneration is widely used, it can indeed be aggressive. Future studies should explore alternative regeneration strategies, such as using milder desorbing agents or chelating agents like EDTA, which may better preserve functional groups while effectively removing adsorbed metals. Investigating the efficacy and environmental impact of such alternatives could provide valuable insight into improving the reusability of waste-derived MBCs.

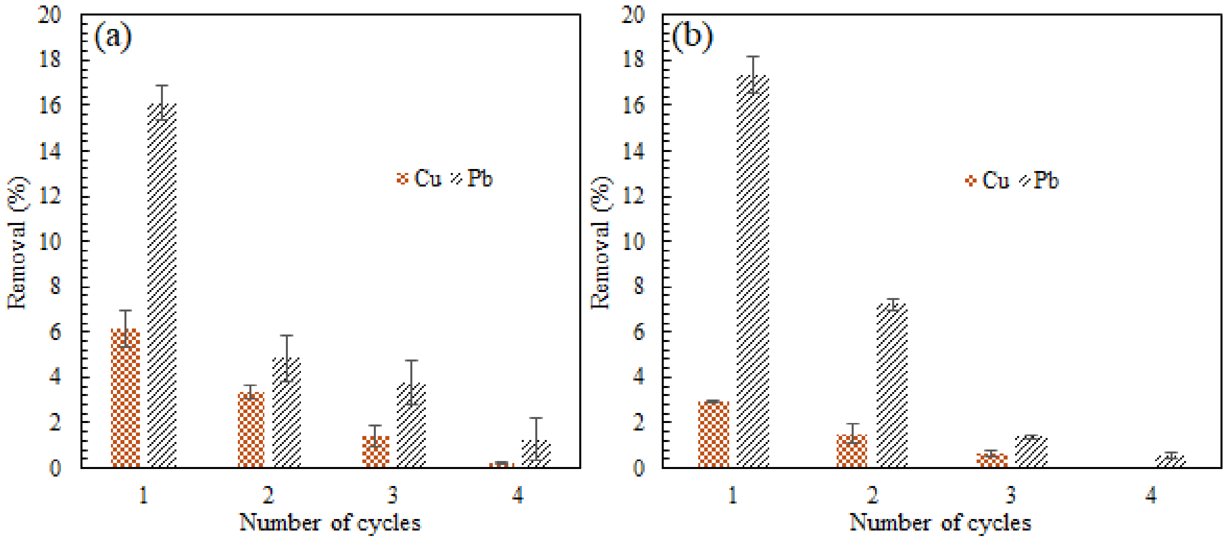

Figure 4.12 Regeneration experiments for spent (a) KOH-MBC and (b) HNO3-MBC in the adsorption of Pb^{2+} and Cu^{2+}

4.3.8. Environmental and economic sustainability of the adsorbents

MW is a widely available and renewable biomass source in Canada. Therefore, using MW as the primary precursor for MBC production can contribute to carbon sequestration by converting organic material into stable carbon, reducing greenhouse gas emissions compared to conventional waste disposal methods such as open burning or landfilling [47]. Furthermore, MBC production offers a value-added application for MW, promoting a circular economy in biomass utilization. As another material used here, RM is generally regarded as an environmental liability because of its high alkalinity, with a pH ranging from 9.0 to 13.2 (average of ~11.3±1.0), as well as the presence of heavy metals such as Cd, Cr, and V [48, 49]. As this is considered a waste, it does not have any value and is often disposed of in tailing ponds or landfills. The presence of salt ions and alkaline compounds in RM forms harmful salt-alkali agglomerates, which can disrupt the stability of ecosystems [50]. However, the global re-utilization rate of RM is still under 15% [50]. So, reusing RM in MBC production not only mitigates disposal challenges but also reduces dependence on synthetic chemicals (iron salts), lowering the environmental footprint associated with chemical synthesis. This approach promotes waste valorization and mitigates environmental pollution. Furthermore, integrating MBC into water treatment will improve resource utilization efficiency [51].

Cost analysis is critical in evaluating the economic viability of new materials or technologies before their large-scale production and implementation. **Table 4.5** shows the estimated cost analysis to produce modified MBCs. The overall cost of production is influenced by several factors, including the availability of raw biomass, collection and transportation logistics, production scale, technology employed, handling, and supply chain considerations [10]. The primary cost drivers for MBC production are raw material expenses and processing costs. Processing costs primarily arise from power consumption during hot air oven drying and high-temperature pyrolysis. In this study, the total production cost of MBC is estimated at approximately CAD 15.47 per kg. For instance, when considering raw maple wood priced at CAD 329 per ton [52], the cost of MBC produced from wood and RM is significantly lower than that of other BC types, which generally range from CAD 50 to CAD 2000 per ton. Moreover, the cost remains substantially lower than that of advanced carbon-based materials such as carbon nanotubes and graphene, which can cost between CAD 50,000 and CAD 100,000 per kg [53]. This study used N_2 as the atmospheric gas during pyrolysis to maintain an O_2-free environment. Some studies have reported successful BC production without atmospheric gases, potentially reducing pyrolysis costs [54]. Additionally, alternative processing methods, such as sun-drying maple wood, could further decrease costs, although they may extend the overall processing time. Furthermore, the chemical modification of MBC increased the cost to CAD 15.47 per kg for KOH-MBC, which is lower than that of HNO_3-MBC (CAD 41.29).

Table 4.5 Estimated cost analysis of producing modified MBC [53]

		Unit Price (CAD)	**Consumption (kg^{-1})**	**Total price (CAD)***
Raw materials**	MW	0.47 kg^{-1}	2.27 kg	1.07
	RM	0	200g	0
Thermal Process***	Drying	0.076 kWh^{-1}	3.08 × 6 kWh^{-1}	1.40
	Grinding	0.076 kWh^{-1}	2.2 × 0.1 kWh^{-1}	0.02
	Pyrolysis	0.076 kWh^{-1}	3.5 × 3 kWh^{-1}	0.80
	N_2	0.9 L^{-1}	4.41 L	11.91
Chemical Modifier****	KOH	0.0011 g^{-1}	252.45 g	0.28
	HNO_3	0.139 ml^{-1}	187.75 mL	26.10

Toal cost	**KOH-MBC**	**15.47**
	HNO_3-MBC	**41.29**

*CAD: Canadian Dollar.

** Purchase from a local shop.

***https://synergynorth.ca/.

****https://www.sigmaaldrich.com/CA/en/product.

[a] The calculations follow the methodology outlined in the article by Y. Wu et al. [53] and have been adjusted based on the consumption data from the current study. The rates are associated with electricity consumption unit prices in Ontario, Canada, the equipment used in this study, and chemical prices obtained from the supplier company.

4.4. Conclusion

This study investigated the adsorption performance of RM-derived MBCs for Cu^{2+} and Pb^{2+} removal, with a focus on the effects of KOH and HNO_3 activation. FTIR and XRD analyses confirmed that chemical activation significantly altered the surface properties of the BCs. KOH activation introduced more oxygen-containing functional groups (e.g., –OH, –COOH), which contributed to the superior adsorption efficiency of KOH-MBC despite its comparatively lower surface area than HNO_3-MBC. Adsorption studies demonstrated that KOH-MBC exhibited superior metal removal efficiency, achieving nearly 100% Cu^{2+} and Pb^{2+} adsorption at optimal conditions, while HNO_3-MBC showed slightly lower efficiency (~95%). Adsorption efficiency increased with higher adsorbent dosage and contact time, with equilibrium reached rapidly for KOH-MBC (within 20 minutes) and slightly later for HNO_3-MBC (40 minutes). The adsorption capacity was significantly influenced by pH, with optimal removal occurring at neutral to alkaline conditions. The adsorption followed the pseudo-second-order model, suggesting chemisorption as the dominant mechanism. Isotherm models revealed that the *Langmuir* model provided the best fit, indicating monolayer adsorption. KOH-MBC exhibited higher maximum adsorption capacities (Q_{max} = 80 mg/g for Cu and 92.59 mg/g for Pb) compared to HNO_3-MBC (Q_{max} = 37.59 mg/g for Cu and 38.61 mg/g for Pb), likely due to increased surface functionality. Also, this study utilizes MW and RM, promoting carbon sequestration and waste valorization while reducing reliance on synthetic chemicals, aligning with the Sustainable Development Goals. The economic analysis further supports the viability of KOH-MBC, given its lower production cost (CAD 15.47/kg) compared to HNO_3-MBC (CAD 41.29/kg). Overall, the results highlight KOH-MBC as a highly effective adsorbent for Cu^{2+} and Pb^{2+} removal, with rapid adsorption kinetics and high capacity, making it a promising material for water treatment applications.

References

[1] L. Ramrakhiani, S. Ghosh, and S. Majumdar, "Heavy metal recovery from electroplating effluent using adsorption by jute waste-derived biochar for soil amendment and plant micro-fertilizer," *Clean Technologies and Environmental Policy,* pp. 1-24, 2022.

[2] P. B. Angon *et al.*, "Sources, effects and present perspectives of heavy metals contamination: Soil, plants and human food chain," *Heliyon,* vol. 10, no. 7, 2024, doi: 10.1016/j.heliyon.2024.e28357.

[3] M. S. Collin *et al.*, "Bioaccumulation of lead (Pb) and its effects on human: A review," *Journal of Hazardous Materials Advances,* vol. 7, p. 100094, 2022/08/01/ 2022, doi: https://doi.org/10.1016/j.hazadv.2022.100094.

[4] R. Teschke, "Copper, iron, cadmium, and arsenic, all generated in the universe: Elucidating their environmental impact risk on human health including clinical liver injury," *International journal of molecular sciences,* vol. 25, no. 12, p. 6662, 2024.

[5] N. R. Canada, "The State of Canada's Forests: Annual Report 2023," 2023. Accessed: March 14, 2025. [Online]. Available: https://natural-resources.canada.ca/sites/nrcan/files/forest/sof2023/NRCAN_SofForest_Annual_2023_EN_accessible-vf(1).pdf

[6] Tim. "10 Native Types of Maple Trees in Canada." Arborist Halifax. https://arboristhalifax.ca/maple-trees-in-canada/ (accessed March 18, 2025).

[7] K. Cheng, W. T. Winter, and A. J. Stipanovic, "A modulated-TGA approach to the kinetics of lignocellulosic biomass pyrolysis/combustion," *Polymer Degradation and Stability,* vol. 97, no. 9, pp. 1606-1615, 2012/09/01/ 2012, doi: https://doi.org/10.1016/j.polymdegradstab.2012.06.027.

[8] A. M. Cheumani Yona *et al.*, "Thermochemical conversion of wood in levulinic acid and application in the preparation of wood coatings," *Biomass Conversion and Biorefinery,* vol. 14, no. 14, pp. 15429-15440, 2024/07/01 2024, doi: 10.1007/s13399-023-03858-x.

[9] N. Kasera, P. Kolar, and S. G. Hall, "Nitrogen-doped biochars as adsorbents for mitigation of heavy metals and organics from water: a review," *Biochar,* vol. 4, no. 1, p. 17, 2022/03/08 2022, doi: 10.1007/s42773-022-00145-2.

[10] J. Pan, H. Deng, Z. Du, K. Tian, and J. Zhang, "Design of nitrogen-phosphorus-doped biochar and its lead adsorption performance," *Environmental Science and Pollution Research,* vol. 29, no. 19, pp. 28984-28994, 2022/04/01 2022, doi: 10.1007/s11356-021-17335-3.

[11] H. Qin, X. Shao, H. Shaghaleh, W. Gao, and Y. A. Hamoud, "Adsorption of Pb2+ and Cd2+ in Agricultural Water by Potassium Permanganate and Nitric Acid-Modified Coconut Shell Biochar," *Agronomy,* vol. 13, no. 7, p. 1813, 2023. [Online]. Available: https://www.mdpi.com/2073-4395/13/7/1813.

[12] Y. Wang, H. Li, and S. Lin, "Advances in the Study of Heavy Metal Adsorption from Water and Soil by Modified Biochar," *Water,* vol. 14, no. 23, p. 3894, 2022. [Online]. Available: https://www.mdpi.com/2073-4441/14/23/3894.

[13] J. Jack, T. M. Huggins, Y. Huang, Y. Fang, and Z. J. Ren, "Production of magnetic biochar from waste-derived fungal biomass for phosphorus removal and recovery," *Journal of Cleaner Production,* vol. 224, pp. 100-106, 2019/07/01/ 2019, doi: https://doi.org/10.1016/j.jclepro.2019.03.120.

[14] X. Zhang *et al.*, "Hydrochar magnetic adsorbent derived from Chinese medicine industry waste via one-step hydrothermal route: Mechanism analyses of magnetism and adsorption," *Fuel,* vol. 326, p. 125110, 2022/10/15/ 2022, doi: https://doi.org/10.1016/j.fuel.2022.125110.

[15] L. A. Pasechnik, V. M. Skachkov, S. A. Bibanaeva, I. S. Medyankina, and V. G. Bamburov, "Composition and Properties of Iron Oxides in the Products of Hydrothermal Treatment of Red Mud and Bauxites," *Russian Journal of Inorganic Chemistry,* vol. 67, no. 7, pp. 1101-1107, 2022/07/01 2022, doi: 10.1134/S0036023622060183.

[16] R. Majumder. "Red mud generation trend across major countries, 2018 to 2023." AL Circle. https://www.alcircle.com/news/red-mud-generation-trend-across-major-countries-2018-to-2023-112752 (accessed March 13, 2025).

[17] N. R. Canada. "Aluminum facts." Natural Resources Canada. https://natural-resources.canada.ca/minerals-mining/mining-data-statistics-analysis/minerals-metals-facts/aluminum-facts#a4 (accessed March 15, 2025).

[18] Y. Liu, R. Naidu, and H. Ming, "Red mud as an amendment for pollutants in solid and liquid phases," *Geoderma,* vol. 163, no. 1, pp. 1-12, 2011/06/15/ 2011, doi: https://doi.org/10.1016/j.geoderma.2011.04.002.

[19] W. Ahmed *et al.*, "Adsorption of Pb(II) from wastewater using a red mud modified rice-straw biochar: Influencing factors and reusability," *Environmental Pollution,* vol. 326, p. 121405, 2023/06/01/ 2023, doi: https://doi.org/10.1016/j.envpol.2023.121405.

[20] G. Loebsack *et al.*, "Adsorption mechanisms and optimal production of magnetic biochar composites from red mud and soft wood biomass," *Journal of Analytical and Applied Pyrolysis,* vol. 177, p. 106340, 2024/01/01/ 2024, doi: https://doi.org/10.1016/j.jaap.2023.106340.

[21] V. Likodimos *et al.*, "Controlled surface functionalization of multiwall carbon nanotubes by HNO3 hydrothermal oxidation," *Carbon,* vol. 69, pp. 311-326, 2014.

[22] Y. Ji, T. Li, L. Zhu, X. Wang, and Q. Lin, "Preparation of activated carbons by microwave heating KOH activation," *Applied surface science,* vol. 254, no. 2, pp. 506-512, 2007.

[23] M. K. Zafeer, R. A. Menezes, H. Venkatachalam, and K. S. Bhat, "Sugarcane bagasse-based biochar and its potential applications: a review," *Emergent Materials,* vol. 7, no. 1, pp. 133-161, 2024/02/01 2024, doi: 10.1007/s42247-023-00603-y.

[24] C. Zhao, J. Ma, Z. Li, H. Xia, H. Liu, and Y. Yang, "Highly enhanced adsorption performance of tetracycline antibiotics on KOH-activated biochar derived from reed plants," *RSC advances,* vol. 10, no. 9, pp. 5066-5076, 2020.

[25] L. Yan *et al.*, "Insight into the Amelioration Effect of Nitric Acid-Modified Biochar on Saline Soil Physicochemical Properties and Plant Growth," *Plants,* vol. 13, no. 23, p. 3434, 2024. [Online]. Available: https://www.mdpi.com/2223-7747/13/23/3434.

[26] X. y. Zhou, F. Xie, M. Jiang, L. KE-ao, and S. g. Tian, "Physicochemical properties and lead ion adsorption of biochar prepared from Turkish gall residue at different pyrolysis temperatures," *Microscopy Research and Technique,* vol. 84, no. 5, pp. 1003-1011, 2021.

[27] O. Tomin and M. R. Yazdani, "Production and characterization of porous magnetic biochar: before and after phosphate adsorption insights," *Journal of Porous Materials,* vol. 29, no. 3, pp. 849-859, 2022/06/01 2022, doi: 10.1007/s10934-022-01217-1.

[28] S. Ahmad *et al.*, "Magnetic properties of different phases iron oxide nanoparticles prepared by micro emulsion-hydrothermal method," *Scientific Reports,* vol. 15, no. 1, p. 878, 2025/01/06 2025, doi: 10.1038/s41598-025-85145-5.

[29] J. Zhang, Q. Li, J. Zhang, H. Liu, H. Wang, and J. Zhang, "Enhanced CO2 absorption in amine-based carbon capture aided by coconut shell-derived nitrogen-doped biochar," *Separation and Purification Technology,* vol. 353, p. 128451, 2025/01/19/ 2025, doi: https://doi.org/10.1016/j.seppur.2024.128451.

[30] Y. Zheng *et al.*, "Insight into the KOH/KMnO4 activation mechanism of oxygen-enriched hierarchical porous biochar derived from biomass waste by in-situ pyrolysis for methylene blue enhanced adsorption," *Journal of Analytical and Applied Pyrolysis,* vol. 158, p. 105269, 2021/09/01/ 2021, doi: https://doi.org/10.1016/j.jaap.2021.105269.

[31] G.-l. Gao, P.-j. Zhou, C.-q. Chen, and L.-l. Zhu, "Adsorption of MB and Pb(II) before and after magnetic modification: Performance and mechanism," *Journal of Molecular Structure,* vol. 1293, p. 136306, 2023/12/05/ 2023, doi: https://doi.org/10.1016/j.molstruc.2023.136306.

[32] A. Eleryan *et al.*, "Copper(II) ion removal by chemically and physically modified sawdust biochar," *Biomass Conversion and Biorefinery,* vol. 14, no. 8, pp. 9283-9320, 2024/04/01 2024, doi: 10.1007/s13399-022-02918-y.

[33] V. Singh *et al.*, "Adsorption Studies of Pb(II) and Cd(II) Heavy Metal Ions from Aqueous Solutions Using a Magnetic Biochar Composite Material," *Separations,* vol. 10, no. 7, p. 389, 2023. [Online]. Available: https://www.mdpi.com/2297-8739/10/7/389.

[34] C. Duan, T. Ma, J. Wang, and Y. Zhou, "Removal of heavy metals from aqueous solution using carbon-based adsorbents: A review," *Journal of Water Process Engineering,* vol. 37, p. 101339, 2020.

[35] R. Castejón-del Pino, M. L. Cayuela, M. Sánchez-García, and M. A. Sánchez-Monedero, "Nitrogen availability in biochar-based fertilizers depending on activation treatment and nitrogen source," *Waste Management,* vol. 158, pp. 76-83, 2023.

[36] L. Deng *et al.*, "Straw-based biochar prepared from multi-step KOH activation and its structure-effect relationship of CO2 capture under atmospheric/pressurized conditions via experimental analysis and MD/DFT calculations," *Chemical Engineering Journal,* vol. 495, p. 153403, 2024/09/01/ 2024, doi: https://doi.org/10.1016/j.cej.2024.153403.

[37] F. P. Dad, W.-u.-D. Khan, F. Sharif, and A. S. Nizami, "Adsorption of trace heavy metals through organic compounds enriched biochar using isotherm adsorption and kinetic models," *Environmental Research,* vol. 241, p. 117702, 2024/01/15/ 2024, doi: https://doi.org/10.1016/j.envres.2023.117702.

[38] J. O. Ighalo, A. G. Adeniyi, O. A. Eletta, and L. T. Arowoyele, "Competitive adsorption of Pb (II), Cu (II), Fe (II) and Zn (II) from aqueous media using biochar from oil palm (Elaeis guineensis) fibers: a kinetic and equilibrium study," *Indian chemical engineer,* vol. 63, no. 5, pp. 501-511, 2021.

[39] A. B. D. Nandiyanto *et al.*, "Sustainable biochar carbon microparticles based on mangosteen peel as biosorbent for dye removal: Theoretical review, modelling, and adsorption isotherm characteristics," *Journal of Advanced Research in Fluid Mechanics and Thermal Sciences,* vol. 105, no. 1, pp. 41-58, 2023.

[40] Q. Wu, S. Dong, L. Wang, and X. Li, "Single and Competitive Adsorption Behaviors of Cu2+, Pb2+ and Zn2+ on the Biochar and Magnetic Biochar of Pomelo Peel in Aqueous Solution," *Water,* vol. 13, no. 6, p. 868, 2021. [Online]. Available: https://www.mdpi.com/2073-4441/13/6/868.

[41] N. H. Lam *et al.*, "Evaluation of the Structural Deviation of Cu/Cu2O Nanocomposite Using the X-ray Diffraction Analysis Methods," *Crystals,* vol. 12, no. 4, p. 566, 2022. [Online]. Available: https://www.mdpi.com/2073-4352/12/4/566.

[42] M. Taunk and N. Singh, "A Comparative Analysis of X-Ray Diffraction, Morphology, and Optical Properties of Sonochemically Synthesized Cupric Oxide Nanostructures," *Journal of Electronic Materials,* vol. 52, no. 10, pp. 6888-6901, 2023/10/01 2023, doi: 10.1007/s11664-023-10611-7.

[43] J. Li, M. Guo, Y. Shao, H. Yu, and K. Ni, "Electrocatalytic Properties of a Novel β-PbO2/Halloysite Nanotube Composite Electrode," *ACS Omega,* vol. 6, no. 8, pp. 5436-5444, 2021/03/02 2021, doi: 10.1021/acsomega.0c05651.

[44] K. Hari Prasad, S. Vinoth, P. Jena, M. Venkateswarlu, and N. Satyanarayana, "Structural characterization and impedance studies of PbO nanofibers synthesized by electrospinning technique," *Materials Chemistry and Physics,* vol. 194, pp. 188-197, 2017/06/15/ 2017, doi: https://doi.org/10.1016/j.matchemphys.2017.03.040.

[45] J. Huang *et al.*, "Trace Doping of Pb(OH)2 Species on PdPb Alloys Boost Highly Active and Stable Ethanol Oxidation," *ACS Omega,* vol. 7, no. 40, pp. 35720-35726, 2022/10/11 2022, doi: 10.1021/acsomega.2c03693.

[46] J. Shin *et al.*, "Oyster shell-doped ground coffee waste biochars for selective removal of phosphate and nitrate ions from aqueous phases via enhanced electrostatic surface complexations: A mechanism study," *Journal of Environmental Chemical Engineering,* vol. 12, no. 2, p. 112154, 2024/04/01/ 2024, doi: https://doi.org/10.1016/j.jece.2024.112154.

[47] A. Waheed *et al.*, "Biochar in sustainable agriculture and Climate Mitigation: Mechanisms, challenges, and applications in the circular bioeconomy," *Biomass and Bioenergy,* vol. 193, p. 107531, 2025/02/01/ 2025, doi: https://doi.org/10.1016/j.biombioe.2024.107531.

[48] Y. Qi, "The neutralization and recycling of red mud–a review," in *Journal of physics: conference series*, 2021, vol. 1759, no. 1: IOP Publishing, p. 012004.

[49] M. Jovičević-Klug, I. R. Souza Filho, H. Springer, C. Adam, and D. Raabe, "Green steel from red mud through climate-neutral hydrogen plasma reduction," *Nature,* vol. 625, no. 7996, pp. 703-709, 2024/01/01 2024, doi: 10.1038/s41586-023-06901-z.

[50] G. Li, J. Liu, L. Yi, J. Luo, and T. Jiang, "Bauxite residue (red mud) treatment: Current situation and promising solution," *Science of The Total Environment,* vol. 948, p. 174757, 2024/10/20/ 2024, doi: https://doi.org/10.1016/j.scitotenv.2024.174757.

[51] P. Kumar *et al.*, "Investigating innovative techniques for biochar modification to enhance the removal of heavy metals from aqueous environments: a comprehensive review," *Clean Technologies and Environmental Policy,* 2024/08/16 2024, doi: 10.1007/s10098-024-02962-4.

[52] S. Pap, K. G. Boyd, M. A. Taggart, and M. Turk Sekulic, "Circular economy based landfill leachate treatment with sulphur-doped microporous biochar," *Waste Management,* vol. 124, pp. 160-171, 2021/04/01/ 2021, doi: https://doi.org/10.1016/j.wasman.2021.01.037.

[53] Y. Wu *et al.*, "Recovery and regeneration of water-hardened magnetic composite biochar sphere for the removal of multiple heavy metals in contaminated soils," *Journal of Cleaner Production,* vol. 450, p. 141906, 2024/04/15/ 2024, doi: https://doi.org/10.1016/j.jclepro.2024.141906.

[54] Y. Dan, X. Wang, M. Ji, W. Sang, Z. Shen, and Y. Zhang, "Influence of temperature change on the immobilization of soil Pb and Zn by hydrochar: Roles of soil microbial modulation," *Environmental Pollution,* vol. 320, p. 121109, 2023/03/01/ 2023, doi: https://doi.org/10.1016/j.envpol.2023.121109.

Chapter 5 Conclusions and future perspectives

5.1. Overall conclusion

Magnetic biochar (MBC) has emerged as a promising candidate due to its low-cost synthesis, high surface reactivity, and potential for environmental sustainability. This thesis focused on the synthesis, modification, and performance evaluation of various MBCs derived from MW and RM for the adsorption of both organic dyes and toxic heavy metals, including Cu^{2+} and Pb^{2+}. Through a series of interconnected studies, the research has demonstrated the feasibility of utilizing biomass waste and industrial by-products to create high-performance, magnetically retrievable adsorbents with excellent adsorption efficiencies.

In the first phase of this study, MBCs were synthesized using different iron anchoring strategies, with one-step co-pyrolysis proving to be the most efficient method in terms of ease of synthesis and adsorption performance. The co-pyrolysis of MW and FeO at an optimal ratio of 1:1 and a temperature of 700 °C yielded MBC with superior removal efficiency for reactive dyes, achieving up to 100% removal of RBBR dye from aqueous solution. This high performance was attributed to the successful incorporation of iron particles into the carbon matrix, which significantly improved the physicochemical properties of the MBC. Characterization results revealed the development of desirable surface features, including magnetic functionality, porosity, and abundant functional groups. Adsorption kinetics and isotherm studies further supported these findings, with the pseudo-second-order model and *Langmuir* isotherm providing the best fit, suggesting that chemisorption and monolayer adsorption dominated the mechanism.

The second phase of this study extended this work by incorporating RM as an alternative iron precursor and applying chemical activation techniques to enhance surface properties. RM, often regarded as a disposal problem in the aluminum industry, was valorized as both a source of iron for magnetization and a structural support for MBC production. Chemical activation using potassium hydroxide (KOH) and nitric acid (HNO_3) was employed to tune the surface chemistry of RM-derived MBCs. FTIR and XRD analysis confirmed that both treatments significantly modified the surface functional groups and crystallinity of the materials, though KOH-activated MBC (KOH-MBC) exhibited more abundant oxygen-containing functional groups, such as hydroxyl and carboxyl moieties, that are known to play a vital role in heavy metal binding.

Among the modified materials, KOH-MBC exhibited outstanding adsorption capacities for Cu^{2+} and Pb^{2+}, achieving nearly complete removal (~100%) at optimal conditions and demonstrating rapid equilibrium times (within 20 minutes). Interestingly, this performance was achieved despite KOH-MBC having a relatively lower surface area than its HNO_3-activated counterpart, highlighting the critical role of surface chemistry over mere surface area in adsorption performance. Adsorption mechanisms were predominantly governed by chemisorption, supported by kinetic and isotherm analyses, which again aligned with the pseudo-second-order and *Langmuir* adsorption isotherm models. The maximum adsorption capacities (Q_{max}) of KOH-MBC were 80 mg/g for Cu^{2+} and 92.59 mg/g for Pb^{2+}, significantly higher than those of HNO_3-MBC. In addition to superior performance, KOH-MBC also demonstrated lower production costs (CAD 15.47/kg) compared to HNO_3-MBC (CAD 41.29/kg), making it a more economically viable choice for large-scale implementation.

Collectively, the results of these three studies reinforce the potential of MBC as an advanced adsorbent for water treatment applications. The strategic integration of biomass resources, industrial wastes, and low-cost chemical treatments yielded materials with high removal efficiency, rapid kinetics, and magnetic properties, enabling easy separation. The environmental implications of this work are substantial: using red mud not only addresses its waste management challenges but also contributes to circular economy principles and sustainable development goals by producing value-added materials for pollution mitigation.

This research also advances the scientific understanding of MBC synthesis and functionality. It highlights the importance of carefully selecting synthesis parameters, such as the FeO-to-biomass ratio, pyrolysis temperature, and activation agent, to tune the structural and chemical properties of biochar. Moreover, it illustrates how the interplay between surface chemistry, porosity, and magnetization can be harnessed to optimize adsorption performance across different pollutants. This thesis presents a comprehensive approach to developing and optimizing MBC for environmental remediation. It not only validates the high performance of these materials in removing organic dyes and toxic heavy metals but also offers practical insights into cost-effective, scalable production methods. The work lays a strong foundation for future innovations in adsorbent design and contributes to the broader goal of achieving clean and safe water through sustainable technologies.

5.2. Recommendations for future work

While the findings of this thesis are promising, several areas require further investigation to advance the practical application of MBC in real-world water treatment systems. Firstly, future research should explore magnetic components' long-term stability, reusability, and leaching behavior under varied environmental conditions to ensure safety and minimize secondary contamination. Scale-up studies and pilot-scale experiments using real wastewater are essential to validate laboratory-scale performance and address potential operational challenges such as fouling, adsorbent loss, and regeneration efficiency. Moreover, further optimization of the red mud pre-treatment process and exploring other low-cost biomass and industrial residues could yield tailored MBC for specific contaminants. To gain mechanistic insights, advanced characterization techniques (e.g., XPS, TEM, synchrotron-based spectroscopy) and computational modeling approaches (e.g., density functional theory, molecular dynamics) should be employed to study adsorption pathways at the molecular level. Integrating machine learning (ML) and artificial intelligence (AI) in the optimization of synthesis parameters and performance prediction models could accelerate materials development. Finally, incorporating life cycle assessment (LCA) and techno-economic analysis (TEA) in future work will be critical for evaluating these MBCs' environmental footprint and commercial viability, thus guiding the development of sustainable and scalable solutions for water decontamination.

Appendix

Efficient iron anchoring methods for magnetic biochar synthesis: Material characteristics and functional mechanism in dye removal (Chapter 3)

Table A3.1 Proximate analysis of MW chips and MBC samples (reported values represent the mean ± standard deviation)

Sample	**Moisture %**	**Volatile Matter %**	**Ash %**	**Fixed Carbon %**
MW	1.32 ± 0.09	85.36 ± 0.48	0.61 ± 0.11	12.71 ± 0.28
1:1-MBC700	0.78 ± 0.16	5.22 ± 0.11	85.08 ± 0.50	8.92 ± 0.54
1:2-MBC700	1.06 ± 0.05	11.23 ± 1.22	68.54 ± 1.10	19.16 ± 2.26
1:3-MBC700	0.84 ± 0.01	14.63 ± 0.60	58.27 ± 0.79	26.26 ± 0.20
1:4-MBC700	1.17 ± 0.13	16.93 ± 1.08	52.70 ± 0.53	29.20 ± 0.69
1:5-MBC700	2.38 ± 0.04	15.18 ± 1.38	44.45 ± 0.14	37.99 ± 1.48

Table A3.2 Regression analysis and ANOVA results showing the influence of FeO content (X1), maple wood content (X2), and adsorbent dosage (X3) on metal adsorption efficiency

Regression Statistics	
Multiple R	0.897
R^2	0.805
Adjusted R^2	0.787
Standard Error	12.282
Observations	36.000

ANOVA

	df	*SS*	*MS*	*F*	*Significance F*
Regression	3.000	19943.017	6647.672	44.067	0.000
Residual	32.000	4827.340	150.854		
Total	35.000	24770.356			

	Coefficients	*Standard Error*	*t Stat*	*P-value*	*Lower 95%*	*Upper 95%*	*Lower 95.0%*	*Upper 95.0%*
Intercept	12.169	6.020	2.021	0.052	-0.094	24.432	-0.094	24.432
X Variable 1	44.600	6.343	7.032	0.000	31.681	57.520	31.681	57.520
X Variable 2	-4.794	1.586	-3.023	0.005	-8.023	-1.564	-8.023	-1.564
X Variable 3	63.851	7.033	9.079	0.000	49.526	78.176	49.526	78.176

Table A3.3 Regression analysis and ANOVA results evaluating the effect of FeO content (X1), maple wood content (X2), and contact time (X3) on metal adsorption efficiency

Regression Statistics	
Multiple R	0.947
R^2	0.897
Adjusted R^2	0.888
Standard Error	6.278
Observations	36.000

ANOVA

	df	*SS*	*MS*	*F*	*Significance F*
Regression	3.000	11035.301	3678.434	93.344	0.000
Residual	32.000	1261.034	39.407		
Total	35.000	12296.335			

	Coefficients	*Standard Error*	*t Stat*	*P-value*	*Lower 95%*	*Upper 95%*	*Lower 95.0%*	*Upper 95.0%*
Intercept	41.130	2.832	14.522	0.000	35.361	46.899	35.361	46.899
X Variable 1	50.819	3.242	15.677	0.000	44.216	57.422	44.216	57.422
X Variable 2	-4.911	0.810	-6.060	0.000	-6.562	-3.260	-6.562	-3.260
X Variable 3	0.056	0.010	5.482	0.000	0.035	0.077	0.035	0.077

Table A3.4 Regression analysis and ANOVA results evaluating the effect of FeO content (X1), maple wood content (X2), and pH (X3) on metal adsorption efficiency

Regression Statistics	
Multiple R	0.952
R^2	0.906

Adjusted R^2	0.895
Standard Error	6.040
Observations	30.000

ANOVA					
	df	*SS*	*MS*	*F*	*Significance F*
Regression	3.000	9095.169	3031.723	83.116	0.000
Residual	26.000	948.370	36.476		
Total	29.000	10043.539			

	Coefficients	*Standard Error*	*t Stat*	*P-value*	*Lower 95%*	*Upper 95%*	*Lower 95.0%*	*Upper 95.0%*
Intercept	56.898	3.933	14.465	0.000	48.812	64.983	48.812	64.983
X Variable 1	46.651	3.416	13.655	0.000	39.628	53.673	39.628	53.673
X Variable 2	-0.716	0.854	-0.839	0.409	-2.472	1.039	-2.472	1.039
X Variable 3	-1.514	0.390	-3.883	0.001	-2.315	-0.713	-2.315	-0.713

Table A3.5 Pseudo-first-order and Pseudo-second-order parameters of adsorption of RBBR onto MBC

RBBR (PPM)	**Pseudo-first-order**			**Pseudo-second-order**		
	Q_{max} (mg/g)	k_1	R^2	Q_{cal} (mg/g)	k_2	R^2
100	0.6811	0.1828	0.8046	4.83559	0.02043	0.9903
200	0.8329	0.1828	0.8599	10.97695	0.145856	0.9976
300	4.3562	1.4716	0.8237	16.44737	0.012409	0.9977
400	8.5609	2.1472	0.7012	19.19386	0.010235	0.9984
500	12.4697	2.5233	0.688	21.14165	0.009935	0.9979

Table A3.6 Intraparticle Diffusion Model and Film Diffusion Model parameters for the adsorption of RBBR dye onto MBC

RBBR (PPM)	**Intraparticle Diffusion Model**			**Film Diffusion Model**	
	k_d	C	R^2	K_{fd}	R^2

100	0.01987	5.72978	0.608	0.0172	0.9112
200	0.0697	10.0635	0.7681	0.0025	0.6529
300	0.25821	12.7199	0.8475	0.0043	0.8055
400	0.37691	13.8402	0.7178	0.0026	0.7019
500	0.35783	16.0274	0.8394	0.0016	0.7218

Table A3.7 *Langmuir*, *Freundlich*, and *Temkin* adsorption isotherm parameters for the adsorption of RBBR dye onto MBC

***Langmuir* model**			***Freundlich* model**			***Temkin* model**		
Q_{max} (mg/g)	K_l	R^2	K_f	n_F	R^2	b_T (J/mol)	K_t (L/g)	R^2
11.327	8.2991	0.9877	43.271	0.192	0.9154	143.47	12.42	0.925

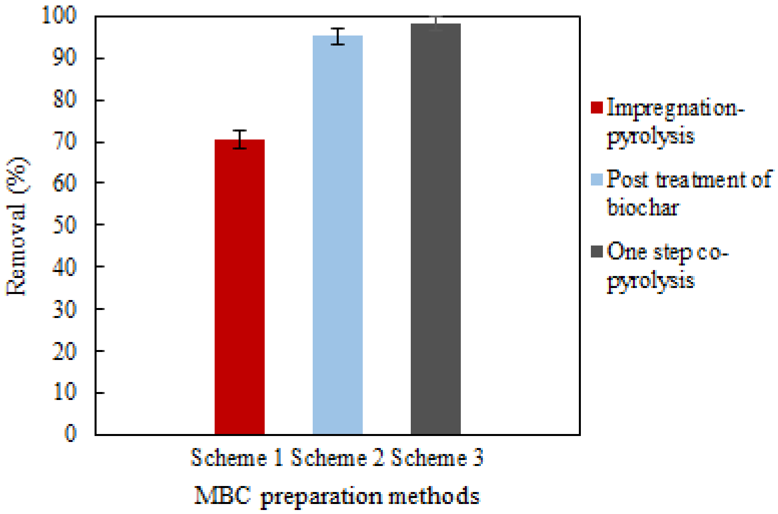

Figure A3.1 Effect of different magnetic biochar preparation methods on RBBR dye removal efficiency

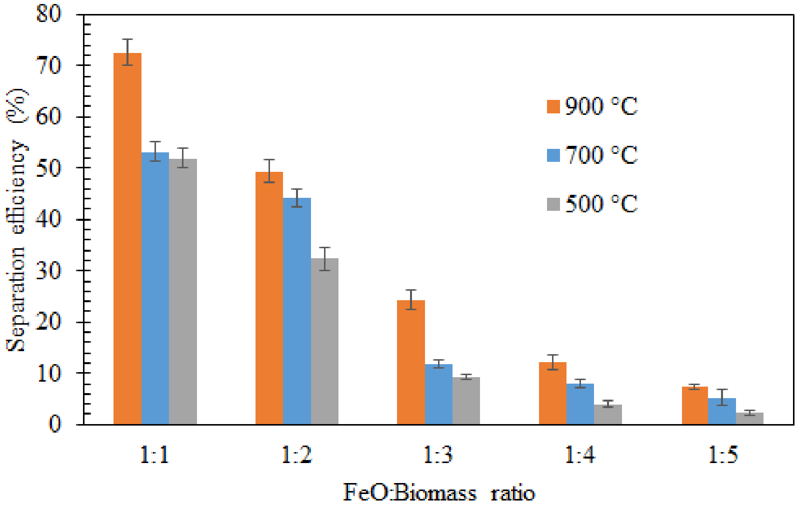

Figure A3.2 Magnetic strength test of the MBC characterized by the separation efficiency of different MBC samples with the electromagnet (MBC weight: 0.1 g; Electromagnet power: 0.5 A)

Pre-pyrolysis activation strategy to enhance heavy metal adsorption by industrial waste-based magnetic biochar (Chapter 4)

Experimental: Detailed explanations of kinetic models used in this study

The adsorption kinetics of different MBCs were examined by mixing the optimum dose (0.2 g KOH-MBC, 0.5 g HNO_3-MBC) of the samples in a 30 mL metal salt solution in a 50 mL Falcon tube. The initial pH of the solution was adjusted to 6.5 ± 0.1 using 0.1 M HCl or 0.1 M NaOH. The tubes were placed in a constant-shaker and shaken at room temperature, 300 rpm, until sampling. At each sampling time (5, 10, 15, 20, 30, 60, and 120 minutes), a sample of the suspension was taken and filtered through a 0.2 µm syringe filter.

The corresponding equations for these models are presented below, as **Equations A4.1 and A4.2**.

Pseudo-first-order kinetic model:

$$\ln(q_e - q_t) = lnq_e - k_1 t \qquad \text{(A4.1)}$$

Pseudo-second-order kinetic model:

$$\frac{t}{q} = \frac{1}{k_2 q_e^2} + \frac{t}{q_e} \quad \text{(A4.2)}$$

Where q_t = amount of adsorbate adsorbed at time t (mg/g), q_e = Amount of adsorbate adsorbed at equilibrium (mg/g), k_1 = Rate constant, t = Contact time (min). k_2 = Rate constant of the pseudo-second-order q_t = Amount of adsorbate adsorbed at time t (mg/g).

The adsorption isotherms were determined at an initial metal salt concentration of 500-700 mg/L. Each metal salt solution (30 mL), with an initial pH of 6.5 ± 0.1, was poured into a 50 mL Falcon tube. The optimum dosage of adsorbents (0.2 g KOH-MBC, 0.5 g HNO_3-MBC) was added to each Falcon tube and equilibrated at room temperature for 24 h in a constant shaker. The *Langmuir* and *Freundlich* models were employed to fit the data from the adsorption isotherms. The equations for these models are provided below as **Equations 4** and **5**, respectively.

Langmuir isotherm model:

$$\frac{C_e}{q_e} = \frac{1}{q_m K_L} + \frac{C_e}{q_m} \quad (4)$$

Freundlich isotherm model:

$$\ln q_e = \ln K_F + \frac{1}{n} \ln C_e \quad (5)$$

Where q_e = Amount of adsorbate adsorbed (mg/g), q_m = Maximum adsorption capacity (mg/g), K_L = *Langmuir* constant (L/mg), C_e = Equilibrium concentration (mg/L), K_F = *Freundlich* constant, n = Heterogeneity factor.

Table A4.1 Regression analysis and ANOVA results evaluating the effect of KOH-modification (X1), HNO_3-modification (X2), pristine biochar (X3), and adsorbent dosage (X4) on Cu adsorption efficiency

Regression Statistics	
Multiple R	0.961
R^2	0.924
Adjusted R^2	0.837
Standard Error	12.479
Observations	18.000

ANOVA					
	df	*SS*	*MS*	*F*	*Significance F*
Regression	4.000	26670.471	6667.618	57.090	0.000

Residual	14.000	2180.113	155.722		
Total	18.000	28850.584			

	Coefficients	*Standard Error*	*t Stat*	*P-value*	*Lower 95%*	*Upper 95%*	*Lower 95.0%*	*Upper 95.0%*
Intercept	71.576	7.892	9.069	0.000	54.648	88.503	54.648	88.503
X Variable 1	0.000	0.000	65535.000	-	0.000	0.000	0.000	0.000
X Variable 2	-36.905	7.205	-5.122	-	-52.358	-21.453	-52.358	-21.453
X Variable 3	-89.242	7.205	-12.387	0.000	-104.695	-73.790	-104.695	-73.790
X Variable 4	69.552	17.222	4.038	0.001	32.613	106.490	32.613	106.490

Table A4.2 Regression analysis and ANOVA results evaluating the effect of KOH-modification (X1), HNO_3-modification (X2), pristine biochar (X3), and adsorbent dosage (X4) on Pb adsorption efficiency

Regression Statistics	
Multiple R	0.963
R^2	0.927
Adjusted R^2	0.840
Standard Error	11.276
Observations	18.000

ANOVA

	df	*SS*	*MS*	*F*	*Significance F*
Regression	4.000	22609.180	5652.295	59.269	0.000
Residual	14.000	1780.188	127.156		
Total	18.000	24389.368			

	Coefficients	*Standard Error*	*t Stat*	*P-value*	*Lower 95%*	*Upper 95%*	*Lower 95.0%*	*Upper 95.0%*
Intercept	68.056	7.132	9.543	0.000	52.760	83.352	52.760	83.352
X Variable 1	0.000	0.000	65535.000	-	0.000	0.000	0.000	0.000
X Variable 2	-25.959	6.510	-3.987	-	-39.923	-11.996	-39.923	-11.996
X Variable 3	-78.335	6.510	-12.032	0.000	-92.298	-64.371	-92.298	-64.371

X Variable 4	81.678	15.563	5.248	0.000	48.299	115.057	48.299	115.057

Table A4.3 Regression analysis and ANOVA results evaluating the effect of KOH-modification (X1), HNO_3-modification (X2), pristine biochar (X3), and contact time (X4) on Cu adsorption efficiency

Regression Statistics	
Multiple R	0.965
R Square	0.932
Adjusted R Square	0.885
Standard Error	10.772
Observations	30.000

ANOVA

	df	*SS*	*MS*	*F*	*Significance F*
Regression	4.000	41066.784	10266.696	117.967	0.000
Residual	26.000	3017.048	116.040		
Total	30.000	44083.832			

	Coefficients	*Standard Error*	*t Stat*	*P-value*	*Lower 95%*	*Upper 95%*	*Lower 95.0%*	*Upper 95.0%*
Intercept	79.442	4.195	18.936	0.000	70.818	88.065	70.818	88.065
X Variable 1	0.000	0.000	65535.000	-	0.000	0.000	0.000	0.000
X Variable 2	-32.806	4.817	-6.810	-	-42.708	-22.904	-42.708	-22.904
X Variable 3	-85.931	4.817	-17.837	0.000	-95.834	-76.029	-95.834	-76.029
X Variable 4	0.304	0.056	5.459	0.000	0.189	0.418	0.189	0.418

Table A4.2 Regression analysis and ANOVA results evaluating the effect of KOH-modification (X1), HNO_3-modification (X2), pristine biochar (X3), and contact time (X4) on Pb adsorption efficiency

Regression Statistics	
Multiple R	0.949
R^2	0.901
Adjusted R^2	0.852
Standard Error	11.415
Observations	30.000

ANOVA					
	df	*SS*	*MS*	*F*	*Significance F*
Regression	4.000	30974.198	7743.549	79.237	0.000
Residual	26.000	3387.862	130.302		
Total	30.000	34362.060			

	Coefficients	*Standard Error*	*t Stat*	*P-value*	*Lower 95%*	*Upper 95%*	*Lower 95.0%*	*Upper 95.0%*
Intercept	83.056	4.446	18.683	0.000	73.918	92.194	73.918	92.194
X Variable 1	0.000	0.000	65535.000	-	0.000	0.000	0.000	0.000
X Variable 2	-27.216	5.105	-5.331	-	-37.709	-16.722	-37.709	-16.722
X Variable 3	-72.251	5.105	-14.153	0.000	-82.744	-61.758	-82.744	-61.758
X Variable 4	0.340	0.059	5.774	0.000	0.219	0.462	0.219	0.462

Table A4.5 Regression analysis and ANOVA results evaluating the effect of KOH-modification (X1), HNO_3-modification (X2), pristine biochar (X3), and pH (X4) on Cu adsorption efficiency

Regression Statistics	
Multiple R	0.906
R^2 Square	0.821
Adjusted R^2	0.682
Standard Error	18.190

Observations	15.000

ANOVA					
	df	*SS*	*MS*	*F*	*Significance F*
Regression	4.000	16721.303	4180.326	16.846	0.000
Residual	11.000	3639.550	330.868		
Total	15	20360.85336			

	Coefficients	*Standard Error*	*t Stat*	*P-value*	*Lower 95%*	*Upper 95%*	*Lower 95.0%*	*Upper 95.0%*
Intercept	-34.719	14.187	-2.447	0.032	-65.945	-3.493	-65.945	-3.493
X Variable 1	0.000	0.000	65535.000	-	0.000	0.000	0.000	0.000
X Variable 2	44.204	11.504	3.842	-	18.883	69.524	18.883	69.524
X Variable 3	35.617	11.504	3.096	0.010	10.296	60.938	10.296	60.938
X Variable 4	9.673	1.660	5.825	0.000	6.018	13.327	6.018	13.327

Table A4.6 Regression analysis and ANOVA results evaluating the effect of KOH-modification (X1), HNO_3-modification (X2), pristine biochar (X3), and pH (X4) on Pb adsorption efficiency

Regression Statistics	
Multiple R	0.915
R^2	0.837
Adjusted R^2	0.702
Standard Error	16.880
Observations	15.000

ANOVA					
	df	*SS*	*MS*	*F*	*Significance F*
Regression	4.000	16153.418	4038.354	18.896	0.000
Residual	11.000	3134.444	284.949		
Total	15.000	19287.861			

	Coefficients	*Standard Error*	*t Stat*	*P-value*	*Lower 95%*	*Upper 95%*	*Lower 95.0%*	*Upper 95.0%*
Intercept	-29.252	13.166	-2.222	0.048	-58.230	-0.274	-58.230	-0.274
X Variable 1	0.000	0.000	65535.000	-	0.000	0.000	0.000	0.000
X Variable 2	39.742	10.676	3.722	-	16.244	63.240	16.244	63.240
X Variable 3	32.903	10.676	3.082	0.010	9.405	56.401	9.405	56.401
X Variable 4	9.848	1.541	6.391	0.000	6.457	13.240	6.457	13.240

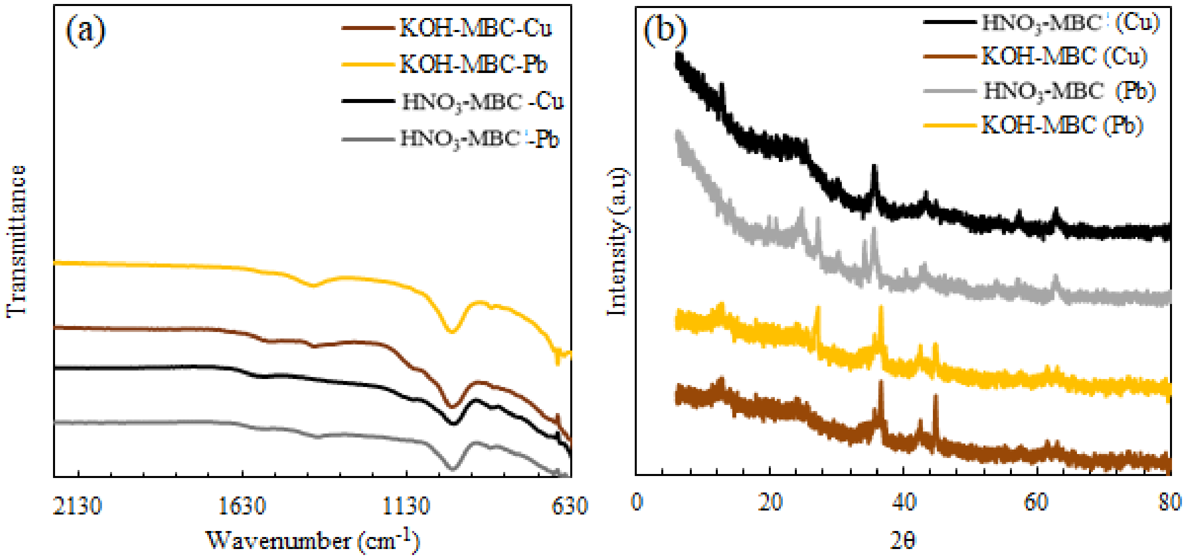

Figure A4.1 Post-adsorption (a) FTIR and (b) XRD spectra of different MBC samples